Quantitative Laser Doppler Flowmetry

Ingemar Fredriksson

Department of Biomedical Engineering
Linköping University
Linköping 2009

Linköping University
INSTITUTE OF TECHNOLOGY

Quantitative Laser Doppler Flowmetry

Ingemar Fredriksson

Department of Biomedical Engineering
Linköping University
SE-581 85 Linköping, Sweden

Cover art:
Computer generated laser speckle pattern

Till Carina

Abstract

Laser Doppler flowmetry (LDF) is virtually the only non-invasive technique, except for other laser speckle based techniques, that enables estimation of the microcirculatory blood flow. The technique was introduced into the field of biomedical engineering in the 1970s, and a rapid evolvement followed during the 1980s with fiber based systems and improved signal analysis. The first imaging systems were presented in the beginning of the 1990s.

Conventional LDF, although unique in many aspects and elegant as a method, is accompanied by a number of limitations that may have reduced the clinical impact of the technique. The analysis model published by Bonner and Nossal in 1981, which is the basis for conventional LDF, is limited to measurements given in arbitrary and relative units, unknown and non-constant measurement volume, non-linearities at increased blood tissue fractions, and a relative average velocity estimate.

In this thesis a new LDF analysis method, quantitative LDF, is presented. The method is based on recent models for light-tissue interaction, comprising the current knowledge of tissue structure and optical properties, making it fundamentally different from the Bonner and Nossal model. Furthermore and most importantly, the method eliminates or highly reduces the limitations mentioned above.

Central to quantitative LDF is Monte Carlo (MC) simulations of light transport in tissue models, including multiple Doppler shifts by red blood cells (RBC). MC was used in the first proof-of-concept study where the principles of the quantitative LDF were tested using plastic flow phantoms. An optically and physiologically relevant skin model suitable for MC was then developed. MC simulations of that model as well as of homogeneous tissue relevant models were used to evaluate the measurement depth and volume of conventional LDF systems. Moreover, a variance reduction technique enabling the reduction of simulation times in orders of magnitudes for imaging based MC setups was presented.

The principle of the quantitative LDF method is to solve the reverse engineering problem of matching measured and calculated Doppler power spectra at two different source-detector separations. The forward problem of calculating the Doppler power spectra from a model is solved by mixing optical Doppler spectra, based on the scattering phase functions and the velocity distribution of the RBC, from various layers in the model and for various amounts of Doppler shifts. The Doppler shift distribution is calculated based on the scattering coefficient of the RBC:s and the path length distribution of the photons in the model, where the latter is given from a few basal MC simulations.

When a proper spectral matching is found, via iterative model parameters updates, the absolute measurement data are given directly from the model. The concentration is given in g RBC/100 g tissue, velocities in mm/s, and perfusion in g RBC/100 g tissue × mm/s. The RBC perfusion is separated into three velocity regions, below 1 mm/s, between 1 and 10 mm/s, and above 10 mm/s. Furthermore, the measures are given for a constant output volume of a 3 mm^3 half sphere, i.e. within 1.13 mm from the light emitting fiber of the measurement probe.

The quantitative LDF method was used in a study on microcirculatory changes in type 2 diabetes. It was concluded that the perfusion response to a local increase in skin temperature, a response that is reduced in diabetes, is a process involving only intermediate and high flow velocities and thus relatively large vessels in the microcirculation. The increased flow in higher velocities was expected, but could not previously be demonstrated with conventional LDF. The lack of increase in low velocity flow indicates a normal metabolic demand during heating. Furthermore, a correlation between the perfusion at low and intermediate flow velocities and diabetes duration was found. Interestingly, these correlations were opposites (negative for the low velocity region and positive for the mediate velocity region). This finding is well in line with the increased shunt flow and reduced nutritive capillary flow that has previously been observed in diabetes.

Populärvetenskaplig sammanfattning

Laserdopplerbaserad flödesmätning (LDF) är en av få tekniker som på ett icke invasivt (oblodigt) sätt kan mäta blodflödet i kroppens minsta kärl, mikrocirkulationen. Tekniken grundar sig på den mikroskopiska frekvensförändring som uppstår då ljus sprids av ett objekt i rörelse, ett fenomen som benämns dopplerskift. De första lyckade försöken att använda den här tekniken på vävnad genomfördes under 1970-talet och grunderna till alla dagens kommersiella system baserar sig på teknik som utvecklades fram till början av 1990-talet, då de första bildgivande systemenen togs fram.

Tyvärr är tekniken behäftad med en del begränsningar som åtminstone delvis orsakat att den inte har fått större kliniskt genomslag trots dess unika egenskaper och att det är en relativt billig teknik jämfört med annan medicinsk utrustning. Man kan till exempel endast mäta flödet i relativa enheter och mätvolymen är okänd och ändras mellan olika mätpunkter och även då blodflödet förändras. Vidare är måttet inte linjärt mot blodflödet då fraktionen blod i vävnaden ökar vilket gör att man ofta underskattar en flödesförändring. Dessutom får man ingen information om vilken hastighetsfördelning flödet har.

I avhandlingen beskrivs en metod att analysera mätsignalen som eliminerar ovan nämnda begränsningar. Metoden kallas för kvantitativ LDF vilket syftar på att den mäter blodflödet i vedertagna fysiologiska enheter i en bestämd och avgränsad volym. Den nya metoden skiljer sig markant från den klassiska analystekniken då den är baserad på omfattande beräkningar på matematiska vävnadsmodeller. Metoden bygger på nyvunnen kunskap de senaste tjugo åren om hur ljuset interagerar med vävnad och har möjliggjorts av den snabba datorutvecklingen.

En simuleringsteknik som kallas för Monte Carlo har använts flitigt i utvecklingen av metoden och den finns även med som en integrerad del i metoden. Monte Carlo baseras på att man slumpvis genererar en serie händelser utifrån kända eller uppskattade sannolikhetsfördelningar. När man slumpar ut tillräckligt många förlopp av en serie händelser får man i genomsnitt fram ett tillförlitligt resultat – de stora talens lag. Monte Carlo används inom många olika discipliner, allt ifrån att beräkna hur man snabbast fyller alla platser i ett flygplan med passagerare till att analysera komplexa ekonomiska system. Den kan också användas för att beräkna hur ljus transporteras inuti vävnad, där ljuset sprids många gånger, vilket alltså varit användningsområdet denna avhandling.

Avhandlingen grundar sig på sex vetenskapliga artiklar. Den första artikeln beskriver principerna bakom kvantitativ LDF och visar att de fungerar vid mätningar på en flödesmodell med plastslang. Den andra artikeln beskriver en matematisk modell av huden som är lämplig att använda i Monte Carlo-simuleringar. En generalisering av den modellen används i den slutliga metoden. Den tredje artikeln handlar om en effektiv metod för att minska simuleringstiden speciellt då man vill simulera resultatet av ett bildgivande system med hjälp av Monte Carlo. Den fjärde artikeln handlar om mätdjup och mätvolym i vanlig LDF och hur de påverkas både av olika vävnadstyper och olika blodflöden och av parametrar som har med mätinstrumentet att göra. Kunskapen från den artikeln har varit en viktig del i utvecklingen av den slutliga metoden.

Den kvantitativa LDF-metoden beskrivs i artikel fem. Den baseras på att data som beräknas från en anpassningsbar modell matchas mot mätsignaler, genom att i en iterativ process uppdatera parametrarna i modellen. När matchningen mot mätsignalerna, som innehåller mycket mer information än det som presenteras i vanlig LDF, är god drar man slutsatsen att modellen återspeglar vävnaden väl. Vävnadens blodflöde ges sedan direkt av modellen där blodflödet är känt. Man kan därför presentera blodflödet i enheten "gram röda blodkroppar per 100 gram vävnad multiplicerat med hastigheten i mm/s". Detta mått kan man dela in i tre olika hastighetsregioner för att skilja på flöde med låga hastigheter,

medelhöga, respektive höga hastigheter. Dessutom ges detta flödesmått som medelvärdet av flödet i en 3 mm^3 stor volym som har formen av en halvsfär.

Metoden har använts för att studera de mikrocirkulatoriska förändringar som inträffar vid diabetes typ 2, så kallad åldersdiabetes. Detta handlar den sjätte och sista artikeln om. Den första slutsatsen från den studien var att det kraftigt förhöjda blodflödet som inträffar när man värmer en liten del av vävnaden är mindre förhöjt hos diabetiker än hos icke-diabetiker. Detta visste man redan tidigare, men vad man tidigare inte kunnat mäta med vanlig LDF är att det förhöjda blodflödet sker i den delen av flödet som har en medelhög och hög hastighet och därmed är relaterat till de lite större kärlen i mikrocirkulationen. Fynden är logiska och förklaras av de fysiologiska processer som blir aktiverade när man utför den här typen av värmning. Ännu intressantare var att vi såg en koppling mellan hur länge man haft diabetes och blodflödet i den lägsta och i den medelhöga hastighetsregionen. Det intressanta ligger i att kopplingen är motsatt för flödet i dessa två hastighetsregioner – flödet i den låga hastighetsregionen blir lägre ju längre man haft sjukdomen, medan flödet i den medelhöga regionen blir högre. Detta är ett tecken på att flödet i kroppens allra minsta kärl, kapillärerna, där flödeshastigheten är låg, delvis är förbikopplat och istället går via större kärl, så kallade shuntar, där hastigheten är högre. Detta är missgynnsamt eftersom kapillärerna är det huvudsakliga stället där syre och andra livsviktiga ämnen övergår från blodet till kroppens celler och restprodukter som koldioxid och annat går motsatt väg. En stor del av de komplikationer som kan uppstå vid diabetes är kopplade till dessa mikrocirkulatoriska förändringar. Den nya tekniken ger möjligheter att studera sjukdomens påverkan på de minsta kärlen på ett sätt som aldrig tidigare varit möjligt.

Populärwissenschaftliche Zusammenfassung

Laserdopplerbasierte Flussmessung (LDF) ist eine der wenigen Techniken, mit der man den Blutfluss in den kleinsten Gefäßen des Körpers – die Mikrozirkulation – nichtinvasiv, d.h. ohne Eingriff in den Körper, messen kann. Das Verfahren beruht auf der mikroskopisch kleinen Frequenzänderung, die entsteht, wenn Licht an sich bewegenden Objekten gestreut wird. Dieses Phänomen wird als Dopplerverschiebung bezeichnet. Die ersten erfolgreichen Versuche, diese Technik an Körpergewebe anzuwenden, wurden in den 1970er Jahren durchgeführt. Allen heute auf dem Markt befindlichen Systemen liegt Ausrüstung zugrunde, die bis zum Beginn der 1990er Jahre entwickelt wurde, als das erste bildgebende System präsentiert werden konnte.

Obwohl die Ausrüstung verglichen mit anderen medizinischen Systemen relativ preiswert ist, ist ein größerer klinischer Durchbruch ausgeblieben. Dafür sind zumindest teilweise Begrenzungen verantwortlich, mit denen die Technik behaftet ist. Beispielsweise kann man den Blutfluss nur in relativen Einheiten messen. Zudem ist das Messvolumen unbekannt und variiert zwischen verschiedenen Messpunkten sowie bei Veränderungen des Blutflusses. Außerdem ist das Maß nicht linear zum Blutfluss, wenn der Anteil Blut im Gewebe zunimmt. Deshalb werden Blutflussveränderungen häufig unterschätzt. Das Verfahren liefert des Weiteren keine Information über die Geschwindigkeitsverteilung des Blutflusses.

In der vorliegenden Dissertation wird eine Methode zur Analysierung des Messsignals beschrieben, wobei die oben genannten Begrenzungen eliminiert werden. Die Methode wird als quantitative LDF bezeichnet. Dies bezieht sich darauf, dass der Blutfluss anstelle des relativen Maßes in üblichen physiologischen Einheiten gemessen und für ein bestimmtes und abgegrenztes Volumen angegeben wird. Die neuartige Methode unterscheidet sich markant von der herkömmlichen Analysetechnik, da sie auf umfassenden Berechnungen an mathematischen Gewebemodellen beruht, die durch die schnelle Weiterentwicklung der Computer ermöglicht werden. Die Methode baut auf neugewonnenen Kenntnissen der letzten 20 Jahre auf, wie das Licht mit Gewebe interagiert.

Zur Entwicklung der Methode wurde ein als Monte Carlo bezeichnetes Simulations-verfahren herangezogen, das auch in der Methode selbst angewendet wird. Monte Carlo basiert darauf, dass man ausgehend von bekannten oder geschätzten Wahrscheinlichkeits-verteilungen zufällig eine Serie von Ereignissen generiert. Werden genügend Verläufe einer Serie Ereignisse erzeugt, erhält man gemäß dem Gesetz der großen Zahlen im Mittel ein zuverlässiges Ergebnis. Monte Carlo wird in vielen verschiedenen Gebieten angewendet – von der Berechnung, wie man am schnellsten alle Sitzplätze in einem Flugzeug mit Passagieren besetzt, bis zur Analyse komplexer wirtschaftlicher Systeme – und eben die in der vorliegenden Arbeit durchgeführte Berechnung des Lichttransportes im Gewebe, bei dem das Licht mehrfach gestreut wird.

Die Dissertation gründet sich auf sechs wissenschaftlichen Publikationen. Der erste Artikel beschreibt das Prinzip quantitativer LDF und zeigt, dass es bei Messungen an einem Flussmodell mit Plastikschlauch funktioniert. Im zweiten Artikel wird ein mathematisches Modell der Haut vorgelegt, das sich zur Anwendung in Monte Carlo Simulationen eignet. Eine Verallgemeinerung dieses Modells wird in der neuartigen Methode angewendet. Der dritte Artikel behandelt eine effektive Methode zur Minimierung der Simulationszeit. Dabei wird speziell auf den Fall eingegangen, dass das Ergebnis eines bildgebenden Systems mit Monte Carlo simuliert werden soll. Der vierte Artikel handelt von Messtiefe und Messvolumen in herkömmlicher LDF und wie sie von unterschiedlichen Gewebearten und Blutflüssen als auch von Parametern, die das Messinstrument betreffen, beeinflusst werden. Die Erkenntnisse aus diesem Artikel waren ein wichtiger Teil zur Entwicklung der neuen Messmethode.

Die quantitative LDF-Methode wird in Artikel fünf beschrieben. Anhand eines Modells errechnete Daten werden dabei mit Messsignalen abgeglichen, indem die Parameter des Modells in einem iterativen Prozess aktualisiert werden. Aus zufriedenstellendem Abgleich schließt man, dass das Modell das Gewebe gut widerspiegelt. Somit kann der Blutfluss im Gewebe direkt aus dem Modell abgeleitet werden, wo der Blutfluss bekannt ist. Der Blutfluss kann daher in der Einheit „Gramm rote Blutkörperchen pro 100 Gramm Gewebe mal die Geschwindigkeit in mm/s" angegeben werden. Das Messsignal selbst enthält wesentlich mehr Information als in herkömmlicher LDF ausgenutzt wird. Damit kann man den Blutfluss in drei unterschiedliche Geschwindigkeitskomponenten einteilen, um zwischen niedrigen, mittleren und hohen Geschwindigkeiten zu unterscheiden. Das Flussmaß wird als Mittel des Flusses in einem 3 mm^3 großen halbkugelförmigen Volumen angegeben.

Die neuartige Methode wurde angewendet, um mikrozirkulatorische Veränderungen bei Diabetes Typ 2, so genannter Altersdiabetes, zu untersuchen. Die betreffenden Ergebnisse sind im letzten Artikel zusammengefasst. Aus dieser Studie konnte gefolgert werden, dass der deutlich erhöhte Blutfluss, der bei Erwärmung eines kleinen Teiles des Gewebes bei Nicht-Diabetikern zu beobachten ist, bei Diabetikern weniger erhöht ist. Dies ist seit längerem bekannt. Mit herkömmlichem Laser-Doppler konnte man bisher jedoch nicht messen, dass der erhöhte Blutfluss aus dem Teil des Blutflusses mit hoher Geschwindigkeit resultiert und damit den etwas größeren Gefäßen der Mikrozirkulation zuzuordnen ist. Dies ist eine logische Konsequenz der physiologischen Vorgänge, die bei dieser Art der Erwärmung stärker aktiviert werden. Noch interessanter war die Erkenntnis, dass zwischen der Dauer der Diabeteserkrankung und dem Blutfluss in den niedrigen und mittleren Geschwindigkeitskomponenten ein Zusammenhang besteht. Das Interessante ist, dass sich der Zusammenhang für diese beiden Komponenten entgegengesetzt auswirkt – der Blutfluss in der niedrigen Geschwindigkeitsregion nimmt mit zunehmender Dauer der Erkrankung ab, während der Blutfluss in der mittleren Region zunimmt. Dies ist ein Zeichen dafür, dass der Blutfluss an den kleinsten Gefäßen des Körpers, den Kapillaren, wo die Fließgeschwindigkeit niedrig ist, teilweise vorbeigekoppelt wird und stattdessen in größeren Gefäßen, so genannten Shunts, verläuft, wo die Geschwindigkeit größer ist. Dies wirkt sich nachteilig auf den Körper aus, da die Kapillaren die einzige Stelle sind, wo Sauerstoff und lebenswichtige Stoffe vom Blut auf die Körperzellen übergehen und Restprodukte wie Kohlendioxid vom Körper an das Blut abgegeben werden. Ein Großteil der Komplikationen, die bei Diabetes auftreten können, ist auf diese mikrozirkulatorischen Veränderungen zurückzuführen. Die neue Technik ermöglicht, den Einfluss der Krankheit auf die kleinsten Blutgefäße zu untersuchen, wie es in dieser Weise bisher nicht möglich war.

List of papers

This thesis is based on the following six papers, referenced in the text with their roman numerals:

I. Fredriksson I., Larsson M., and Strömberg T.
"Absolute flow velocity components in laser Doppler flowmetry"
Proceedings of SPIE, Optical Diagnostics and Sensing VI. 2006. 60940A

II. Fredriksson I., Larsson M., and Strömberg T.
"Optical microcirculatory skin model: assessed by Monte Carlo simulations paired with in vivo laser Doppler flowmetry"
Journal of Biomedical Optics, 2008. 13(1): 014015

III. Fredriksson I., Larsson M., and Strömberg T.
"Forced detection Monte Carlo algorithms for accelerated blood vessel image simulations"
Journal of Biophotonics, 2009. 3(2): 178-184

IV. Fredriksson I., Larsson M., and Strömberg T.
"Measurement depth and volume in laser Doppler flowmetry"
Microvascular Research 2009. 78(1): 4-13

V. Fredriksson I., Larsson M., and Strömberg T.
"Model-based quantitative laser Doppler flowmetry in skin"
In Manuscript

VI. Fredriksson, I., Larsson M., Nyström F. H., Länne T., Östgren C. J., Strömberg T.
"Microcirculatory changes in type 2 diabetes assessed with velocity resolved quantitative laser Doppler flowmetry"
In Manuscript

Postprinted versions of the above papers may be found at Linköping University Electronic Press (www.ep.liu.se).

The following papers are related to the thesis, but not included:

Lindbergh T., Larsson M., Fredriksson I., and Strömberg T.
"Reduced scattering coefficient determination by non-contact oblique angle illumination: methodological considerations"
Proceedings of SPIE, Optical Interactions with Tissue and Cells XVIII. 2007. 64350I

Lindbergh T., Fredriksson I., Larsson M., and Strömberg T.
"Spectral determination of a two-parametric phase function for polydispersive scattering liquids"
Optics Express, 2009. 17(3): 1610-1621.

Johansson J., Fredriksson I., Wårdell K., Eriksson O.
"Prediction of reflected light intensity changes during navigation and radio frequency lesioning in the brain"
Accepted for publication in Journal of Biomedical Optics

Abbreviations and nomenclature

Generally throughout this thesis, mathematical functions are written in plain, variables in *italic*, and vectors in **lower-case bold**. An italic subscript indicates a numerator, e.g. λ_i should be interpreted as "the i:th wavelength", whereas a plain subscript indicates a descriptor, e.g. λ_i should be interpreted "the incident wavelength". Furthermore, the absolute value of for example the vector $\mathbf{v}$ is expressed as v, i.e. $v = |\mathbf{v}|$.

Some symbols and abbreviations frequently used in this thesis are listed below. Some symbols may have multiple meanings, however.

α_{Gk}	Parameter in the Gegenbauer kernel (Gk) scattering phase function [-]
β	Optical frequency [Hz]
θ	Scattering angle [rad]
λ	Wavelength [nm]
μ_a	Absorption coefficient [mm^{-1}]
μ_s	Scattering coefficient [mm^{-1}]
μ_s'	Reduced scattering coefficient, $\mu_s(1 - g)$ [mm^{-1}]
ξ	Random number with a uniform distribution in the interval [0 1) [-]
ρ	Density [mm^{-3}]
σ_a	Absorption cross section [mm^2]
σ_s	Scattering cross section [mm^2]
φ	Angle between the scattering vector $\mathbf{q}$ and the velocity vector $\mathbf{v}$ [rad]
Ω	Solid angle [sr]
c_0	Speed of light in vacuum [$2.998 \cdot 10^8$ m/s] or in tissue [m/s]
f	Frequency [Hz]
g	Anisotropy factor, average cosine of scattering angle θ [-]
g_{Gk}	Parameter in the Gk scattering phase function [-]
k	Wave number [m^{-1}]
n	Refractive index [-]
$p_s(\cos\theta)$	Scattering phase function (probability density function) [-]
v	Velocity [m/s]
w	Photon weight [-]
G	Optical spectrum, i.e. spectrum of optical frequencies [Hz^{-1}]
E	Electromagnetic field [V/m]
I	Light intensity, generally normalized with some other intensity, e.g. emitted or incident intensity, [-]
P_D	Doppler power spectrum [Hz^{-1}]
$\mathbf{q}$	Scattering vector [m^{-1}]
AV	Arteriovenous
CMBC	LDF estimate of moving RBC tissue fraction (concentration of moving blood cells)
DM	Diabetes mellitus
DRS	Diffuse reflectance spectroscopy
Gk	The Gegenbauer kernel or Reynolds-McCormick scattering phase function
HCT	Hematocrit, volume fraction of blood that is occupied by RBC:s
HG	The Henyey-Greenstein scattering phase function
LDF	Laser Doppler flowmetry
LDPI	Laser Doppler perfusion imaging, imaging LDF system

LDPM   Laser Doppler perfusion monitoring, probe based LDF system
MC   Monte Carlo simulation
mfp   Mean free path length ($1/\mu_s$, $1/\mu_a$, or $1/\mu_t$)
NO   Nitric oxide
RBC   Red blood cell (erythrocyte)
RMS   Root mean square $\sqrt{\langle x^2 \rangle}$
SNR   Signal to noise ratio

Contents

1 Introduction

Laser Doppler flowmetry (LDF) is a non-invasive technique that uses laser light to estimate the microcirculatory blood flow in living tissue. In the microcirculation, or more specifically in the capillaries, the oxygen, nutrition, and waste exchange between the blood and the living cells takes place. Thus, the microcirculation is vital to the body, and to be able to accurately measure it would be a valuable clinical tool. LDF is virtually the only existing method to estimate the microcirculation non-invasively (except other laser speckle based methods), and consequently attracted much attention especially during the 1980s when the technique was new. However, due to a number of shortcomings, its broad clinical impact has not yet become a reality. In this thesis, the development of a method that works around many of those shortcomings is described.

The principle that is the basis for LDF was first demonstrated by Forrester *et al.* in 1955 [1], before the first working laser was presented. The theory was foremost developed by Forrester [2] and extended by Cummins and Swinney [3] during the 1960s before the first successful *in vivo* measurements were presented by Stern in 1975 [4]. Soon thereafter, the first fiber-optic based system was presented by Holloway and Watkins [5], and it was improved by Nilsson *et al.* [6]. The theory was further improved during the early 1980s [7-9], and the first imaging system (LDPI – laser Doppler perfusion imaging, in contrast to single point systems LDPM – laser Doppler perfusion monitoring) was presented in 1989 by Nilsson *et al.* [10], see also [11,12]. More recent methodological improvements are described briefly in Section 1.1.

LDF is currently used in a variety of fields, especially in research, including wound healing [13], assessment of burn wound depth [14], skin tumor characterization [15], amputation level determination [16,17], neurosurgery [18], and breast reconstruction [19]. Generally, it is used together with some prevocational protocol, such as local heating of the skin at the measurements site, to increase the clinical information.

The technique utilizes the small frequency shift, the Doppler shift, that arises when light is scattered by a moving red blood cell (RBC) or by any other moving particle. By analyzing the frequency content of the backscattered light that mixes on the detector, conclusions about the amount and velocity of the blood flow can be drawn. In conventional LDF, the perfusion value is calculated as the first moment of the Doppler power spectrum, and this measure reflects the tissue fraction of moving red blood cells times their average velocity. Sometimes, the zero order moment is also calculated, which reflects the tissue fraction (concentration) of moving red blood cells, CMBC. Dividing the perfusion value with CMBC thus gives the average velocity. Unfortunately, the perfusion measure, and especially the CMBC, scales non-linear to the RBC tissue fraction. Furthermore, the CMBC measure is uncertain due to high fluctuations at low frequencies, where most of the signal energy is present. That also makes the average velocity measure uncertain. The three measures mentioned above, the perfusion, CMBC, and average velocity, are not given in physiologically relevant units, reflect an unknown measurement volume, and are affected by tissue absorption and scattering in an uncontrolled manner. That makes intra- and inter-individual comparisons troublesome.

During the last two decades, the knowledge of how to accurately measure optical properties of tissue has increased drastically. The Monte Carlo technique for simulating light transport in a highly scattering and geometrically complex medium has also been developed, and the possibility to perform these simulations on a large scale has opened up due to the rapid development of computer hardware. Therefore, it is now possible to develop physiologically and optically relevant adaptive tissue models, and to adapt these models to measured data on real tissue using a reverse engineering approach.

This thesis describes the development of a quantitative laser Doppler flowmetry method that gives output data in physiologically relevant units. The core of the method is an optical tissue model that is adapted to Doppler power spectra originating from measurements. The included papers cover proof-of-concept using a flow phantom [I], tissue model development [II], Monte Carlo simulation improvements [III], measurement depth and volume estimation [IV], method description and evaluation [V], and a clinical evaluation [VI]. It is interesting to note that the possibility to develop a method like this was already foreseen by Stern in his paper from 1975 [4], where he stated that "In principle it is possible to recover the cell speed distribution from the measured spectrum", and "Because it [the Doppler power spectrum] provides information about the flow velocity distribution, it has the potential ability to analyse the distribution of flow in the different microvascular compartments".

1.1   Recent LDF improvements

Until the beginning of the 1990s, most of the improvements made in the field of LDF were foremost related to the hardware, including the development of LDPI. Since then, many of the improvements involve the signal analysis. For further references, a comprehensive review about methodological developments in LDF has recently been published by Rajan *et al.* at the Twente group. [20]

One branch of LDF research involves spectral analysis of the conventional perfusion signal using for example simple spectrograms or wavelets. [21-24] By studying the frequency content of the perfusion signal, the vasomotion of the microcirculation can be studied and conclusions about the microcirculation can be drawn. Normally in skin, three frequency peaks are found except for the peaks correlated to the heart beats and breathing, at about 0.1, 0.04, and 0.01 Hz. It is suggested that the 0.1 Hz component reflects the activity of the smooth muscle of the vessels, that the 0.04 Hz component reflects the neurogenic stimulation of the small arteries, and that the 0.01 Hz component is correlated to metabolic changes. [22]

A couple of methods have been presented that enable measurements at large depths in the order of centimeters. [25-27] Common for the techniques is that a long source-detector separation was used in combination with a high power and/or pulsed laser. In the method presented by Lohwasser and Soelkner [25] the average RBC velocity was estimated by investigating the logarithmic slope of the Doppler power spectra, an estimation that they found worked well at large source-detector separations.

One of few LDF improvements over the last decades relying on a large modification of the hardware is the path-length resolved LDF instrument. [28,29] This instrument is based on a Mach-Zender interferometer, and by tuning the position of the reference arm, photons that have traveled a specific path-length can be selected. The advantage of this instrument is not only that some conclusions about the measurement depth can be drawn based on the path length, but more importantly that the influence of optical properties on the perfusion estimate, which is generally seen as a problem in LDF, can be reduced.

Methods for a velocity resolved perfusion measure have previously been presented by Dörschel and Müller, Liebert *et al.*, and Larsson and Strömberg. [30-33] These methods only work in the single-shift regime, i.e. for very low blood tissue fractions, which is a major drawback. In the method presented by Dörschel and Müller, a constant scattering angle was also assumed, which must be questioned. Nevertheless, the method described by Larsson and Strömberg constituted the starting point of the quantitative LDF method presented in this thesis.

Others have used multiple source-detector separations [34] and multiple wavelengths [35,36] to be able to differentiate between different measurement depths and thus draw further conclusions about the microcirculation.

1.2   Related techniques

Before the development of LDF, the xenon washout technique [37] and the radioactively labeled microsphere technique [38,39], were the main alternatives to measure the microcirculatory blood flow. The obvious disadvantage of injecting radioactive substances into the blood greatly limits their usefulness.

Ultrasound Doppler techniques are widely used to measure the blood flow in larger vessels but the spatial resolution is insufficient for the microcirculation, when not using modern contrast agents. The ultrasound Doppler technique measures, in contrast to LDF, the blood flow in a single directional component only.

Since the surface temperature of the tissue is related to the blood flow, thermography can be used as an estimator of the blood flow. [40-42] The method presents a map of the surface temperature at video speed, but its disadvantage as an estimator of blood flow is that temperature and blood are not directly connected.

A number of optical and non-invasive techniques, other than LDF, exist that can provide information about the blood flow. The most direct method is capillary microscopy, where the capillaries, mostly in the nailfold where they are oriented parallel to the skin surface, are studied individually. [43] The blood velocity can be estimated by inspecting the spatial dislocation of the RBC:s frame by frame. Another variant of capillary microscopy studies the number of active (visible) capillary loops in a certain area. [44] This technique is not limited to the nailfolds but is unable to measure the blood flow velocity.

Other optical methods like photoplethysmography (PPG), pulse oximetry, and diffuse reflection spectroscopy all rely on the absorption of blood to estimate the blood volume and oxygen saturation. However, they give no flow information.

In optical Doppler tomography (ODT, based on optical coherence tomography), the spatial distribution of the microvascular flow can be studied. [45] As Doppler ultrasound, it is sensitive to the direction of the flow. Disadvantages compared to LDF involve a very limited measurement depth and high cost.

Diffusing wave spectroscopy (DWS) is similar to LDF but is based on the diffusion approximation and operates at large source-detector separations accompanied with strong multiple Doppler shifts. [46-48] Due to the large source-detector separations and the accompanied large measurement volume, DWS is not suitable for evaluating the microcirculation since the output will be dominated by larger high flow velocity vessels.

Laser speckle techniques analyze the temporal and spatial changes in the speckle pattern formed on the detector, according to Section 5.2. [49] The de-correlation time or the speckle contrast at various integration times is related to the blood flow, and the technique can therefore relatively simply be implemented using an ordinary CCD or CMOS camera, to give a full-field perfusion map close to real time. Compared to LDF, the technique gives no spectral information which reduces the possibilities for complex data analysis methods, such as quantitative LDF.

2   Aim

The aim of this thesis was to evaluate the possibilities for a fundamentally new method for data analysis in laser Doppler flowmetry, using a model-based reverse engineering approach. The purpose was to develop a method for quantitative velocity resolved laser Doppler flowmetry with:

- RBC flow velocities measured in **mm/s**
- RBC tissue fraction measured in **g RBC / 100 g tissue**
- perfusion measured in **g RBC / 100 g tissue × mm/s**
- predetermined and geometrically defined output volume in **mm³**

for facilitating the physiological interpretation of LDF perfusion estimates.

3   Principles of light absorption and scattering

For a thorough understanding of the complex nature of light, electromagnetic theory and quantum theory is needed. However, depending on the application, less complex approaches may be suitable. For large geometries, light propagation may be described by ray optics and Snell's and Fresnel's laws, which are dependent upon the refractive index mismatch between media (see Section 3.2) and common trigonometry.

In biomedical optics, ray optics is most often inadequate to describe the propagation of light though. Instead, a wave and/or particle representation may be appropriate. With wave optics, phenomena such as interference, polarization, and, central in this thesis, the Doppler effect, can be described. The particle representation, on the other hand, offers an intuitive representation of energy transfer and absorption and scattering, although it fails to fully describe the underlying processes of these phenomena. The particle representation can even be used to quantify the Doppler effect, despite the close connection between the Doppler effect and wave optics (see Chapter 5). When using the Monte Carlo technique to simulate light propagation (see Chapter 4), a particle representation where the particles are given certain wave properties is used.

In this chapter, the concepts of absorption and scattering are presented to give a basic bio-optical background to the rest of the thesis. Also how to measure the absorption and scattering coefficients and the scattering phase function is described briefly.

3.1   Absorption

During an absorption event, the energy of a photon is transferred to a molecule or a single, unbounded atom. This energy transmission causes the molecule or atom to increase its internal energy state, from one energy level to another, called a transition, as described by the quantum theory. Only certain transitions are allowed, increasing either of the electronic, vibrational, or rotational energies, where the latter two are not possible for free atoms, but only for molecules. The energy level of a transition is dependent on the structure and composition of the molecule, and therefore, each molecule has a unique absorption spectrum. [50] Biological molecules are often large and have a complex structure, and the combinations of transitions in such molecules are thus nearly infinite. Therefore, their absorption spectra are in principle continuous with a smooth shape (see for example Figure 3.1).

The efficiency of an absorbing particle at a certain wavelength is denoted absorption cross section, σ_a, and is given by the geometrical cross section of the particle, weighted with an absorption efficiency factor. The dimension of σ_a is therefore mm^2. Given the number density of absorbers in a medium, ρ_a (mm^{-3}), its absorption coefficient is given by $\mu_a = \rho_a \sigma_a$. It follows that the dimension of μ_a is mm^{-1}, and μ_a can be interpreted as the average number of absorption events per mm. The inverse of μ_a is maybe more intuitive; the mean path length d_{mfp} of photons propagating through the media before being absorbed. [50,51] Beer-Lambert's law:

$$I = I_0 e^{-d\mu_a}, \hspace{3cm} (3.1)$$

describes how the light intensity I decays with the penetration distance d through an absorbing material, where I_0 is the intensity of the incident light.

Three predominant absorbers in the visible and near infrared wavelength region are found in human skin: melanin (eumelanin) in the epidermal layers; hemoglobin in the

blood in the dermis; and water, see Figure 3.1 and also Section 6.1. [52] All these absorbers are relatively weak in the wavelength interval 600-900 nm, which makes this region particularly suitable for bio-optical diagnostics, e.g. LDF. Hemoglobin and water are also predominant in other types of tissue.
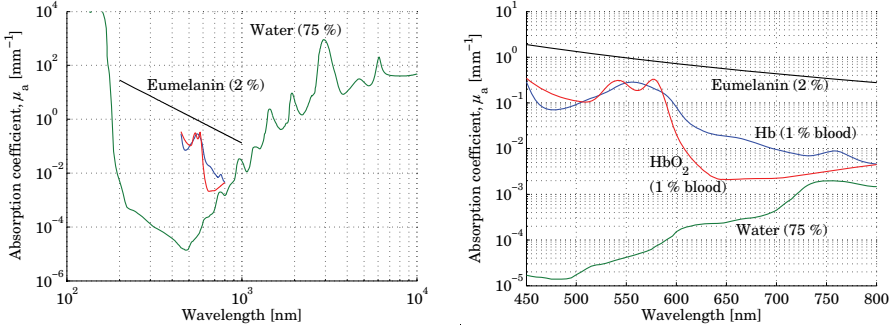

Figure 3.1: Absorption spectra of eumelanin, hemoglobin (reduced and oxygenated, 150 g Hb/liter blood), and water, at realistic tissue fractions in epidermis (eumelanin) and dermis (blood and water). [53-55]

3.2   Scattering

When an electromagnetic wave (e.g. light) propagates through any medium, its energy is constantly transferred to the particles of the medium, creating oscillating dipoles. These oscillations instantly re-radiate new waves, with the same wavelength as the incoming wave, in all directions. In a homogeneous medium, where the particles are organized in an ordered pattern giving a constant refractive index, the waves re-radiated in all directions except the forward direction are cancelled out due to total destructive interference. Therefore, the result is a light beam propagating in the forward direction only. [56]

When the ordered pattern of the particles is disturbed, causing a local change of the refractive index, the re-radiated waves will produce other interference patterns. Thus, such refractive index inhomogeneities cause the light to propagate in other directions than the forward direction – scattering has occurred. The scattering angle is strongly dependent on the size and shape of the objects. [51,56] When the object is much larger than the wavelength, i.e. within the so-called geometric limit, destructive interference occurs in all directions except two. A fraction of the light is reflected at the boundary and the rest of the light is refracted with a deterministic angle as it is transmitted into the object. For $\theta_i > \sin^{-1}(n_t/n_i)$, all light is reflected, else the angle of refraction is given by Snell's law:

$$n_i \sin \theta_i = n_t \sin \theta_t, \tag{3.2}$$

where n_i and n_t are the refractive indices of the object and the surrounding medium, and θ_i and θ_t are the angles of incidence and transmittance, respectively. For unpolarized light, the fraction of reflected light, r, also called specular reflectance, can be calculated using Fresnel's formula:

$$r = \frac{1}{2} \left(\frac{\sin^2(\theta_i - \theta_t)}{\sin^2(\theta_i + \theta_t)} + \frac{\tan^2(\theta_i - \theta_t)}{\tan^2(\theta_i + \theta_t)} \right). \tag{3.3}$$

For very small particles, much smaller than the wavelength of light (less than approximately $\lambda/15$, the Rayleigh regime), very little destructive interference occurs in the re-radiated waves. This type of scattering is called Rayleigh scattering, and due to the small degree of destructive scattering, the scattering occurs with almost the same intensity in all directions.

In analogy with absorption, the efficiency of a scattering particle is given by the scattering cross section σ_s, and the scattering coefficient μ_s of a medium is calculated as $\mu_s = \rho_s \sigma_s$. For the small scattering particles in the Rayleigh regime, σ_s tends to decrease with wavelength as λ^{-4}. This explains why the sky is blue during daytime and red in daybreak and sunset. During daytime the light propagates a rather short distance through the atmosphere and yellow and red light are therefore scattered to a minor extent. Blue light on the other hand, which has a short wavelength, is scattered out from the original path and thus seems to originate from all over the sky. During daybreak and sunset the light propagates a very long distance through the atmosphere due to the flat angle. Then, the blue light that is scattered extensively is eventually absorbed before reaching the observer, whereas the red light is scattered to an amount comparable to blue light during daytime. For the same reason, the sunset seems longer in areas where air pollution is high, since the blue light is absorbed to a greater extent there. [56]

The distribution of scattering angles θ is described by a scattering phase function $p_s(\cos\theta)$. For spherical homogeneous objects and a few other simple geometries, the phase function can be calculated using for example Mie theory. Mie theory can also be used to calculate the scattering cross section σ_s for such objects. Large objects, compared with the wavelength, with a small difference in refractive index compared to the surrounding medium generally result in a greater extent of forward scattered light, and vice versa.

The mean cosine of the scattering angle is referred to as the anisotropy factor, g, and describes the level of forward scattering. A value of 0 indicates equal amounts of forward and backward scattering, where a special case is isotropic scattering, i.e. equal scattering in all directions. A value close to 1 indicates strong forward scattering, i.e. a small change in the direction of propagation. A red blood cell (RBC) is an example of a particle with a very high anisotropy factor (about 0.991 at 780 nm [II]). Since strong forward scattering of a medium leads to less effective scattering, i.e. more scattering events are needed for the light to turn around, the scattering coefficient μ_s and the anisotropy factor are sometimes combined into the reduced scattering coefficient $\mu_s' = \mu_s(1 - g)$. Using this substitution, a medium can be described as isotropic scattering with the scattering coefficient μ_s'. Generally, this substitution is valid when studying the light a couple of reduced men free path lengths $d_{mfp'} = 1/\mu_s'$ away from the light source in an infinite homogeneous medium. When studying the light much closer than one $d_{mfp'}$ from the source or in a non-homogeneous medium, not only g but also higher order moments of the scattering phase function must be considered for a proper description of the light transport.

Generally, for a constant volume tissue fraction of scatterers, both μ_s and g increase with the particle size when the size of the particle is comparable to the wavelength, causing μ_s' to remain rather constant. For example, the RBC:s in blood of normal hematocrit scatters with approximately $\mu_s = 222$ mm^{-1} and $g = 0.991$ at 780 nm, whereas dermis tissue that is constituted by smaller structures such as collagen fibers and subcellular structures [53] has scattering properties of $\mu_s = 13$ mm^{-1} and $g = 0.85$ at the same wavelength. The reduced scattering coefficient for both blood and dermis is thus about 2 mm^{-1}. [II]

The structure of scattering particles in biological tissue is usually complex which makes Mie calculations of the phase function impossible. Approximate empirical phase functions are therefore used instead. The most common phase function in bio-optics is the Henyey-Greenstein (HG) phase function that has been found to resemble the phase function of many biological tissues well. [57] It is expressed as:

$$p_{HG}(\theta) = \frac{1}{4\pi} \frac{1 - g_{HG}^2}{(1 + g_{HG}^2 - 2g_{HG}\cos\theta)^{3/2}}, \tag{3.4}$$

where g_{HG} equals the anisotropy factor g. Combinations of HG phase functions with different anisotropy factors are also often used. Another common phase function, related to HG but more general, is the two parametric Gegenbauer kernel (Gk) or Reynolds-

McCormick phase function, developed especially to describe the phase function of blood and other biological particles. [58] It is given by:

$$p_{\mathrm{Gk}}(\theta) = \frac{\alpha_{\mathrm{Gk}} g_{\mathrm{Gk}} (1 - g_{\mathrm{Gk}}^2)^{2\alpha_{\mathrm{Gk}}}}{\pi((1 + g_{\mathrm{Gk}})^{2\alpha_{\mathrm{Gk}}} - (1 - g_{\mathrm{Gk}})^{2\alpha_{\mathrm{Gk}}})(1 + g_{\mathrm{Gk}}^2 - 2g_{\mathrm{Gk}} \cos\theta)^{\alpha_{\mathrm{Gk}}+1}}. \tag{3.5}$$

Note that this reduces to Equation 3.4 for $\alpha_{\mathrm{Gk}} = 0.5$. The anisotropy factor of the Gk phase function is given by the expression:

$$g = \left(2g_{\mathrm{Gk}}\alpha_{\mathrm{Gk}} \frac{(1 + g_{\mathrm{Gk}})^{2\alpha_{\mathrm{Gk}}} + (1 - g_{\mathrm{Gk}})^{2\alpha_{\mathrm{Gk}}}}{(1 + g_{\mathrm{Gk}})^{2\alpha_{\mathrm{Gk}}} - (1 - g_{\mathrm{Gk}})^{2\alpha_{\mathrm{Gk}}}} - (1 + g_{\mathrm{Gk}}^2) \right) \Big/ 2g_{\mathrm{Gk}}(\alpha_{\mathrm{Gk}} - 1). \tag{3.6}$$

An example of a Mie scattering phase function from a relatively large object with a small refractive index mismatch can be seen in Figure 3.2. The object is a spherical approximation of an RBC with a volume of 90 μm^3 (radius 2.8 μm), refractive index of 1.40, and the surrounding plasma with a refractive index of 1.34. The resulting phase function is strongly forward scattering with an anisotropy factor of 0.993 at 780 nm. In this figure, the Gk phase function approximation of blood from Paper II, with $\alpha_{\mathrm{Gk}} = 1.0$ and $g_{\mathrm{Gk}} = 0.948$, resulting in $g = 0.991$, as well as the HG phase function with $g = 0.991$, are also shown. The spherical approximation of the RBC results in a slightly higher anisotropy factor for the Mie phase function than for the Gk phase function approximation. Also note that all RBC:s are normally not equally sized, and a mean Mie phase function would therefore lack the sharp peaks and troughs seen in Figure 3.2 (see [II]).
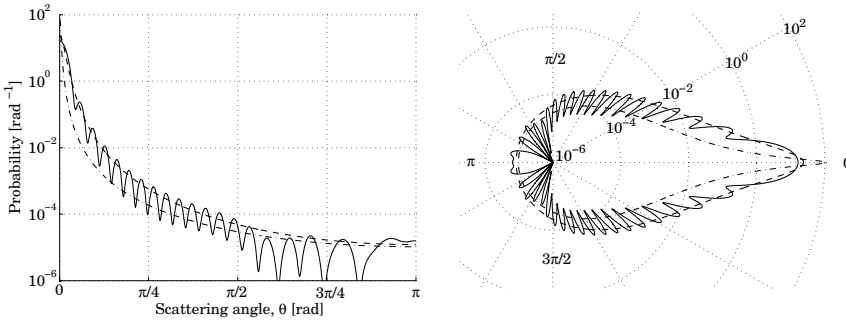

Figure 3.2: Plot of the scattering phase function of a 90 μm^3 spherical red blood cell (solid line), Gk phase function approximation of RBC:s from Paper II (dashed line), and HG phase function with the same anisotropy factor as the Gk phase function (dash-dotted line).

3.3   Measurement of optical properties

There exist a great number of methods to measure or estimate the optical properties of a medium. Some of the most common methods used today are briefly described in this section. An excellent overview of various methods and the theories behind them has previously been presented by Wilson. [59] It is interesting to notice that, in practice, all methods presented here except collimated transmission rely on the solution of an inverse problem. Furthermore, although most of the methods were based on the diffusion approximation when developed, it has been shown that the results are more reliable when using Monte Carlo simulations (see Chapter 4).

3.3.1 Collimated transmission

The most straightforward method to measure the total attenuation coefficient μ_t, i.e. $\mu_a + \mu_s$, is the use of collimated transmission. [60,61] This method directly makes use of Beer-Lamberts law (Equation 3.1). Taking the logarithm of Beer-Lamberts law:

$$\log(I) = \log(I_0) - \mu_t d, \tag{3.7}$$

one can realize that μ_t can be solved by varying the thickness d of the sample in at least two steps. The light incident on the sample, as well as the detected light, has to be collimated for this method to work. Figure 3.3 shows one variant of a collimated transmission setup.

Because the method makes use of transmitted light, it is not suitable for *in vivo* measurements. The samples used must also be rather thin, which could be troublesome to achieve for solid samples. Finally, the method performs poorly on highly forward scattering media, such as blood, due to the difficulty to separate forward scattered and non-scattered light.
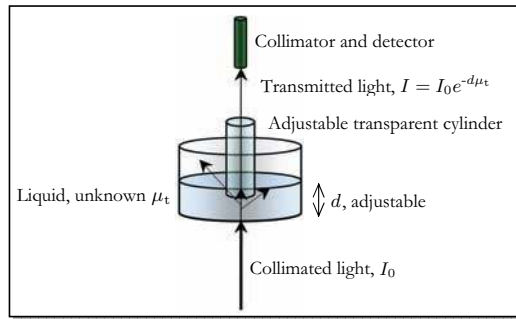

Figure 3.3 The principle of a collimated transmission setup.

3.3.2 Goniometry

A goniometer is, in theory, a simple device that detects the scattered light intensity in various scattering directions. It can thus be used to directly measure the scattering phase function. However, to compensate for multiple scattering and refractive index mismatches, it may be used in combination with MC simulations or other compensation techniques [62].

Goniometry suffers from the same disadvantages as the collimated transmission setup. It also suffers from some practical difficulties in the construction. It is however the only accepted method to measure the scattering phase function of a medium. Rather than measuring the phase function itself, other methods generally estimate one (the anisotropy factor) or more parameters of the phase function.
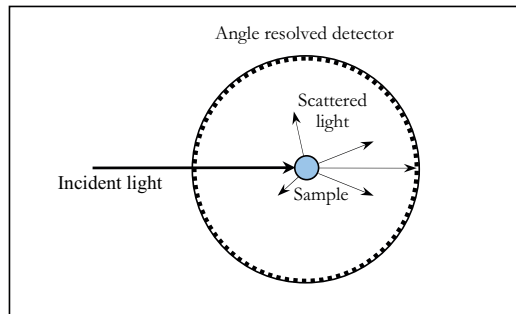

Figure 3.4 A simple goniometric setup.

3.3.3 Integrating spheres

An integrating sphere is a sphere whose interior is covered with a highly reflective material, e.g. barium sulfate. The light entering the sphere is detected independent of the incident direction, by a small detector in the wall of the sphere. By using a double integrating sphere with the sample between the spheres, the reflected and backscattered light into the first sphere and the transmitted light into the second sphere can be measured to calculate μ_s' and μ_a. [63,64] Combining the measurements with collimated transmission measurements allows for separation of μ_s' into μ_s and g. Figure 3.5 shows a schematic of the integrating sphere setup. Alternatively, a third detector can be placed to the right of the transmittance sphere to measure collimated transmitted light as well.

Integrating sphere measurements suffer from the same disadvantages as collimated transmission measurements and are generally sensitive to imperfections in the setup. For correct calculations of μ_s' and μ_a, MC simulations are usually used today. [64,65]
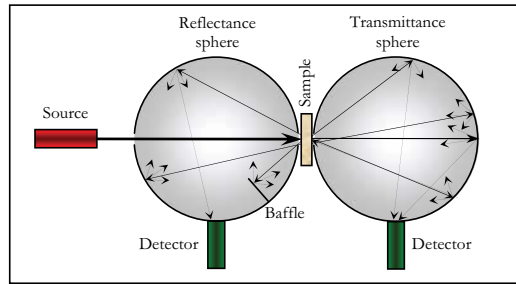

Figure 3.5 Schematic of integrating sphere measurements.

3.3.4 Spatially resolved diffuse reflectance

All three methods presented above require transmission of the light through the sample and knowledge about the sample geometry. That makes the methods unsuitable for *in vivo* measurements. The remaining methods presented here operate in reflectance mode, which enables the first four of them to be used *in vivo*, often with the assumption that the tissue of interest is homogeneous and larger than the sampling volume.

By inspecting the intensity profile of light backscattered from a sample, its optical properties can be derived. [66-68] The intensity reduces when μ_a is increased and the intensity increases close to the illumination point and decreases further away when μ_s' increases. Furthermore, it is possible to separate μ_s and g when inspecting the profile close to the illumination point. It is also possible to estimate more than the anisotropy factor of the phase function by a careful inspection close to the illumination point. [69,70] Figure 3.6 and Figure 3.7 show how the backscattered intensity profile changes with μ_a, μ_s, and g.
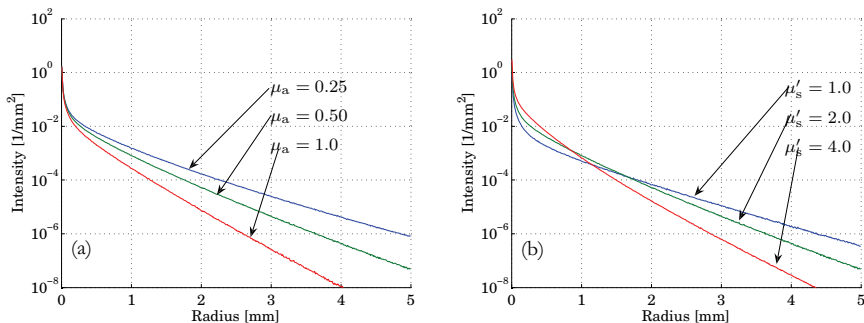

Figure 3.6 Simulated changes in backscattered intensity profile for variations in μ_a (a, constant $\mu_s = 10$ mm^{-1} and $g = 0.8$) and μ_s (b, constant $\mu_a = 0.5$ mm^{-1} and $g = 0.8$).
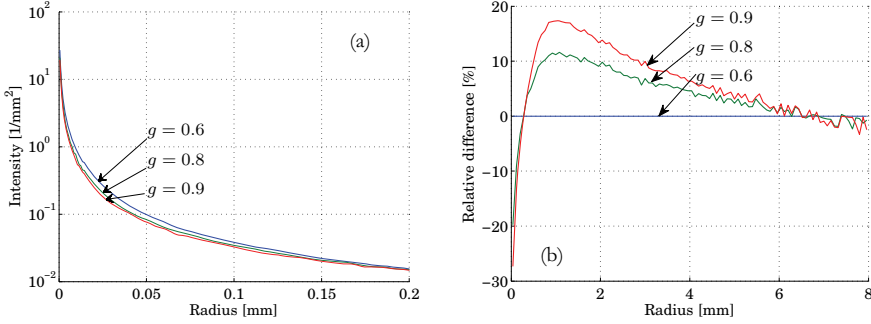
Figure 3.7(a) Simulated changes in backscattered intensity profile for variations in g (constant $\mu_a = 0.5$ mm^{-1} and $\mu'_s = 2$ mm^{-1}).
(b) The relative difference between the intensity profile with $g = 0.6$ and $g = 0.8$ and 0.9.
The photons were injected using a point source at radius 0.

To reduce the errors in the estimated optical properties, proper modeling of the light transport using MC simulations is needed. However this leads to high complexity of the method and increases the computational time. Careful calibration of the measurement system is also needed and a high spatial resolution is desired. This method as well as time resolved and frequency domain diffuse reflectance may be used together with a more complex tissue model if the assumption of homogeneity is inappropriate.

3.3.5 Oblique angle

In oblique angle measurements [71,72], a collimated laser beam is directed towards the sample with a known oblique angle α. At a distance $1/\mu'_s$ away from the point of illumination, a virtual isotropic light source will arise, giving rise to a symmetrical intensity decay at the surface. By identifying the positions of the illumination point, often approximated to the point of maximal reflected light intensity called the hot spot, and the center of the intensity decay, the distance Δr between them can be used to calculate μ'_s as

$$\mu'_s = \frac{\sin \alpha}{n \Delta r} - k\mu_a, \tag{3.8}$$

where n is the refractive index of the sample and k is a correction factor. A simulated example where $\alpha = \pi/4$, $\mu'_s = 3$ mm^{-1} ($g = 0.7$), $\mu_a = 0.1$ mm^{-1}, and $n = 1.4$ is shown in Figure 3.8. Here, the light impinges the medium in the origin of coordinates and the diffuse center is located at the dashed line. The curve approaching the diffuse center at low intensity levels indicate the center of gravity for light above the given intensity. The
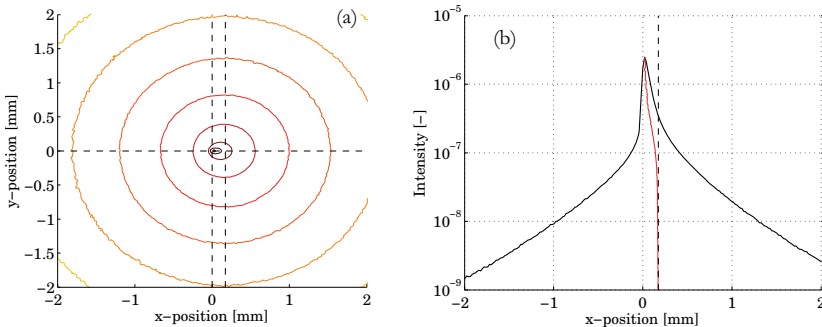

Figure 3.8 Contour plot of the reflected intensity from an oblique angle simulation (a) and plot of the reflected intensity along the x-axis at $y = 0$ (b).

distance Δr equals 0.17 mm, which with $k = 0$ results in $\mu'_s = 3.0$ mm^{-1}. However, if the hot spot was used as the approximate point of illumination, the calculated reduced scattering rather resulted in $\mu'_s = 3.4$ mm^{-1}. In the simulation, the acceptance angle of the detector was 0.025 rad, and the forced detection variance reducing method [III] was used to accelerate the simulation.

3.3.6 Time resolved spectroscopy

By illuminating a sample with short light pulses and measuring the time of flight until detection of the photons, it is possible to resolve the optical properties of the sample. This is often called time resolved spectroscopy. [73-75] To resolve the optical properties, the measurements are fitted to a model, preferably an MC model [76]. Using an MC model, the times of flights are easily calculated with knowledge of the speed of light in the sample (and fibers). Examples for variations in μ_a and μ'_s are shown in Figure 3.9. Due to the relatively large source-detector separation used in time resolved spectroscopy the technique can not separate changes in μ'_s into changes in μ_s and g.
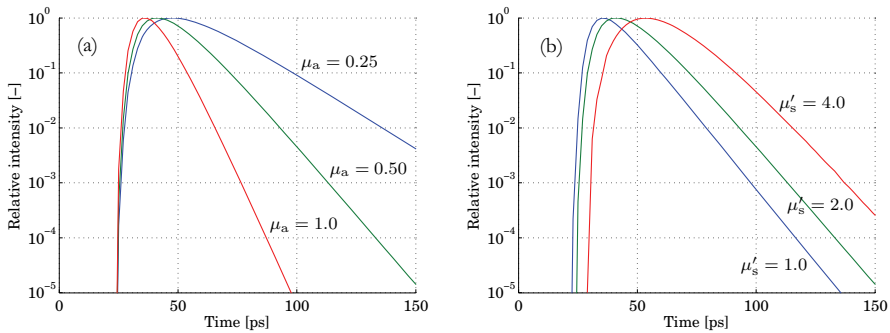

Figure 3.9 Simulated changes in backscattered time resolved profile for variations in μ_a (a, constant $\mu'_s = 2.0$ mm^{-1}) and μ'_s (b, constant $\mu_a = 0.50$ mm^{-1}). The photons were injected in a 0.25 mm diameter fiber and detected in a 0.50 mm diameter fiber 5 mm away.

3.3.7 Frequency domain spectroscopy

A method closely related to time resolved spectroscopy is frequency domain spectroscopy. [77,78] It can even be shown that the two techniques are equivalent, using the Fourier transform. [74] With this method, the light source is intensity modulated (typically in the order of 100 MHz) and the optical properties, usually μ_a and μ'_s, can be estimated by measuring the modulation (amplitude of the time varying part) and phase of the detected light intensity. As with many of the methods presented in this section, frequency domain spectroscopy was developed using the diffusion approximation, but this has been replaced by Monte Carlo simulations in recent years due to the inaccuracies and limitations accompanying the diffusion approximation. [79,80]

3.3.8 Laser Doppler flowmetry

As we will see in Chapter 5, the size of the Doppler shifts is highly dependent on the scattering angle, and the number of Doppler shifts are highly dependent on μ_s. Therefore, the scattering properties of a liquid can be derived using an LDF-setup where measured LDF-spectra are fitted to a model. [81]

With this method, μ_s and g are more easily separated than when using the methods presented above, especially for very forward scattering (g close to unity) media such as blood. This method was therefore utilized when determining the scattering phase function (Gegenbauer kernel approximation) of blood used in this thesis, see especially [II].

4   Monte Carlo simulations

Being able to describe and predict the transport of light in biological media is an important step for understanding various bio-optical methods. Due to light scattering and the fact that most biomedical methods work in reflectance mode, simple ray optics is not applicable for this description. This is contrary to the situation in medical radiology where scattering has traditionally been neglected or regarded as a somewhat troublesome factor.

Mathematically, using the particle representation of light, the transport equation can be used to describe light transport. [82] Unfortunately, no general analytic solution is known to the transport equation. The diffusion approximation of the transport equation can be used for analytical approximate solutions in some simple cases, though. It has therefore been extensively used within bio-optics, but since it is strongly limited to simple geometries, relatively large source-detector separations, and situations where $\mu_\mathrm{a} \ll \mu_\mathrm{s}'$, alternatives are needed. [83]

Monte Carlo simulations offer a numerical solution to the transport equation and operate in an intuitive manner. By simulating random walks for a great number of individual photons, the results converge to the true solution. The random walk is based on the optical properties of the medium, i.e. the absorption coefficient μ_a, the scattering coefficient μ_s, and the scattering phase function $p_\mathrm{s}(\cos\theta)$, and the refractive index n. Furthermore, it can be solved for any arbitrary complex geometry for the medium, light source, and detector.

The limitation of the Monte Carlo method is the computational speed. Since many photons are needed for correct results, the computational times needed are sometimes immense. The fast progress in computer hardware and the promising use of graphic card processors with Monte Carlo [84] make the speed issue less of a problem, though, as well as the use of post processing and variance reduction techniques.

The basics of the Monte Carlo technique are described in Section 4.1. Some variance reducing methods that increase the efficiency of the simulations are described in Section 4.2. Finally the software developed during this thesis work is briefly described in Section 4.3 together with a validation of the results generated by the software.

4.1   Basics

The Monte Carlo method as presented in this section is an extension of the method presented by Prahl [85] and Wang *et al.* [86]. The most important steps are shown in the flowchart in Figure 4.1, and are thereafter described one by one. This description is in accordance with the Monte Carlo software developed and used during the work of this thesis. Random numbers ξ, uniformly distributed between zero and unity, occur frequently in the description.

4.1.1   Launch photon

At the launch of each photon, its weight w is set to unity, and an initial position $\{x, y, z\}$ and direction unit vector $\boldsymbol{\mu} = [\mu_x, \mu_y, \mu_z]^T$ are set. The position and direction are dependent on the position, direction, and the properties, e.g. numerical aperture, of the light source. The photon position is normally uniformly chosen over the spatial spread of the light source (e.g. valid for an optical fiber), although it can also make sense to choose the position from a Gaussian distribution (e.g. for a laser source) [86]. Furthermore, the initial direction can be arbitrarily chosen, for example uniformly distributed on the unit sphere within the numerical aperture (divided by the refractive index) of the light source.
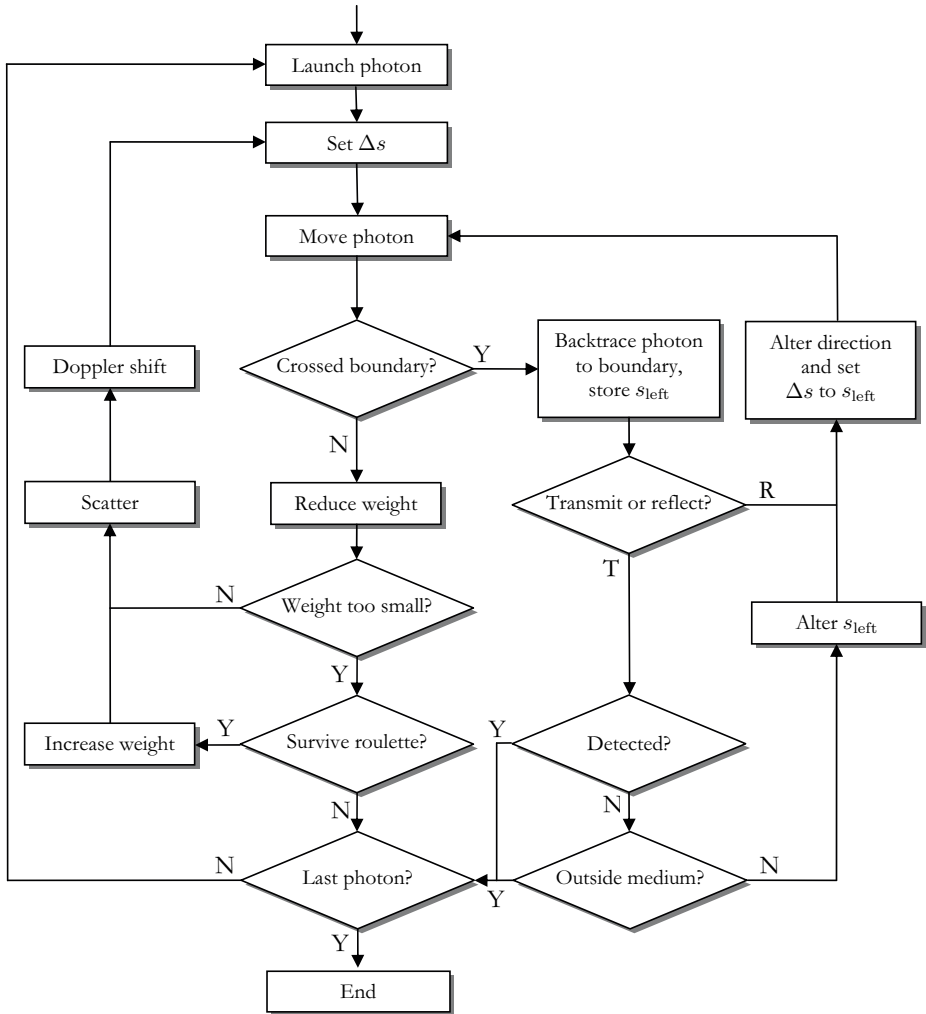
Figure 4.1 Flowchart of the Monte Carlo method.

Before escaping the light source, the direction is refracted at the border between the light source and the medium, if the refractive index is not matched (see subsection 4.1.10). Some photons may also be internally reflected and thus never reach the medium.

4.1.2   Set Δs

Beer-Lamberts law (Equation 3.1) can be used to express the cumulative distribution $F(s)$ that the photon step size Δs before next scattering or absorption event is less than s:

$$F(s) = 1 - e^{-\mu_\mathrm{t} s}, \tag{4.1}$$

The step size is therefore randomly chosen as:

$$\Delta s = \frac{-\ln \xi}{\mu_\mathrm{t}}. \tag{4.2}$$

In early Monte Carlo software, the step size was often fixed to the mean free path length, which could introduce large errors.

4.1.3 Move photon

When moving a photon, its new position is simply calculated by:

$$\begin{cases} x' = x + \mu_x \Delta s \\ y' = y + \mu_y \Delta s \\ z' = z + \mu_z \Delta s \end{cases} . \tag{4.3}$$

4.1.4 Crossed boundary?

The medium may consist of any number of objects of any arbitrary geometrical shape. It is convenient to let the objects overlap in space and then it must be explicitly defined which object dominates over the other. The boundary between two overlapping objects will equal the boundary of the dominating object. A typical situation is when a blood vessel is located within a semi-infinite slab, where the blood vessel then dominates the slab. For example in Figure 4.2, the light object dominates the dark object, and therefore the boundary between the objects is the solid line rather than the dashed line. When checking if the photon has crossed any boundary, it must therefore first be checked if the photon has crossed the boundary of any object that dominates the current object, as in case a in the figure, and thereafter if it has crossed the boundary of the current object, as in case b. In case c, the photon remains in the same object and has not actually crossed any boundary. It should be noted, however, that testing that the photon remains within the same object is not enough to conclude that it has not crossed any boundary, as in case d.
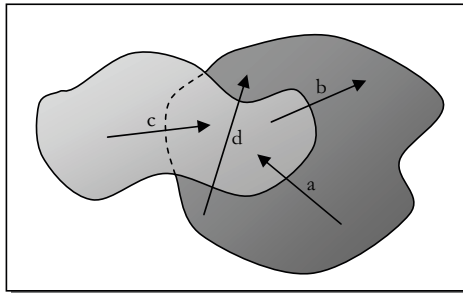
Figure 4.2 Illustration of the boundary and boundary crossings between overlapping objects.

It is trivial to check if the photon has crossed a boundary of a semi-infinite slab, finite in z-direction and infinite in x- and y-directions. For other mathematically easily defined objects, such as boxes, spheres, and cylinders, the task is solved by using simple geometrical rules, but for general irregular shaped objects, other strategies must be employed. For objects that are not aligned to the x-, y-, and z-axes, the coordinate system may temporarily be rotated so that the object is aligned to the axes before calculating the boundary.

4.1.5 Reduce weight

When no boundary is crossed, the next step is to reduce the weight of the photon (see also Section 4.2.2) due to absorption. The weight is reduced according to

$$w' = w \frac{\mu_s}{\mu_t}, \tag{4.4}$$

where the term μ_a/μ_t is often called the albedo of the object. This way of reducing the weight is correct when calculating the step size as described in subsection 4.1.2. An alternative way, which may be more intuitive, is to calculate the step size as

$$\Delta s = \frac{-\ln \xi}{\mu_s}, \tag{4.5}$$

i.e. ignoring μ_a, and then reduce the weight according to Beer-Lamberts law as

$$w' = we^{-\mu_a \Delta s}. \tag{4.6}$$

These two strategies generate identical simulation results, but as the second alternative is somewhat slower due to the exponential term in 4.6, the first strategy may be preferable.

4.1.6   Roulette

It is very inefficient to track photons with small weights until they are detected or escape from the medium. To prevent this, a technique called Russian roulette is used. When the weight drops below a certain threshold value, typically between 1/1000 and 1/10, the photon has one chance out of r to survive, typically between 10 and 100. If it survives, its weight is increased with the factor r, and it continues its random walk. The weight increase is crucial for energy conservation.

In a few cases, it is not efficient to use weights at all. Then it is just decided if the photon shall continue its random walk or not. If $\xi < \mu_a/\mu_t$, the photon is terminated, or else the photon continues its random walk with intact weight, i.e. without the weight loss in Equation 4.4.

4.1.7   Scatter

In early Monte Carlo software, the scattering was totally isotropic, i.e. all scattering angles had equal probability. However, biological tissue is generally strongly forward scattering, i.e. $g = \langle \cos \theta \rangle$ is rather close to unity, usually between 0.7-0.9 and even higher for blood. For correct results it is important that a sufficient exact phase function is used. This is more important when studying photons close to the source. At large distances, more than some $1/\mu_s'$, it is sufficient to have the correct μ_s' and isotropic scattering will do; at medium distances, μ_s' has to be divided into μ_s and g for correct results; and at very short distances, less than about $1/\mu_s$, higher order moments of the scattering phase functions must be known as well [87]. How to include the phase function in the Monte Carlo software was first described by Prahl. [85]

Most often the azimuthal angle ϕ is randomly chosen from a uniform distribution between 0 and 2π:

$$\theta = 2\pi\xi. \tag{4.7}$$

The longitudinal angle θ is instead randomly chosen from the scattering phase function (see Figure 4.3 for an illustration of azimuthal angle ϕ and longitudinal angle θ). Any phase function can be used by employing a table lookup procedure, but most often the Henyey-Greenstein phase function is used in bio-optical Monte Carlo, where $\cos \theta$ can be given by an analytic expression [85], which is advantageous both for speed and accuracy:

$$\cos \theta = \left((1 + g_{HG}^2) - \left(\frac{1 - g_{HG}^2}{1 - g_{HG} + 2g_{HG}\xi} \right)^2 \right) \Big/ 2g_{HG}. \tag{4.8}$$

An analytic expression also exists for the Gegenbauer kernel phase function [88]:

$$\cos \theta = \frac{1}{2g_{Gk}} \left(1 + g_{Gk}^2 - \left(\frac{\xi}{A} + (1 + g_{Gk})^{-2\alpha_{Gk}} \right)^{-1/\alpha_{Gk}} \right), \tag{4.9}$$

where

$$A = \frac{(1 - g_{\mathrm{Gk}}^2)^{2\alpha_{\mathrm{Gk}}}}{(1 + g_{\mathrm{Gk}})^{2\alpha_{\mathrm{Gk}}} - (1 - g_{\mathrm{Gk}})^{2\alpha_{\mathrm{Gk}}}}. \tag{4.10}$$

When both ϕ and θ are given, the new direction is calculated by:

$$\begin{cases} \mu_x' = \frac{\sin\theta}{\sqrt{1-\mu_z^2}}(\mu_x\mu_z\cos\phi - \mu_y\sin\phi) + \mu_x\cos\theta \\ \mu_y' = \frac{\sin\theta}{\sqrt{1-\mu_z^2}}(\mu_y\mu_z\cos\phi - \mu_x\sin\phi) + \mu_y\cos\theta \\ \mu_z' = -\sin\theta\cos\phi\sqrt{1-\mu_z^2} + \mu_z\cos\theta \end{cases}. \tag{4.11}$$

If the z-direction is very close to the normal, (e.g. when $|\mu_z| > 0.99999$), the following formulas are used instead to avoid numerical problems:

$$\begin{cases} \mu_x' = \sin\theta\cos\phi \\ \mu_y' = \sin\theta\sin\phi \\ \mu_z' = \mathrm{sign}\mu_z\cos\theta \end{cases}, \tag{4.12}$$

where sign denotes the signum function.

It is normally assumed that the tissue is isotropic, i.e. that the scattering and absorption properties in a certain point are independent of the photon direction $\boldsymbol{\mu}$. This is however not true for all types of tissue, it can for example be questioned in skeletal muscle tissue. It is possible to account for this anisotropic behavior in the Monte Carlo simulation, which was demonstrated by Kienle and Hibst for human dentin. [89]
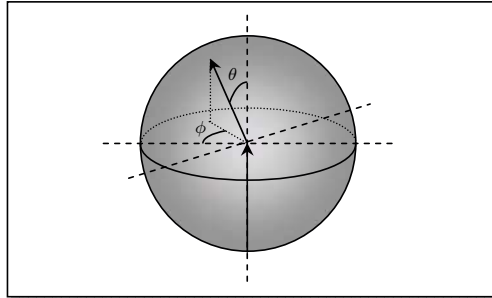
Figure 4.3 Illustration of scattering with azimuthal angle ϕ and longitudinal angle θ.

4.1.8   Doppler shift

If the scattering event is invoked by a moving particle, the photon is Doppler shifted by an amount of:

$$f_{\mathrm{D}} = -\mathbf{v} \cdot \mathbf{q}, \tag{4.13}$$

where $\mathbf{v}$ is the velocity vector of the moving particle, $\cdot$ denotes the scalar product, and the scattering vector $\mathbf{q}$ is the difference between the wave vectors $\mathbf{k}_{\mathrm{i}}$ and $\mathbf{k}_{\mathrm{s}}$, calculated by:

$$\mathbf{q} = \mathbf{k}_{\mathrm{i}} - \mathbf{k}_{\mathrm{s}} = \frac{n}{\lambda}(\boldsymbol{\mu} - \boldsymbol{\mu}'), \tag{4.14}$$

where n is the refractive index of the medium, λ is the laser wavelength, $\boldsymbol{\mu}$ is the direction unit vector of the incoming photon, and $\boldsymbol{\mu}'$ is the direction unit vector of the scattered photon. The total Doppler shift of a photon, i.e. the sum of individual f_{D}, is simply an extra scalar attribute of the photon. For details on single Doppler shifts, see Section 5.1.

4.1.9   Backtrace photon…

When the current photon step caused the photon to cross a boundary, the photon is backtraced to the point where it crossed the boundary, and the distance backtraced is stored as s_{left}.

4.1.10 Transmit or reflect?

When the photon is backtraced to the border, it is decided whether to transmit or reflect the photon. This is done by the Fresnel formula given in Equation 3.3:

$$r(\theta_{\text{i}}) = \frac{1}{2} \left(\frac{\sin^2(\theta_{\text{i}} - \theta_{\text{t}})}{\sin^2(\theta_{\text{i}} + \theta_{\text{t}})} + \frac{\tan^2(\theta_{\text{i}} - \theta_{\text{t}})}{\tan^2(\theta_{\text{i}} + \theta_{\text{t}})} \right) \tag{4.15}$$

where θ_{i} is the incident angle to the normal and the transmittance angle θ_{t} is given by Snell's law 3.2:

$$n_{\text{i}} \sin \theta_{\text{i}} = n_{\text{t}} \sin \theta_{\text{t}}. \tag{4.16}$$

When $r(\theta_{\text{i}}) < \xi$, the photon is transmitted to the other object, and otherwise it is internally reflected. It should be noted that 4.15 reduces into:

$$r(0) = \left(\frac{n_{\text{i}} - n_{\text{t}}}{n_{\text{i}} + n_{\text{t}}} \right)^2 \tag{4.17}$$

for an incident angle orthogonal to the border.

4.1.11 Detected?

Detectors are treated as normal objects, with the only difference that photons are detected when transmitted into them. When a photon is detected, its random walk is terminated and information about the photon is stored. Normally, at least the position of detection and the photon weight is stored, but other information, such as the final direction of the photon, Doppler shift information, path length etc. can be stored. In principle, every single step and intermediate state of the photon in the random walk can be stored. This offers great advantages compared to for example the diffusion approximation, for understanding the details of the light transport.

4.1.12 Outside medium?

The photon is simply terminated when it escapes the defined geometrical perimeter of the model.

4.1.13 Alter s_{left}

When the photon is transmitted into an object, the variable s_{left} is updated to account for the difference in μ_{t} between the two objects. This is done by multiplying s_{left} with the quotient of μ_{t} between the incoming and transmission objects.

4.1.14 Alter direction…

When the photon is internally reflected, its direction is altered according to:

$$\begin{cases} \mu'_x = \text{-}2\mathbf{n} \cdot \boldsymbol{\mu} + \mu_x \\ \mu'_y = \text{-}2\mathbf{n} \cdot \boldsymbol{\mu} + \mu_y \\ \mu'_z = \text{-}2\mathbf{n} \cdot \boldsymbol{\mu} + \mu_z \end{cases}, \tag{4.18}$$

where $\mathbf{n} = [n_x, n_y, n_z]^T$ is the normal unit vector to the boundary and $\boldsymbol{\mu}$ is the direction unit vector of the photon.

Transmitted photons are refracted and the new direction is calculated by:

$$\begin{cases} \mu'_x = \kappa n_x + \mu_x n_\mathrm{i}/n_\mathrm{t} \\ \mu'_y = \kappa n_y + \mu_y n_\mathrm{i}/n_\mathrm{t} \\ \mu'_z = \kappa n_z + \mu_z n_\mathrm{i}/n_\mathrm{t} \end{cases}, \qquad (4.19)$$

where κ is given by:

$$\kappa = \sqrt{1 - n_\mathrm{i}^2/n_\mathrm{t}^2(1 - \cos^2\theta_\mathrm{i}) - n_\mathrm{i}/n_\mathrm{t}\cos\theta_\mathrm{i}}, \qquad (4.20)$$

where θ_i is the incident angle relative to the normal.

The new step size Δs is then set to s_left.

4.1.15 Last photon?

The simulation is preferably terminated when a certain amount of photons are simulated or detected. When it is possible to calculate the variance of the result continuously and efficiently, it may be convenient to terminate the simulation when a sufficiently low variance has been reached.

4.1.16 End

When the simulation is terminated, the number of emitted photons is stored, as well as the simulation time and other relevant information.

4.2   Variance reduction and post processing

Because a large amount of photons has to be simulated to achieve correct results, the Monte Carlo method is slow and computationally demanding. Although super computers with thousands of parallel CPU:s, as well as utilizing the GPU of modern computers, reduces the time needed significantly, it may be even more efficient to use various variance reducing methods and post processing techniques. Some examples of such methods, most of them used in this thesis, are presented in this section.

4.2.1   Russian roulette

The concept of Russian roulette already has been introduced in Section 4.1.6 where it was used to terminate most photons which dropped below a certain weight due to absorption. The technique can be used in other situations as well though, for example when the photon propagates far away from the source and detector. Russian roulette is also important in for example forced detection.

4.2.2   Weights

In Monte Carlo simulations, it is often convenient to allow photons to have any weight between zero and unity, and theoretically any other weight as well, indicating their contribution to the result. This weight has nothing to do with the wavelength dependent energy of the photon or with the mass of the photon. In Section 4.1.5 it was described how the effect of absorption was accounted for using weights. Although this is the most common way to use it, weights are a central concept in Monte Carlo simulations and are frequently used for other purposes as well. Consider for example a model where the detector has a sensitivity that varies with the detection angle. Instead of rejecting some of the photons detected at a certain angle, all photons that reach the detector are detected and reweighted dependent on their detection angle. By storing the detection angle, the angle sensitivity can also be added or changed afterwards.

Weights play a central role in most types of variance reducing methods, such as photon splitting, forced detection, and various types of post processing methods.

4.2.3 Photon splitting

It is sometimes very efficient to split some photons during their random walk in the simulated medium. When splitting a photon, the weight of the original photon is divided on the split photons for energy conservation, and then all split photons follow their own random walk from the point of splitting. [90] This is efficient for example for large source-detector separations, when splitting photons approaching the detector increase the probability that some of the split photons will actually reach the detector. This technique was also used in many of the simulations in this thesis for photons that gathered a high total Doppler shift. Since relatively few photons accumulate a high total Doppler shift, it is important that these photons reach the detector to reduce the statistical uncertainties in the Doppler power spectrum at high frequencies.

4.2.4 Controlled Monte Carlo

In some situations only photons of a certain property are interesting, or at least much more interesting than other photons. Such situations are for example LDF, where Doppler shifted photons may be more interesting than non-Doppler shifted, or time resolved optical tomography, where only early arriving photons are of interest. To increase the speed of such simulations, it is important to make sure that the computational time is mostly spent on calculating the random walk of these interesting photons and to skip other photons. One way to do that is to use photon splitting as described in the previous subsection, but a method that is even more efficient in time resolved optical tomography is to force the photons to go in a ballistic path. That is done by changing the scattering phase function in each scattering event so that it peaks towards the detector, and for energy conserving reasons the weight of the photon is reduced at each scattering event based on the scattering angle probability change (see also subsection 4.2.7 and Equation 4.22). This technique is called controlled Monte Carlo [91] or biased Monte Carlo [92].

4.2.5 Forced detection

When the probability for a photon to hit the detector from any scattering position is very low, but not zero, a variation reducing technique called forced detection is very effective. This technique calculates the low probability that the photon will go directly to the detector in the next step without further scattering, and forces a part of the photon with a weight proportional to that probability to be detected. This is done at every scattering event. This is a common technique in Monte Carlo simulations within the fields of atmospheric optics, nuclear and particle physics, and radiology [93-95], but is rarely used in biomedical optics [96,97]. More details on this technique can be found in [III] which describes forced detection for biomedical optics.

4.2.6 Model symmetry

The variance reducing methods presented so far are designed to reduce the simulation time of a single simulation. However, by recalculating some stored parameters, much can be done when analyzing the simulation. These post processing techniques can be divided into two separate groups, one taking advantage of model symmetries (treated in this subsection), and one that recalculates the results for other optical properties (treated in the next subsection).

In many situations, the simulated geometry has some sort of symmetry, for example the typical model consisting of semi-infinite layers. By taking advantage of this symmetry when analyzing the simulation, the simulation time can be reduced significantly. One example of such a technique is to convolute an infinitely narrow beam to a wider finite beam.[98] The rationale behind this can be realized by inspecting Figure 4.4a. Consider a photon path that begins in the center of the emitting fiber and ends just outside the receiving fiber. By copying and moving the photon path so that it originates from various locations inside the

emitting fiber, some of these paths will end within the receiving fiber. In this way, more of the simulated photon paths are taken into the result and fewer total paths have to be simulated.

When the detector is a circular fiber tip, the axial symmetry around the light source can also be used.[34] This is shown in Figure 4.4b, where the detection position of a photon detected at distance r from the center of the emitting fiber is rotated so that it is detected within a detector fiber. For energy conservation the photon then also has to reduce its weight w with the fraction $\mathrm{d}C/(2\pi r)$, which is done with the following expression:

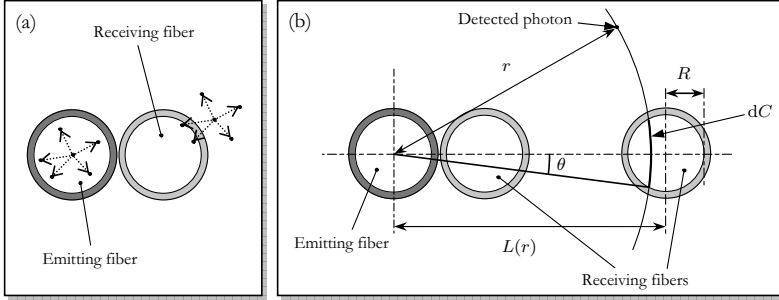$$w' = w\frac{1}{\pi}\arccos\left(\frac{r^2 + L^2(r) - R^2(r)}{2rL(r)}\right). \tag{4.21}$$

Figure 4.4 Principles of source convolution (a) and detection rotation (b).

4.2.7 White Monte Carlo

Especially when simulating homogeneous media, it is possible to recalculate the simulated results in a post processing procedure for other optical properties than those that were used in the original simulation.[76,99-102] This is sometimes called white Monte Carlo since the color of the original "white" simulation can be changed by adding or adjusting the optical properties afterwards.

Adding the absorption is trivial when storing the path length d of each individual photon. The absorption is then added by applying Beer-Lamberts law on each photon. By storing the path length of the photons in each object this procedure can easily be applied to any arbitrary complex model and not only homogeneous models. For efficiency, it can be wise to divide the photons into groups according to their path length, and then apply Beer-Lamberts law for each group instead of recalculating each individual photon. How this can be done in a multilayered medium is described in [V].

In a one-layered medium where the photons are injected in an infinitely narrow beam, the effect of a changed scattering coefficient can also be added afterwards. Since each step of the photon scales linearly to $1/\mu_s$ (see Equation 4.5), the distance of the detected position from the injection point will also scale linearly to $1/\mu_s$. Thus, rescaling a simulation where the scattering coefficient was $\mu_{s,orig}$, to a simulation with $\mu_{s,new}$, all detection positions can be scaled with $\mu_{s,orig}/\mu_{s,new}$. When adding both μ_a and μ_s, the scaling of the path length d with $\mu_{s,orig}/\mu_{s,new}$ must also be considered when adding μ_a. This is summarized in Figure 4.5.

It is also possible to change the scattering phase function in a post processing procedure when storing the scattering angle θ for each scattering event. This is done by reweighting the photon at each scattering event according to the relation of the scattering phase function used in the simulation, $p_s(\cos\theta)$, and the wanted phase function, $p_s'(\cos\theta)$, for the current scattering angle θ, by: [103]

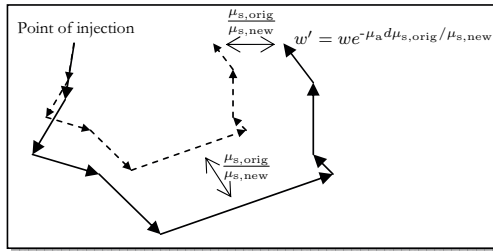$$w' = w\frac{p_s'(\cos\theta)}{p_s(\cos\theta)}. \tag{4.22}$$

Figure 4.5 Rescaling of detection position and photon weight
when adding μ_a and $\mu_{s,new}$ in a post processing process.

This technique can be generalized to reweight the photons also for other μ_a and μ_s, and, in theory, results for any arbitrary refractive index matched geometry can thus be calculated using this post processing technique when the position of each scattering event is also stored. However, the reweighting will generally result in large amounts of statistical uncertainties in the result for highly scattering media when the difference between for example $p_s(\cos\theta)$ and $p'_s(\cos\theta)$ is large. The technique also requires a large amount of storage since information about each scattering event is needed and it is therefore slower than rescaling with μ_a and μ_s as demonstrated in Figure 4.5.

4.3   Software description and validation

A Monte Carlo software following the principles described in Section 4.1 has been developed during the work presented in this thesis. Being able to customize the output parameters from this software has been of invaluable importance for the methods developed, and also for understanding the complex light-tissue interaction involved in LDF. A screen dump of the software user interface can be seen in Figure 4.6.
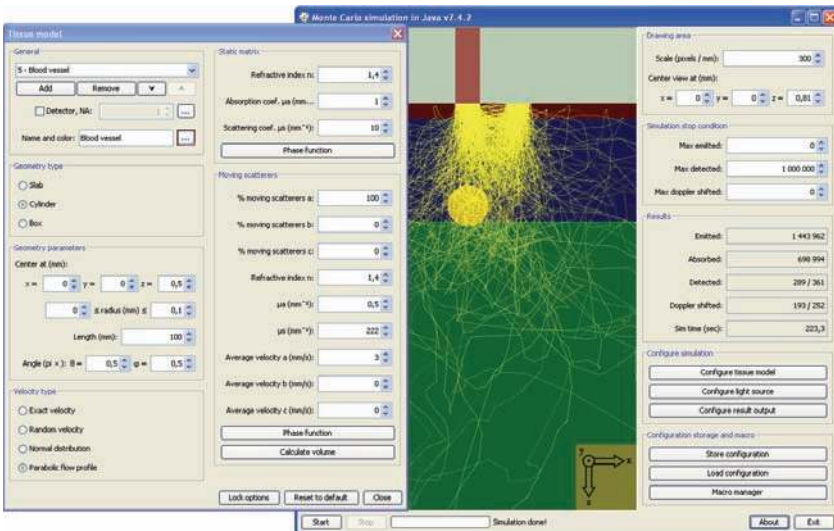

Figure 4.6 Screen dump from the Monte Carlo software developed and used during the thesis work.

Since Monte Carlo simulations are central to this thesis, it is of the uttermost importance that they produce correct results. Therefore, the output from this software has been compared with the results presented by Wang and Jacques [86] produced by their MCML software, which has been validated both with other Monte Carlo software and with other analytical and numerical calculations [85,104,105]. The first comparison is between a model consisting of one 0.2 mm thick slab with $\mu_a = 1.0$ mm^{-1}, $\mu_s = 9.0$ mm^{-1}, $g = 0.75$ (Henyey-Greenstein phase function), and $n = 1$. Ten simulations were run, all with 50 000 emitted photons. This resulted in $9.735 \pm 0.033\%$ reflected photons and $66.112 \pm 0.052\%$ transmitted photons for the thesis software, compared to $9.734 \pm 0.035\%$ and $66.096 \pm 0.020\%$, respectively, for MCML (average $\pm$ standard error).

The second comparison is with a refractive index mismatched infinitely thick medium with $\mu_a = 1.0$ mm^{-1}, $\mu_s = 9.0$ mm^{-1}, $g = 0$, and $n = 1.5$. Here, ten simulations of 5 000 photons each were run. For the thesis software, the total reflectance (including the specularly reflected photons) was $26.114 \pm 0.158\%$, compared with $25.907 \pm 0.170\%$ for MCML.

The angularly resolved diffuse reflectance and transmittance were compared next. The simulated medium was the same as in the first comparison. 500 000 photons were emitted and 30 angular grid elements between 0 and $\pi/2$ were used in the analysis. The results for reflectance and transmittance (non-scattered photons are excluded) are shown in Figure 4.7.
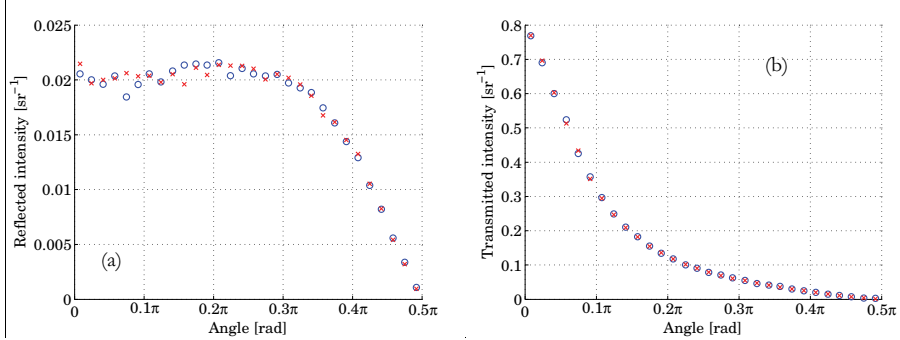
Figure 4.7 Angularly resolved reflected (a) and transmitted (b) intensity. Crosses – MCML, dots – thesis software.

Finally, the radially resolved diffuse reflectance and transmittance from a multilayered model was compared. The parameters of the model, which is surrounded by air with $n = 1.0$, is described in Table 4.1. In this simulation, 1 000 000 photons were emitted perpendicular to the surface of the model at radius 0. The results (50 bins between 0 and 5 mm) are compared in Figure 4.8.

Table 4.1 The optical properties and thickness t of the three-layered model

| Layer	n [-]	μ_a [mm^{-1}]	μ_s [mm^{-1}]	g [-]	t [mm]
1	1.37	0.1	10	0.9	1.0
2	1.37	0.1	1.0	0.0	1.0
3	1.37	0.2	1.0	0.7	2.0

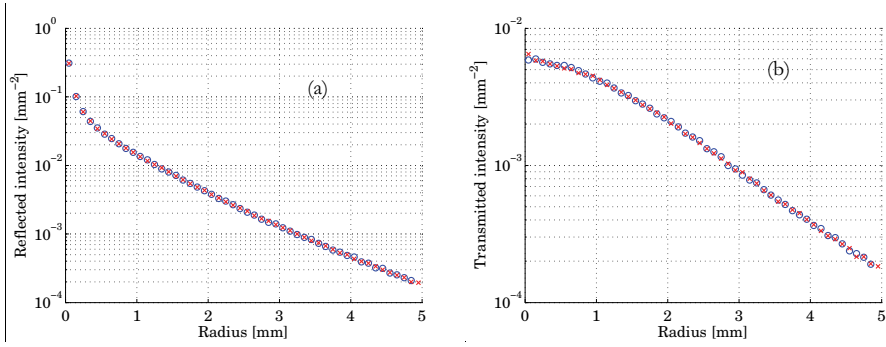Figure 4.8 Radially resolved reflected (a) and transmitted (b) intensity. Crosses – MCML, dots – thesis software.

The small differences between the results from the thesis software and MCML are explained by statistical uncertainties due to the limited amount of photons used. Based on these validation simulations, it is reasonable to believe that the developed Monte Carlo software produces correct results.

5   Laser Doppler flowmetry

The laser, developed in the middle of the last century, soon found its way into medicine, where it has been frequently used both in therapy and diagnostics. The word laser is an acronym for Light Amplification by Stimulated Emission of Radiation. Two characteristics of the light radiated by this stimulated emission are that it is monochromatic and coherent. The coherency is central in Laser Doppler Flowmetry (LDF), as explained later in this chapter.

In LDF, light that has been backscattered from tissue is analyzed to retrieve information about the blood flow in the microcirculation. A fraction of the backscattered light has been scattered by moving red blood cells and undergone one or several Doppler shifts (see Section 5.1). The backscattered light interferes on the detector which causes the detector current to fluctuate depending on the Doppler shifts of the backscattered light (see Section 5.2). The detector current is analyzed to give information about the local microcirculation, conventionally summarized into a single perfusion value that scales to the tissue fraction and velocity of the moving red blood cells in the examined tissue volume (see Section 5.3). Both single point (laser Doppler perfusion monitoring, LDPM) and imaging (laser Doppler perfusion imaging, LDPI) systems exist, and the hardware realizations of these systems are described in Section 5.4. At the end of this chapter, in Section 5.5, the relation between LDF and Monte Carlo simulations is described and discussed.

5.1   Single Doppler shift

The Doppler effect, i.e. the frequency shift of e.g. sound or light when emitted, reflected, scattered, or detected by a moving object, was first described by Johan Christian Doppler in 1842 [106]. The size f_D of this frequency shift in the case of light scattered by a moving object, for example an RBC, is given by the following expression:

$$f_D = \text{-}\mathbf{v} \cdot \mathbf{q} = \text{-}2\frac{v}{\lambda}\sin\frac{\theta}{2}\cos\varphi, \tag{5.1}$$

where $\mathbf{v}$ is the velocity vector of the moving object in the plane of scattering, the scattering vector $\mathbf{q}$ is the difference between the wave vectors $\mathbf{k}_i$ and $\mathbf{k}_s$ ($|\mathbf{k}| = 1/\lambda$) of the incident and scattered light wave, respectively, λ is the wavelength, θ is the scattering angle, and φ is the angle between $\mathbf{q}$ and $\mathbf{v}$ (see also Figure 5.1a). This expression follows from Equations 5.2 to 5.7 given below. The major steps in this section have previously been presented in Reference [107].

The light wave incident to the particle has a frequency f_i and a wavelength $\lambda_i = 1/k_i = c/f_i$, where $c = c_0/n$ is the speed of light in the tissue with refractive index n. Now consider the time Δt for a certain position of the incident wave to travel the distance from λ_i away from the particle, to the particle. Since the particle moves a small distance during this time, the traveled distance will not be exactly λ_i, but rather:

$$\lambda_i + \Delta t v \cos\psi = \Delta t c, \tag{5.2}$$

where ψ is the angle between $\mathbf{k}_i$ and $\mathbf{v}$ (Figure 5.1b). During the same time, the light wave that is scattered with the angle θ has propagated one wavelength λ_s away relative to the particle, which can also be expressed as (Figure 5.1c):

$$\lambda_s = c\Delta t - \Delta t v \cos(\psi + \theta). \tag{5.3}$$

Combining Equations 5.2 and 5.3 gives:

$$\lambda_s = \frac{\lambda_i - \lambda_i \frac{v}{c}\cos(\psi + \theta)}{1 - \frac{v}{c}\cos\psi}.$$

(5.4)

The frequency shift f_D is the difference between the frequency of the incident and scattered light waves, i.e. $f_i = c/\lambda_i$ and $f_s = c/\lambda_s$, respectively:

$$
\begin{aligned}
f_D &= f_i - f_s \\
&= c\left(\frac{1}{\lambda_i} - \frac{1}{\lambda_s}\right) \\
&= \frac{c}{\lambda_i}\left(\frac{1 - \frac{v}{c}\cos\psi}{1 - \frac{v}{c}\cos(\psi + \theta)} - 1\right) \\
&= \frac{c}{\lambda_i}\left(\frac{1 - \frac{v}{c}\cos\psi - 1 + \frac{v}{c}\cos(\psi + \theta)}{1 - \frac{v}{c}\cos(\psi + \theta)}\right) \\
&\cong \frac{v}{\lambda_i}(\cos(\psi + \theta) - \cos\psi),
\end{aligned}
$$

(5.5)

where the nominator is removed in the last step since $v \ll c$. This observation also leads to $\lambda_i \cong \lambda_s$ and consequently $k_i \cong k_s$. Thus, the incoming and scattered wave vectors, $\mathbf{k}_i$ and $\mathbf{k}_s$, form an isosceles triangle together with the scattering vector $\mathbf{q}$, with the angles θ and $(\pi - \theta)/2$ (Figure 5.1d). The angle ψ can thus be calculated:

$$\theta + \psi + \varphi + \frac{\pi - \theta}{2} = \pi \quad \Rightarrow \quad \psi = \frac{\pi}{2} - \frac{\theta}{2} - \varphi.$$

(5.6)

Combining Equations 5.5 and 5.6 results in:

$$
\begin{aligned}
f_D &\cong \frac{v}{\lambda_i}\left[\cos\left(\frac{\pi}{2} - \frac{\theta}{2} - \varphi + \theta\right) - \cos\left(\frac{\pi}{2} - \frac{\theta}{2} - \varphi\right)\right] \\
&= \frac{v}{\lambda_i}\left[\sin\left(-\frac{\theta}{2} + \varphi\right) - \sin\left(\frac{\theta}{2} + \varphi\right)\right] \\
&= -2\frac{v}{\lambda_i}\sin\frac{\theta}{2}\cos\varphi \\
&= -\mathbf{q}\cdot\mathbf{v}.
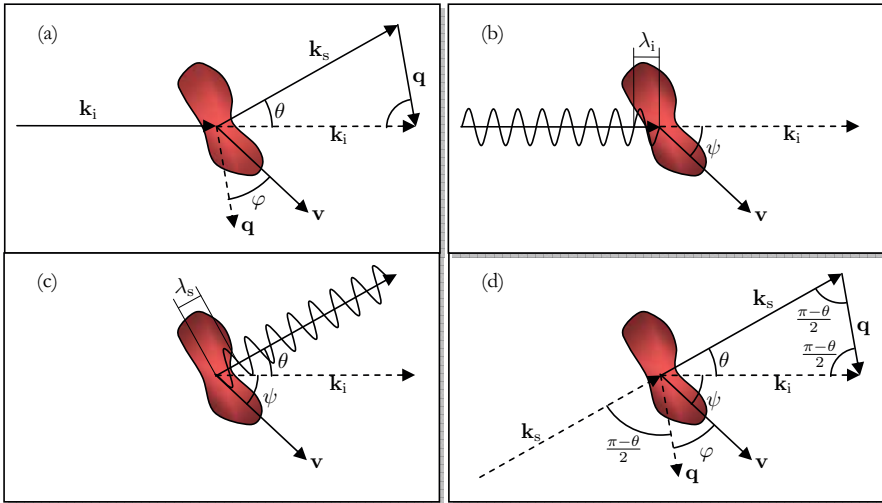\end{aligned}
$$

(5.7)

Figure 5.1 Illustrations showing the vectors and angles involved when calculating the size of a single Doppler shift.

When analyzing this expression it is evident that the size of the Doppler shift is linearly dependent on v. It is maximized when $\theta = -\pi$, i.e. backscattering, and when the directions of the moving particle and the incident light are equal or opposite. However, RBC:s are very forward scattering ($g \approx 0.991$ [II]), i.e. θ is most often close to 0. That results in that the scattering vector $\mathbf{q}$ is most often orthogonal to the direction of the light, and the size of the Doppler shift will therefore be maximized when the direction of the RBC is orthogonal to the direction of the light.

5.2   The Doppler power spectrum

All light, non Doppler shifted, single shifted, and multiple shifted, that impinges the detector will interfere (under the assumption of equal polarization direction). When the light is coherent, the interference gives rise to a speckle pattern and due to the small frequency differences within the light, caused by the Doppler shifts, this speckle pattern will move and change intensity rhythmically – it seams to beat. This beating leads to amplitude variations in the detector current which can be analyzed by looking at the power spectral density of the signal, called the Doppler power spectrum, $P_D(f)$, throughout this thesis. This section, which is based on the theoretical work by Forrester [2] and Cummins and Swinney [3], extended by Larsson [108], shows the relationship between individual Doppler shifts and the Doppler power spectrum. Parts of this section has previously been presented in Reference [107].

Consider light on the tip of an optical fiber or on a small spot on a tissue surface, being backscattered from the tissue and originating from a laser source. Some of this light has retained its laser frequency, while some has undergone small frequency changes due to Doppler shifts. The phase of the light can be assumed to be random due to the various optical path lengths in the medium, and the fact that the differences in optical path length are generally much larger than the wavelength of the light. For simplicity, consider this light as being E-field sources on the fiber tip or tissue surface, with the frequency and phase as given above, emitting E-fields in all directions. At the surface of a detector positioned some distance away from these E-field sources, a beating speckle pattern will form from the superposition of all E-fields. A 10 ms sequence of a simulated such speckle pattern is shown in Figure 5.2. The simulation was based on 10,000 E-fields with frequencies $\beta = \beta_L \pm 2.5$ kHz, where $\beta_L \approx 3.8 \times 10^{14}$ Hz (a 780 nm laser), and random phase. The E-fields were distributed on a 0.125 diameter fiber tip and moved with a velocity up to 2.5 mm/s. The speckle pattern formed on a 1×1 mm detector surface placed 5 cm away from the fiber tip is shown.

The theoretical derivation of the Doppler power spectrum starts at the light that impinges the detector. This light has a frequency content described by the optical Doppler spectrum $G(\beta)$, created from the individual Doppler shifts, normalized so that:

$$\int_0^\infty G_c(\beta)\, \mathrm{d}\beta = i_{\mathrm{dc,c}}, \tag{5.8}$$

where $i_{\mathrm{dc,c}}$ is the average current generated by the detector, under the assumption that the light is spatially coherent over the detector. Dividing the optical Doppler spectrum into frequency intervals, the E-field of the light on the detector in the m:th interval can be expressed as a function of time t as:

$$E_m(t) = \sqrt{G_m \Delta \beta}\, e^{j(2\pi \Delta \beta m t + \phi_m)}, \tag{5.9}$$

where $G_m \Delta \beta = G_c(\beta_m) \Delta \beta$ is the intensity of the m:th frequency interval and ϕ_m is a random phase. The generated detector current can be expressed by summing over all frequencies:
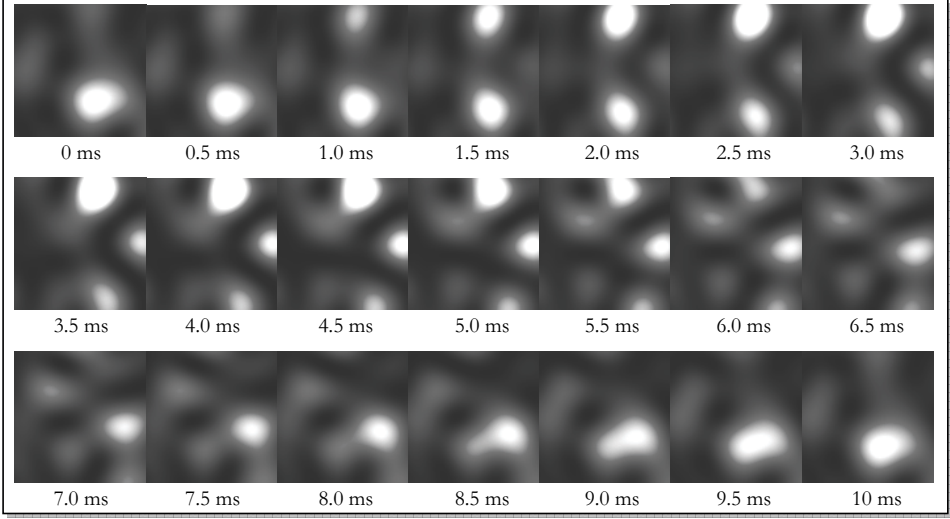
Figure 5.2 A 10 ms sequence of a simulated speckle pattern on a 1×1 mm detector surface placed 5 cm away from a 0.125 mm diameter fiber tip.

$$i_c(t) = E(t)E(t)^*$$

$$= \Delta\beta \sum_{m=0}^{\infty} \left(\sqrt{G_m}e^{j(2\pi\Delta\beta mt+\phi_m)} \right) \sum_{m=0}^{\infty} \left(\sqrt{G_m}e^{-j(2\pi\Delta\beta mt+\phi_m)} \right)$$

$$= \Delta\beta \sum_{m=0}^{\infty}\sum_{n=0}^{\infty} \left(\sqrt{G_mG_n}e^{j(2\pi(m-n)\Delta\beta t+(\phi_m-\phi_n))} \right). \tag{5.10}$$

A double sum over n and m can be rewritten as $\sum_{m,n} = \sum_{m<n} + \sum_{m=n} + \sum_{m>n}$. Applying this to Equation 5.10 and reverse n and m in the third term gives us:

$$i_c(t) = \Delta\beta \left[\sum_{m=0}^{\infty}G_m + \sum_{m=0}^{\infty}\sum_{n=m+1}^{\infty} \left(\sqrt{G_mG_n}\left(e^{j(2\pi(m-n)\Delta\beta t+(\phi_m-\phi_n))} + e^{-j(2\pi(m-n)\Delta\beta t+(\phi_m-\phi_n))} \right) \right) \right]$$

$$= \underbrace{\Delta\beta \sum_{m=0}^{\infty}G_m}_{i_{dc,c}} + \underbrace{2\Delta\beta \sum_{m=0}^{\infty}\sum_{n=m+1}^{\infty} \left(\sqrt{G_mG_n}\cos(2\pi(m-n)\Delta\beta t+(\phi_m-\phi_n)) \right)}_{i_{ac,c}}. \tag{5.11}$$

By letting $\Delta\beta \to 0$ and changing the sum to an integral, the first term in the resulting expression is identified as $i_{dc,c}$ (Equation 5.8). The second term varies over time and is denoted $i_{ac,c}$. By introducing $b = n - m$ and $\psi_{m,b} = \phi_{m+b} - \phi_m$, $i_{ac,c}$ can be written as

$$i_{ac,c}(t) = 2\Delta\beta \sum_{m=0}^{\infty}\sum_{b=1}^{\infty} \left(\sqrt{G_mG_{m+b}}\cos(2\pi b\Delta\beta t+\psi_{m,b}) \right). \tag{5.12}$$

Now, let $i_{ac,c}$ be a function of $b\Delta\beta$ and t, i.e. dropping the sum over b in Equation 5.12:

$$i_{ac,c}(b\Delta\beta,t) = 2\Delta\beta \sum_{m=0}^{\infty} \left(\sqrt{G_mG_{m+b}}\cos(2\pi b\Delta\beta t+\psi_{m,b}) \right). \tag{5.13}$$

Before continuing, $f = b\Delta\beta$ is also introduced (note that $n > m$ which leads to $b > 0$ and $f > 0$, and that generally $f \ll \beta$). The power spectral density of the time varying part of the detector current, $P_{D,c}(f)$, is calculated from $i_{ac,c}(f,t) = i_{ac,c}(b\Delta\beta,t)$ as:

$$P_{\mathrm{D,c}}(f) = \frac{\langle i_{\mathrm{ac}}(f,t)^2 \rangle}{\Delta\beta}$$

$$= 4\Delta\beta \left\langle \left[\sum_{m=0}^{\infty} \left(\sqrt{G_m G_{m+b}} \cos(2\pi f t + \psi_{m,b}) \right) \right]^2 \right\rangle$$

$$= 4\Delta\beta \left[\sum_{m=0}^{\infty} \left(G_m G_{m+b} \left\langle \cos^2(2\pi f t + \psi_{m,b}) \right\rangle \right) \right.$$

$$\left. + \sum_{m=0}^{\infty} \sum_{\substack{n=0 \\ n \neq m}}^{\infty} \left(\sqrt{G_m G_{m+b} G_n G_{n+b}} \left\langle \cos(2\pi f t + \psi_{m,b}) \cos(2\pi f t + \psi_{n,b}) \right\rangle \right) \right]$$

$$= 4\Delta\beta \left[\sum_{m=0}^{\infty} \left(G_m G_{m+b} \left\langle \cos^2(2\pi f t + \psi_{m,b}) \right\rangle \right) \right.$$

$$+ \frac{1}{2} \sum_{m=0}^{\infty} \sum_{\substack{n=0 \\ n \neq m}}^{\infty} \left(\sqrt{G_m G_{m+b} G_n G_{n+b}} \left\langle \cos(4\pi f t + \psi_{m,b} + \psi_{n,b}) \right\rangle \right)$$

$$\left. + \frac{1}{2} \sum_{m=0}^{\infty} \sum_{\substack{n=0 \\ n \neq m}}^{\infty} \left(\sqrt{G_m G_{m+b} G_n G_{n+b}} \left\langle \cos(\psi_{m,b} - \psi_{n,b}) \right\rangle \right) \right], \tag{5.14}$$

where $\langle ... \rangle$ is the time average. The time averages for the three cosine terms are:

$$\left\langle \cos^2(2\pi f t + \psi_{m,b}) \right\rangle = 1/2$$
$$\left\langle \cos(4\pi f t + \psi_{m,b} + \psi_{n,b}) \right\rangle = 0$$
$$\left\langle \cos(\psi_{m,b} - \psi_{n,b}) \right\rangle = \cos(\psi_{m,b} - \psi_{n,b}), \tag{5.15}$$

and $P_{\mathrm{D,c}}(f)$ can thus be rewritten as:

$$P_{\mathrm{D,c}}(f) = 2\Delta\beta \sum_{m=0}^{\infty} (G_m G_{m+b}) + 2\Delta\beta \sum_{m=0}^{\infty} \sum_{\substack{n=0 \\ n \neq m}}^{\infty} \left(\sqrt{G_m G_{m+b} G_n G_{n+b}} \cos(\psi_{m,b} - \psi_{n,b}) \right). \tag{5.16}$$

The second term does not equal zero for any individual frequency. However, the term averages to zero over any small frequency interval, i.e. over any small interval in b.[†] Therefore, we ignore that term and write $P_{\mathrm{D,c}}(f)$ as:

$$P_{\mathrm{D,c}}(f) = 2\Delta\beta \sum_{m=0}^{\infty} (G_m G_{m+b}) = 2 \sum_{m=0}^{\infty} \left(G_{\mathrm{c}}(\beta_m) G_{\mathrm{c}}(\beta_m + f) \Delta\beta \right). \tag{5.17}$$

By letting $\Delta\beta \to 0$, we can rewrite the sum to an integral:

$$P_{\mathrm{D,c}}(f) = 2 \int_0^{\infty} G_{\mathrm{c}}(\beta) G_{\mathrm{c}}(\beta + f) \, \mathrm{d}\beta = 2(G_{\mathrm{c}} \star G_{\mathrm{c}})(f), \tag{5.18}$$

where $\star$ denotes the cross correlation (note that $G_{\mathrm{c}}(\beta) = 0$ for $\beta < 0$). As stated above, $f > 0$ in this derivation, and therefore $P_{\mathrm{D,c}}(f)$ is extended for $f \leq 0$ so that:

$$P_{\mathrm{D,c}}(f) = \begin{cases} 2(G_{\mathrm{c}} \star G_{\mathrm{c}})(f) & \text{for} \quad f > 0 \\ 0 & \text{for} \quad f \leq 0 \end{cases} . \tag{5.19}$$

The assumption of spatial coherence over the whole detector can be relaxed as suggested below. Any given point on the detector is highly correlated with points within a certain area around the point. This area is called a coherence area A_{c}, and the size of A_{c} can

---

[†] This statement has been validated by numerically calculating the term over various intervals in b for random phases ϕ_m, $B_m = 1$ for all m, and $\Delta\beta = 1/N$ where N was finite.

be predicted based on the wavelength of the light λ_L and the solid angle Ω between the area of illumination and each point on the detector: [109]

$$A_c \approx \lambda_L^2 / \Omega. \tag{5.20}$$

Since the distance D between the fiber tip or the surface area on the tissue from which the backscattered light illuminates the detector, is usually much larger that the radius r of the fiber tip or the tissue area, the solid angle can be approximated to:

$$\Omega \approx \pi r^2 / D^2. \tag{5.21}$$

In total

$$n_c = A_{det} / A_c \tag{5.22}$$

coherence areas fit on the detector, which for the case of the simulated setup used for Figure 5.2 gives $n_c \approx 8$. Each coherence area can be considered as an independent realization of the same stochastic process and $i_{dc,c}$, $i_{ac,c}$, and $P_{D,c}(f)$ derived above are thus valid for each single coherence area. The static current generated over the whole detector is simply summarized as:

$$i_{dc} = \sum_{n_c} i_{dc,c} = n_c i_{dc,c}, \tag{5.23}$$

whereas, due to the random phases between the various $i_{ac,c}$, the time varying part of the whole detector is rather summarized to:

$$i_{ac} = \sum_{n_c} i_{ac,c} = \sqrt{n_c} i_{ac,c}. \tag{5.24}$$

In analogy with Equation 5.8, the optical Doppler spectrum $G(\beta)$ over the whole detector is normalized so that

$$\int_0^\infty G(\beta)\, d\beta = i_{dc}. \tag{5.25}$$

It then follows from Equations 5.8, 5.23, and 5.25 that

$$G(\beta) = n_c G_c(\beta). \tag{5.26}$$

By combining 5.14, 5.18, 5.24, and 5.26, the Doppler power spectrum generated by the whole detector can be expressed as:

$$P_D(f) = \begin{cases} \frac{2}{n_c}(G \star G)(f) & \text{for} \quad f > 0 \\ 0 & \text{for} \quad f \leq 0 \end{cases}. \tag{5.27}$$

In Figure 5.3, the effect of an increased velocity (a) and an increased RBC tissue fraction (b) on the Doppler power spectrum is shown. It can be seen that an increased velocity broadens the spectrum, whereas an increased RBC tissue fraction first increases the power for all frequencies > 0 Hz, and for high tissue fractions also causes a significant broadening due to multiple Doppler shifts. These spectra are based on Monte Carlo simulations of a static homogeneous medium with $\mu_a = 0.1$ mm^{-1}, $\mu_s = 13$ mm^{-1}, and $g = 0.85$, containing RBC:s in blood (435 g RBC/liter blood, HCT = 42%) with $\mu_a = 0.5$ mm^{-1}, $\mu_s = 222$ mm^{-1}, and $g = 0.991$ (a Gegenbauer kernel phase function with $\alpha_{Gk} = 1.0$ and $g_{Gk} = 0.948$). The optical Doppler spectra $G(\beta)$ were given by the simulation and the Doppler power spectra calculated using Equation 5.17 (see also Section 5.5). In Figure 5.3a, the RBC tissue fraction was 0.1 g RBC / 100 g tissue (or %) and the RBC velocity shown on the x-axis was the mean velocity of a rectangular velocity

distribution between 0 and twice that mean velocity. In Figure 5.3b the velocity of the RBC:s was evenly distributed between 0 and 5 mm/s. The fiber separation was 0.25 mm, and both emitting and receiving fibers had a core diameter of 0.125 mm and NA = 0.37.
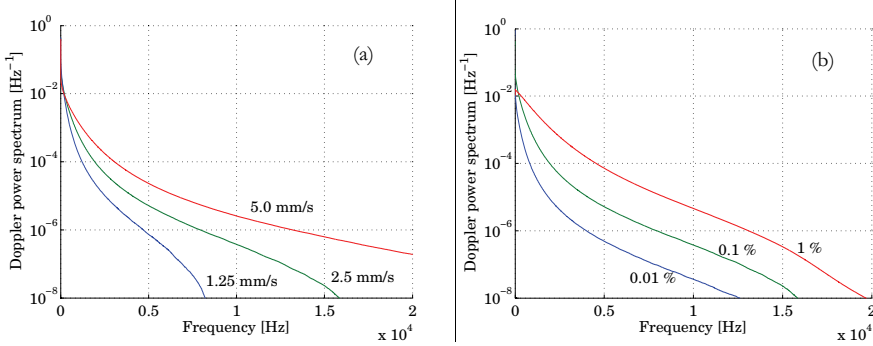

Figure 5.3 Effect on the Doppler power spectrum for increased velocity (a) and increased RBC tissue fraction (b).

5.3   Conventional measures

The conventional perfusion measure is calculated as the first moment of the Doppler power spectrum normalized with i_{dc}^2: [9]

$$s_{perf} = \frac{\int_{-\infty}^{\infty} f P_D(f) \, df}{i_{dc}^2}. \tag{5.28}$$

Note that $P_D(f) = 0$ for $f \leq 0$ (Equation 5.19). Similarly, an RBC tissue fraction estimate is calculated as:

$$s_{CMBC} = \frac{\int_{-\infty}^{\infty} P_D(f) \, df}{i_{dc}^2}, \tag{5.29}$$

where CMBC is a commonly used abbreviation for the concentration of moving RBC:s. The meaning of these measures was first evaluated by Bonner and Nossal. [8]   The evaluation in this section is based on Larsson [108] and partly previously presented in [107]. A homogeneous medium is assumed.

First, Beer-Lambert s law (Equation 3.1) lets us estimate the fraction of non Doppler shifted photons:

$$\zeta_0 \approx e^{-\langle d \rangle \zeta_{RBC} \mu_{s,RBC}}, \tag{5.30}$$

where $\langle d \rangle$ is the average path length, ζ_{RBC} is the tissue fraction of RBC:s, and $\mu_{s,RBC}$ is the scattering coefficient of the RBC:s. Since we really have a distribution of path lengths, this is only an approximation that introduces significant errors, but it is enough for the examination in this section. We also define the fraction of Doppler shifted photons $\zeta_D = 1 - \zeta_0$, and introduce:

$$H(\beta) = G(\beta)(1 - \delta(\beta - \beta_L))/(i_{dc}\zeta_D), \tag{5.31}$$

where δ is Dirac's delta function. Note that $\int_{-\infty}^{\infty} H(\beta) d\beta = 1$. Furthermore, $G(\beta)$ is divided into one non Doppler shifted part $G_0(\beta)$ and one Doppler shifted part $G_D(\beta)$ as: (remember Equation 5.8)

$$\begin{cases} G_0(\beta) = i_{\text{dc}}\zeta_0\delta(\beta - \beta_{\text{L}}) \\ G_{\text{D}}(\beta) = i_{\text{dc}}\zeta_{\text{D}}H(\beta) \end{cases}.$$ (5.32)

By using Equation 5.27, $P_{\text{D}}(f)$ can then be rewritten as:

$$\begin{aligned} P_{\text{D}}(f) &= 2n_{\text{c}}^{-1}(G \star G)(f) \\ &= 2n_{\text{c}}^{-1}\big((G_0 + G_{\text{D}}) \star (G_0 + G_{\text{D}})\big)(f) \\ &= 2n_{\text{c}}^{-1}\Big(\underbrace{(G_0 \star G_0)(f)}_{\text{stationary}} + 2\underbrace{(G_0 \star G_{\text{D}})(f)}_{\text{heterodyne}} + \underbrace{(G_{\text{D}} \star G_{\text{D}})(f)}_{\text{homodyne}} \Big) \end{aligned}$$ (5.33)

for $f > 0$. The stationary, heterodyne, and homodyne terms can be rewritten as:

$$\begin{aligned} (G_0 \star G_0)(f) &= \int_{-\infty}^{\infty} G_0(\beta)G_0(\beta + f)\,\mathrm{d}\beta \\ &= i_{\text{dc}}^2\zeta_0^2 \int_{-\infty}^{\infty} \delta(\beta - \beta_{\text{L}})\delta(\beta - \beta_{\text{L}} + f)\,\mathrm{d}\beta \\ &= i_{\text{dc}}^2\zeta_0^2\delta(f) \\ &= 0 \ \text{ for } f > 0, \end{aligned}$$ (5.34)

$$\begin{aligned} (G_0 \star G_{\text{D}})(f) &= \int_{-\infty}^{\infty} G_0(\beta)G_{\text{D}}(\beta + f)\,\mathrm{d}\beta \\ &= i_{\text{dc}}^2\zeta_0\zeta_{\text{D}} \int_{-\infty}^{\infty} \delta(\beta - \beta_{\text{L}})H(\beta + f)\,\mathrm{d}\beta \\ &= i_{\text{dc}}^2\zeta_0\zeta_{\text{D}}H(\beta_{\text{L}} + f), \end{aligned}$$ (5.35)

$$\begin{aligned} (G_{\text{D}} \star G_{\text{D}})(f) &= \int_{-\infty}^{\infty} G_{\text{D}}(\beta)G_{\text{D}}(\beta + f)\,\mathrm{d}\beta \\ &= i_{\text{dc}}^2\zeta_{\text{D}}^2 \int_{-\infty}^{\infty} H(\beta)H(\beta + f)\,\mathrm{d}\beta. \end{aligned}$$ (5.36)

Inserting Equations 5.34-5.36 into 5.33 gives:

$$P_{\text{D}}(f) = 2n_{\text{c}}^{-1}i_{\text{dc}}^2\Big(2\zeta_0\zeta_{\text{D}}H(\beta_{\text{L}} + f) + \zeta_{\text{D}}^2 \int_{-\infty}^{\infty} H(\beta)H(\beta + f)\,\mathrm{d}\beta \Big)$$ (5.37)

for $f > 0$. Inserting this result into Equation 5.29 yields:

$$\begin{aligned} s_{\text{CMBC}} &= \frac{\displaystyle\int_{-\infty}^{\infty} P_{\text{D}}(f)\,\mathrm{d}f}{i_{\text{dc}}^2} \\ &= \frac{2i_{\text{dc}}^2}{n_{\text{c}}i_{\text{dc}}^2}\Big(2\zeta_0\zeta_{\text{D}} \int_{-\infty}^{\infty} H(\beta_{\text{L}} + f)\,\mathrm{d}f + \zeta_{\text{D}}^2 \int_{-\infty}^{\infty}\int_{-\infty}^{\infty} H(\beta)H(\beta + f)\,\mathrm{d}\beta\,\mathrm{d}f \Big) \\ &= \frac{2}{n_{\text{c}}}\Big(2\zeta_0\zeta_{\text{D}} + \zeta_{\text{D}}^2 \int_{-\infty}^{\infty} H(\beta) \int_{-\infty}^{\infty} H(\beta + f)\,\mathrm{d}f\,\mathrm{d}\beta \Big) \\ &= \frac{2}{n_{\text{c}}}\Big(2\zeta_0\zeta_{\text{D}} + \zeta_{\text{D}}^2 \int_{-\infty}^{\infty} H(\beta)\,\mathrm{d}\beta \Big) \\ &= \frac{2}{n_{\text{c}}}(2\zeta_0\zeta_{\text{D}} + \zeta_{\text{D}}^2) \\ &= \frac{2}{n_{\text{c}}}(1 - \zeta_0^2) \\ &\approx \underbrace{\frac{2}{n_{\text{c}}}}_{\mathbb{A}} \underbrace{(1 - e^{-2\langle d \rangle c_{\text{RBC}}\mu_{\text{s,RBC}}})}_{\mathbb{B}}, \end{aligned}$$ (5.38)

and similarly when inserted into Equation 5.28:

$$s_{\text{perf}} = \frac{\displaystyle\int_{-\infty}^{\infty} f P_{\text{D}}(f)\,\mathrm{d}f}{i_{\text{dc}}^2}$$

$$= \langle f \rangle \frac{\displaystyle\int_{-\infty}^{\infty} P_{\text{D}}(f)\,\mathrm{d}f}{i_{\text{dc}}^2}$$

$$\approx \underbrace{\langle f \rangle}_{\mathbb{C}} \underbrace{\frac{2}{n_{\text{c}}}}_{\mathbb{A}} \underbrace{(1 - e^{-2\langle d \rangle c_{\text{RBC}} \mu_{\text{s,RBC}}})}_{\mathbb{B}}, \tag{5.39}$$

where $\langle f \rangle$ is the average frequency of $P_{\text{D}}(f)$. To understand the meaning of s_{CMBC} and s_{perf}, each of the terms $\mathbb{A}$, $\mathbb{B}$, and $\mathbb{C}$ are now analyzed. Term $\mathbb{A}$ is constant as long as n_{c} is constant, which may not be the case in an LDPI system (see Section 5.4). In practice, i_{ac} and i_{dc} are often processed separately giving two different amplification of the signals, which implies that the term $\mathbb{A}$ may rather be $(2k_{\text{ac}}^2)/(n_{\text{c}}k_{\text{dc}}^2)$.

Term $\mathbb{B}$ can be rewritten using the Maclaurin series expansion of e, i.e. $e^x = 1 + x/1! + x^2/2! + ...$. For low RBC tissue fractions, $\mathbb{B}$ can thus be approximated to $2\langle d \rangle c_{\text{RBC}} \mu_{\text{s,RBC}}$, which is linear to the RBC tissue fraction. For higher RBC tissue fractions, higher order moments of the Maclaurin series have to be considered, introducing non-linearities. This leads to the CMBC and perfusion values being underestimated for higher RBC tissue fractions. Furthermore, the path length generally decreases when the RBC tissue fraction increases [IV], making the underestimation even worse.

We know from Equation 4.13 that the size of each Doppler shift is linearly dependent on the velocity of the moving RBC. Therefore term $\mathbb{C}$ will be linearly dependent on the RMS velocity of RBC:s, [8] under the assumption that everything else is constant and the bandwidth of the system is wide enough. However, the average frequency increases when the photons are multiple Doppler shifted, which they are to a greater extent when the RBC tissue fraction is high. This compensates the nonlinearities introduced in term $\mathbb{B}$ to some extent, but not entirely.

In conclusion, CMBC reflects the concentration (tissue fraction) of moving RBC:s and the perfusion estimate reflects the tissue fraction of RBC:s times their average velocity. It can also be noted that since s_{CMBC} and s_{perf} are normalized with i_{dc}^2, they are independent of the total detected light intensity. The relationship between the tissue fraction of RBC:s in a homogeneous medium and simulated s_{CMBC} and s_{perf} are shown in Figure 5.4. The simulated setup was the same as described at the end of Section 5.2. The velocity of the RBC:s in the medium was evenly distributed between 0 and 5 mm/s. In this figure, the non-linear behavior of especially s_{CMBC}, but also s_{perf}, becomes evident. It must be emphasized that the non-linearity is strongly dependent on the geometry and optical properties of the medium and can therefore not be easily accounted for, as suggested in [9].
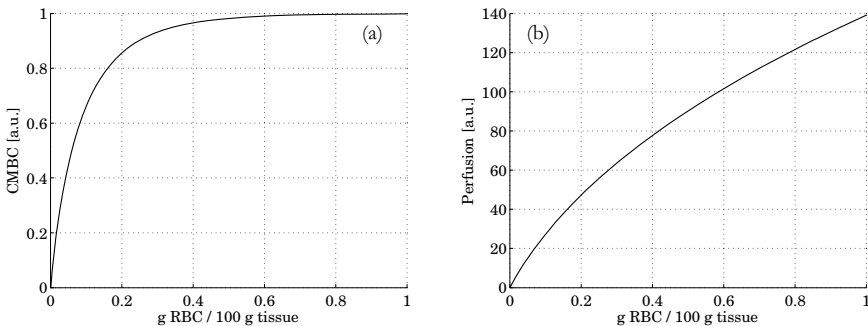

Figure 5.4 Relationship between RBC tissue fraction and s_{CMBC} (a) and s_{perf} (b).

5.4 Hardware realizations

As stated in the introduction to this chapter, there exist single point (LDPM) and imaging (LDPI) LDF systems. In this section, the special characteristics of these systems, as well as a newer type of imaging systems based on fast CMOS cameras, are described. Noise reduction and typical calibration procedures are also described.

5.4.1 LDPM

In single point systems, optical fibers are typically used to guide the light from the laser source to the tissue and from the tissue to the detector. Most often separate fibers are used, but a single fiber can also be used when a very small measurement volume is wanted [IV]. The most common source-detector distance in probes provided by the two leading manufacturers of LDF instruments (Perimed AB, Järfälla, Sweden, and Moor Instruments Ltd, Axminster, UK) is 0.25 mm. Generally, short source-detector distances have been preferred to limit the measurement depth, and to avoid a high degree of multiple Doppler shifts leading to severe non-linearities in the conventional CMBC and perfusion measures.

In a fiber based system, the detector fiber illuminates the detector at a certain distance between the fiber tip and the detector (Figure 5.5a). The illuminating angle is constant and determined from the numerical aperture of the fiber, under the reasonable assumption that the light impinging the fiber has a uniform angle distribution. During these conditions, the number of coherence areas on the detector is constant (Equation 5.22), and the dc-squared normalized Doppler power spectrum $P_D(f)/i_{dc}^2$ will only depend on the optical spectrum $B(\beta)$ (Equation 5.27).

Another type of LDPM systems, not based on fibers, also exists, where the optics and electronics are built on a single chip that is in direct contact with the tissue. [110] These systems are less sensitive to movements and can therefore be used under less controlled situations, but at low perfusion levels, the SNR is lower due to the shorter coherence length of the lasers used.

5.4.2 LDPI

In a conventional imaging system (Figure 5.5b), a laser beam is scanned over the tissue of interest to form an image. In each scanning position, the perfusion value is calculated and transformed into a pixel value, and the scanning procedure lasts for a couple of minutes to form an entire image. The detector is typically placed some 20-30 cm above the tissue surface. In some systems a lens focuses the light on the detector.

The backscattered light from the impinging laser beam escapes the tissue from a spot centered in the point of injection, with a radially decaying intensity. The slope of the decay, and thus the apparent spot size, is strongly dependent on the absorption properties of the tissue (see also Section 3.3.4 about SRDR). The spot size, by itself, reduces the calculated perfusion value since it affects the solid angle to the detector points. Since an increased RBC tissue fraction increases the total absorption of the tissue and thus reduces the spot size, the increase in the estimated CMBC and perfusion will be underestimated. The effect, which is explained below, is similar for both systems with and without a light focusing lens in front of the detector (see also [111]).

For simplicity, assume that the backscattered light exits the tissue in a homogeneous spot. For a system without a lens in front of the detector, the solid angle between the spot and each point on the detector varies with the radius r of the spot squared (Equation 5.21). As given by Equation 5.39, the perfusion value is inversely proportional to the number of coherence areas n_c, which in turn is linearly dependent on r^2 (Equations 5.20-5.22). Therefore, the calculated perfusion value is inversely proportional to r^2 for a system without a lens.

For a system with a light focusing lens, the solid angle is determined by the dimension and position of the lens and is thus independent on the spot size. However, as the lens

focuses the light on the detector, the illuminated part of the detector will depend directly on the size of the spot, under the assumption that the entire spot is imaged on the detector. Therefore, the "active" detector area will depend on r^2, and the calculated perfusion value is inversely proportional to r^2 also for a system with a lens.

5.4.3 CMOS imager

A conventional LDPI system has the drawbacks that it is slow and that the estimated perfusion value is affected by the spot size of back reflected light. Both these drawbacks are addressed with the new generation of LDPI systems, which are based on fast CMOS cameras. [112,113] In these systems, the backscattered light is focused on a detector array, where every pixel in the array is used to calculate a perfusion value from the part of the tissue that the pixel sees (Figure 5.5c). By simultaneously illuminating the whole tissue area of interest, the whole image is acquired simultaneously, which is naturally faster than to scan the area point by point. Every pixel in the array also has a constant solid angle (based on the lens) and they can be assumed to be evenly illuminated, so the perfusion value is independent of the spot size.

The big drawback with these systems is that the cameras used are not yet fast enough. A normal Doppler power spectrum has frequency components of significant power up to about 15 kHz (see for example [II]). The sample frequency thus has to be at least 30 kHz to collect the entire frequency content of the Doppler signal, and to avoid aliasing. The system presented in [113] operated with a sampling frequency of only 8 kHz, which will have the effect that when the velocity of the RBC:s is increased, a substantial part of the energy in the Doppler power spectrum will exceed 4 kHz, and the expected increase in the perfusion value will be underestimated, or the perfusion value may even decrease.
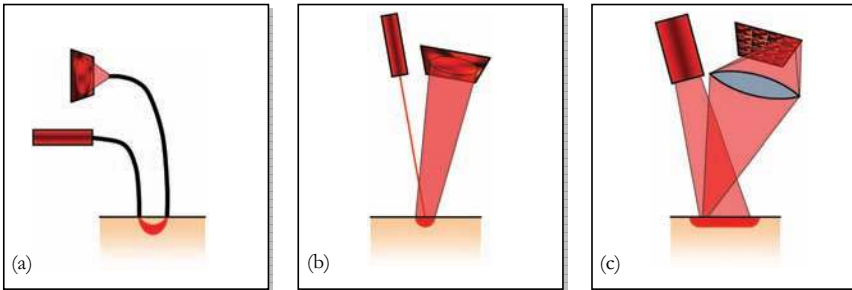

Figure 5.5 Schematic illustrations of the various LDF modalities, LDPM (a), LDPI (b), and CMOS imager (c).

5.4.4 Noise

Various types of noise influence the Doppler power spectrum. Some of this noise originates from variations in background light intensity and other common mode noise. To get rid of this type of noise, a differential detector technique is often used for i_{ac}, that simply calculates the difference between the light falling on two adjacent detectors. By calculating the difference, common noise is cancelled out, whereas the statistical properties of the two separate realizations of i_{ac} are kept. [6]

Other types of noise are not removed by this technique, though. The amplitude of shot noise, which is a variation in the photoelectron emission rate of the detector, is linearly dependent on the total detector current i_{dc}, whereas thermal noise is constant as long as the temperature is held constant. [114] Consequently, an expression of these types of noise can be established:

$$P_{noise}(f, i_{dc}) = k_{noise}(f)i_{dc} + l_{noise}(f), \tag{5.40}$$

where the parameter k_{noise} relates to the shot noise and l_{noise} to the thermal noise.

5.4.5   Calibration

Two different objectives are reached when calibrating an LDF system. Firstly, the noise parameters k_{noise} and l_{noise} in Equation 5.40 are calculated. This is done by measuring the signal at different dc-levels on a static scattering object, i.e. an object without any moving scatterers, such as a piece of white plastic. The noise perfusion value is then calculated and subtracted from the measured perfusion values during the normal measurements.

Secondly, a reference perfusion value is measured. In the Periflux 5000 system (Perimed AB, Järfälla, Sweden), this is achieved by placing the measurement probe in a beaker containing a certain concentration of polystyrene microspheres diluted in water, a so-called motility standard. Due to Brownian motion, these microspheres, acting as scatterers, move with a certain velocity distribution which is dependent on the temperature. Thus, all backscattered light is Doppler shifted and in the case of the Periflux 5000 system, the perfusion level measured in this setup is set to 250 p.u. (perfusion units). Since this is a repeatable procedure, all other perfusion values can be compared. Other systems have similar calibration routines.

The calibration procedure in the new method presented in this thesis differs slightly from the procedure described above. Firstly, the noise spectrum $P_{\text{noise}}(f, i_{\text{dc}})$ is subtracted directly from the Doppler power spectrum $P_{\text{D}}(f)$. Secondly, the resulting Doppler power spectrum is normalized with the CMBC from the motility measurement, which is calculated as:

$$s_{\text{CMBC,mot}} = \frac{\int_{-\infty}^{\infty} (P_{\text{mot}}(f) - P_{\text{noise}}(i_{\text{dc,mot}}, f)) \, \mathrm{d}f}{i_{\text{dc,mot}}^2}. \tag{5.41}$$

Thus, the calibrated Doppler power spectrum is calculated as

$$P_{\text{D}}'(f) = \frac{P_{\text{D}}(f) - P_{\text{noise}}(i_{\text{dc}}, f)}{i_{\text{dc}}^2} \bigg/ s_{\text{CMBC,mot}}. \tag{5.42}$$

The modification of the second calibration step results in the CMBC of a measurement where all light is Doppler shifted being unity (see Equation 5.38). The measured Doppler power spectra can thus easily be compared to simulated spectra. Another positive consequence of this is that the second calibration step can be performed with any scattering liquid where Brownian motion is present, and is not limited to expensive motility standard that has to be exchanged from time to time and is independent of the temperature.

5.4.6   The biological zero

In LDF, a phenomenon called biological zero (BZ) has long been known and debated. [115-119] The BZ signal is the recorded non-zero perfusion signal that still remains when the flow is obviously arrested, and it is believed that the signal originates from Brownian motion of trapped blood cells and maybe other moving constitutes in the tissue. [120,121]

Many authors have suggested that the BZ signal should simply be subtracted from the conventional perfusion estimate for more correct results. [116,121] However, even when assuming that the movements causing the BZ still remain during normal flow conditions, that the measurement volume is the same, and that the effect of the BZ mixes with all detected light, it is theoretically incorrect to subtract the BZ and that will result in an underestimation of the perfusion. Mixing of optical spectra is simply not linear to the conventional perfusion estimate. This has been tested by calculating the forward problem described in Section 7.2, and is also supported by Zhong *et al.* who performed a mathematical analysis of the BZ problem. [122] It is also likely that the measurement volume is not the same during the BZ measurement as during normal condition measurements due to for example a reduced blood tissue fraction [IV], which would also

suggest that the BZ signal is different during the BZ measurement than during normal condition measurements. Finally, it may be questioned if the Brownian motion that is believed to cause the BZ remains to the same extent during normal flow conditions. [20] All of this argues against a subtraction of the BZ in conventional LDF.

5.5   Monte Carlo and LDF

Although the Doppler effect is a light wave phenomenon, the Monte Carlo technique that is based on the particle representation of light has been used throughout this thesis to quantify the Doppler power spectrum from a simulated medium. This may seem contradictory. However, each individual Doppler shift is calculated using the wave representation of light (see Sections 5.1 and 4.1.8) and the Doppler shift of each photon is then stored as an extra attribute of the photon in the Monte Carlo simulation. The calculation of the Doppler power spectrum is based on the optical Doppler spectrum, which is given from the distribution of photons with different total Doppler shifts. In summary, the photons in the Monte Carlo simulations behave as information carriers, but both the individual Doppler shifts and the resulting Doppler power spectra are calculated using light wave theory, using input from the information carrying photons.

It has frequently been shown that Doppler power spectra calculated with the aid of Monte Carlo simulations correlate with *ex vivo* measurements for LDPM [33,34,81,123] [I]. Some of the papers included in this thesis also show that they correlate well with *in vivo* measurements [II, V-VI]. For LDPI on the other hand, see the subsection below.

5.5.1   Simulating LDPI

In a conventional LDPI system, with or without a light collecting lens in front of the detector, the intensity of all coherence areas can not be assumed to be equal, as for an LDPM system. This has to be accounted for when calculating the Doppler power spectrum from a simulation. A description of this is given in this section. Most of this description has previously been presented in [IV], but is here treated in some more detail.

In any LDF system, the estimated perfusion scales with the frequency content and the magnitude of the time varying part of the photo detector current i_{ac}, normalized with the average total detector current i_{dc} squared (see for example Equation 5.28). The variation in i_{ac} is expressed as the variance $\langle i_{ac}^2 \rangle$. For each coherence area i on the detector, this variation can be calculated from the fraction of Doppler shifted photons $\zeta_{D,i}$ impinging the coherence area [124] as

$$\langle i_{ac}^2 \rangle_i = \langle i_{dc} \rangle_i^2 \zeta_{D,i}(2 - \zeta_{D,i}), \tag{5.43}$$

where $\langle i_{dc} \rangle_i$ is the average detector current generated by coherence area i. The values of $\zeta_{D,i}$ and $\langle i_{dc} \rangle_i$ are given from the Monte Carlo simulations as the fraction of Doppler shifted photons and the total amount of photons, respectively, impinging coherence area i.

The average total detector current is simply given as

$$\langle i_{dc} \rangle = \sum_{i=1}^{n_c} \langle i_{dc} \rangle_i, \tag{5.44}$$

where n_c is the number of coherence areas. The time varying part of the detector current, i_{ac}, can not be summarized that easily. However, the stochastic nature of the speckle pattern implies that each speckle (i.e. coherence area) can be treated as an independent realization of the same stochastic process. As a consequence, the variance of the total detected signal can be expressed as

$$\langle i_{ac}^2 \rangle = \sum_{i=1}^{n_c} \langle i_{ac}^2 \rangle_i. \tag{5.45}$$

For a moment, consider the situation where the average total detector current $\langle i_{dc} \rangle$ is constant and $\langle i_{dc} \rangle_i$ and $\zeta_{D,i}$ are equal for all coherence areas. It can then be realized from Equations 5.43-5.45 that the magnitude of $\langle i_{ac}^2 \rangle$ and hence the perfusion value decreases when the number of coherence areas n_c increases, and are maximal for $n_c = 1$. In analogy, for a constant number of coherence areas n_c, $\langle i_{ac}^2 \rangle$ will be larger when most of the average total detector current $\langle i_{dc} \rangle$ is concentrated to a few coherence areas, i.e. $\langle i_{dc} \rangle_i$ is high for a few i and small for other i:s, than if all $\langle i_{dc} \rangle_i$ are similar. In an LDPI system without a light collecting lens in front of the detector, it can be assumed that all $\langle i_{dc} \rangle_i$ are equal, but the number of coherence areas n_c varies with the spot size of the backscattered light on the tissue surface. In an LDPI system with a lens that focuses the light on the detector the number of coherence areas is rather given by the solid angle between the lens and the detector (see Equations 5.20-5.22), but $\langle i_{dc} \rangle_i$ varies over the detector area and is largest in the point where the center of the backscattered light is imaged, decreasing toward the edges. Thus, for both types of systems, the perfusion estimate will be at the highest when the light is backscattered in a small point on the tissue surface.

The following derivation is based on a system with a light collecting lens. To account for the variation in $\langle i_{dc} \rangle_i$ when analyzing LDPI simulations, the detector surface is divided into n_c equally sized bins, each representing one coherence area (it is not important exactly how this division is done). Each photon is assigned to a single bin according to its position of detection. For each bin, $\langle i_{ac}^2 \rangle_i$ is calculated according to Equation 5.43. According to that equation, the intensity $\langle i_{dc} \rangle_i$ in each coherence area does not linearly contribute to $\langle i_{ac}^2 \rangle_i$, and therefore not linearly to $\langle i_{ac}^2 \rangle$ (Equation 5.45) and the perfusion value. Consequently, when the intensity varies over the detector, each photon weight that contributes linearly to the light intensity $\langle i_{dc} \rangle_i$ will not contribute linearly to the Doppler power spectrum. Therefore, in order to calculate the Doppler power spectrum for an LDPI setup, the weight of each photon $w_{i,j}$ has to be adjusted. Assume that this weight adjustment fulfills

$$\begin{cases} \sum_{j \in D_i} w'_{i,j} = \langle i_{ac}^2 \rangle_i \\ w'_{i,j} = k_i w_{i,j} \end{cases}, \tag{5.46}$$

where $w'_{i,j}$ is the adjusted photon weight of Doppler shifted photon j in coherence area i, D_i is the Doppler shifted photons in that coherence area, and k_i the weight adjusting coefficient for the photons in coherence area i. This implies that the sum of the reweighted photons in coherence area i is equal to $\langle i_{ac}^2 \rangle_i$, and all photons within one coherence area are reweighted with the same factor. Thus, the weight of every Doppler shifted photon is adjusted according to

$$w'_{i,j} = \langle i_{ac}^2 \rangle_i w_{i,j} \Big/ \sum_{j \in D_i} w_{i,j}. \tag{5.47}$$

The adjusted photon weight $w'_{i,j}$ can then be used to calculate the Doppler power spectrum from a simulation in the LDPI setups.

Although the reasoning above was given for a system with a light collecting lens, it is reasonable to assume that the same reweighting can be done to get an accurate result also for systems without a lens. Rajan *et al.* have shown that the effect is identical for both types of systems at least when the backscattered spot on the tissue surface is homogeneous. [111] In an LDPM system on the other hand, all coherence areas have equal intensity and a constant size, depending only on the fiber-detector properties and not the tissue optical properties (i.e. the number of coherence areas is hardware dependent only). [124] Therefore, the weight adjustment in Equation 5.47 is identical for all photons and the Doppler power spectrum is not affected by it, and is therefore unnecessary. The same is true for a CMOS based imaging system, where it can be assumed that the light intensity is homogeneous in each detector element due to their small size and the broad laser beam illuminating the tissue.

6   Medical background

Quantitative laser Doppler flowmetry, as presented in this thesis, is based on model adaption to measurements. For accurate results, it is important that the model parameters are chosen carefully. Therefore, as all *in vivo* measurements presented in the thesis are performed on skin, the structure of the skin (Section 6.1) as well as the characteristics of the microcirculation (Section 6.2) is described in this chapter, and the model is based on that knowledge. Furthermore, the local heat regulation of the skin is described (Section 6.2.1), as local heating is a provocation that has been used in the measurements, and the microvascular changes that often arise in diabetics are described (Section 6.2.2), as the clinical study in Paper VI is performed on patients with diabetes type 2.

6.1   Structure of the skin

The skin, the largest organ of the human body, constitutes a physical barrier to the external environment. Other important functions of the skin include body temperature regulation and functioning as a blood reservoir. It has a thickness in adults ranging from 0.5 mm (the eye lids) to 4.0 mm (the heel), but the average thickness is 1-2 mm. Two distinct layers can be observed in skin, the superficial thin epidermis, and the deeper and thicker dermis. A third layer, subcutis (subcutaneous fat or hypodermis), is located below dermis, but is strictly not a part of the skin. [125]

Epidermis, itself, is often divided into four to five subgroups. The deepest layer is responsible for creating new cells, and in the higher layers the cells are continuously degenerated, flattened, and more and more packed, until they are shed. The degeneration causes the cells to release a lipid-rich secretion that contributes to the water-repellant properties of skin. [125]

The epidermis contains the chromophore melanin, which highly contributes to the apparent brownish color of the skin. The melanin is produced by special cells, melanosomes. The melanosomes really produce two different kinds of melanin, pheomelanin which is the major pigment in red hair, and eumelanin. [126] As eumelanin is found in considerably higher concentrations than pheomelanin in epidermis, and since eumelanin absorbs much more light than pheomelanin at the wavelengths relevant in this thesis (540-800 nm, see also Figure 3.1), this is the only type considered here. The total amount of eumelanin in the epidermis depends both on the number of melanosomes and the amount of eumelanin they produce. The concentration varies from about 1-3% (wet weight) in fair skin to up to 43% in black skin [53,126]. The dermis contains no or very little melanin.

The epidermis contains no blood vessels, but the basal cell layers are supported by the capillary loops of the papillary dermis, that is the top layer of the dermis. This layer got its name from the papillary shape of this region, where the epidermis and dermis are connected in fingerlike junctions, which contain these capillary loops. The rest of the dermis is called reticular dermis and consists of dense connective tissue of collagen and elastic fibers. This gives the skin strength, extensibility, and elasticity. Directly beneath the papillary dermis, a plexus of blood vessels exists that supports the capillary loops. Another blood plexus of larger blood vessels is present at the border between the dermis and subcutis. In both these plexa, the blood vessels are orientated parallel to the skin, whereas sparse blood vessels connect the plexa and are thus orientated perpendicular to the skin.

The above described structure of the skin motivates the skin model developed in Paper II and illustrated in Figure 6.1. For details about that skin model, see Section 8.2 or Paper II.
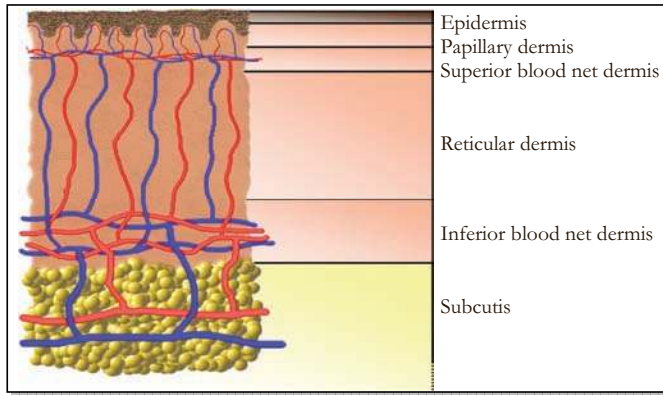
Figure 6.1 Illustration of the skin structure (left) that motivates the layered structure of the skin model.

Apart from blood vessels, the skin also contains other structures such as hair, smooth muscle, nerves, and glands. Hair is present on most skin sites except the palms, soles, and the palmar side of the digits. [125] Besides the scalp and the forehead, the number of hair follicles in the skin varies between about $0.1/mm^2$ on e.g. the calf to about $0.4/mm^2$ on e.g. the upper arm. The follicle diameter varies from about 50 μm on e.g. the volar side of the forearm to up to sometimes above 200 μm on e.g. the calf. [127]

Oil glands are mostly located in connection with the hair follicles and prevent the hairs from drying or becoming brittle. [125] The most common type of sweat glands, the eccrine sweat glands, are mainly located in the deep dermis and secrete sweat on the surface of the epidermis. On the forehead, palms, and soles, their density can be up to almost $5/mm^2$. [125]

Due to the relatively small size and low density of hair follicles and sweat glands, they are not a part of the skin model in Paper II. However, their effect on the quantitative LDF method presented in Paper V is evaluated there. Smooth muscle and nerves are even smaller structures than hair follicles and sweat glands, and their optical properties are assumed to be similar to the optical properties of the surrounding skin. Thus, their eventual minimal effect on the quantitative LDF method has been neglected.

6.2 Microcirculation

All living cells in the body are supported with oxygen and nutrients via the blood, which is oxygenized in the lungs and pumped out in the body by the heart. The blood is transported from the heart through the aorta, which is successively branched into smaller and smaller arteries, which eventually branch into arterioles and finally into the capillaries. In the capillaries, the oxygen and nutrients are transferred to the cells and waste products from the cells are returned to the blood. The blood returns from the capillaries to the heart via the venules which are joined into larger and larger veins and finally into the venae cavae. The microcirculation is usually defined as the vessels with a diameter less than 100 μm, including the arterioles, capillaries, and venules.

Although the aorta has the largest cross sectional area of all vessels in the body, the total cross sectional area of the smaller vessels is larger. Since there is a direct inverse relationship between the total cross sectional area of a vessel type and their average flow velocity, the velocity is the highest in the aorta and smallest in the capillaries (Table 6.1).

Table 6.1 Total cross sectional area and mean blood velocity for various types of vessels. [128]

Vessel type	Area [cm^2]	$\langle v \rangle$ [mm/s]
Aorta	2.5	330
Small arteries	20	40
Arterioles	40	20
Capillaries	2500	0.3
Venules	250	3.3
Small veins	80	10
Venae cavae	8	100

Blood vessels are built up of several layers. The innermost layer of all blood vessels is constituted by endothelium, a continuous thin layer of cells. The endothelium is covered by a basement membrane, and these are the only two layers that constitute the capillaries. In arteries and veins, and also in arterioles and venules, the vessel wall also contains smooth muscle fibers (especially in the arteries and arterioles) and an outer coat, the tunica externa, that is composed mostly of elastic and collagen fibers. The arteries, especially large arteries, also contain additional elastic layers outside the basement membrane and inside the tunica externa. [129]

Due to the thin walls of the capillaries, some substances such as O_2, CO_2, glucose, amino acids, and hormones may diffuse through the wall. This is also possible through the walls of some small venules, but not in other types of vessels. [129] It is in this capillary exchange process the main purpose of the complex circulatory system is manifested.

The smooth muscle of the vessels may be sympathetically stimulated to contract which causes the diameter of the vessel lumen, i.e. the hollow center of the vessel, to decrease. This is called vasoconstriction. In contrast, a decrease of the stimulation or the presence of for example nitric oxide (NO) causes the vessel to increase its lumen diameter, called vasodilatation. The smooth muscle regulates the blood flow in the body, where the arterioles in particular are important when regulating the capillary flow. Smooth muscles situated between the arterioles and capillaries are called precapillary sphincters and control the blood flow into the individual capillaries. During normal conditions, these sphincters open and close about five to ten times per minute, a phenomenon called vasomotion. [129]

In most parts of the circulatory system, blood flow has alternative ways to get to the same location. An engineer would probably compare it with a parallel circuit in electricity. In anatomy, this is referred to as an anastomosis and exists both on the artery and the vein side of the circulatory system, but also between arterioles and venules, so called arteriovenous (AV) anastomoses or AV shunts. [129] The anatomical (i.e. normal) AV shunts, which bypass the nutritive capillary flow when open, are controlled by sympathetic nerves [130], and are most numerous in the skin of the hands, feet, and ears. [131] In some disorders, capillaries can also have the function of arteriovenous shunts, when the basement membrane grows thick and prevents the capillary exchange or when the blood is forced through the capillaries at high velocities which also prevents an effective capillary exchange. [132] Moreover, when the precapillary sphincters are closed, the blood is forced through special thoroughfare channels with minimal capillary exchange. [129]

About 60% of the total blood volume is present in the veins and venules under normal resting conditions, whereas the systemic capillaries hold only about 5% and the systemic arteries and arterioles about 15%. The other 20% is located in the heart and in the pulmonary vessels. The veins and venules, especially in the liver, spleen, and skin, thus function as a blood reservoir and the blood flow velocity in these vessels may under some circumstances be rather low. [129]

6.2.1 Microcirculatory heat regulation

One important role of the skin is to regulate the temperature of the body which is done by regulating the blood flow and by sweating, where the latter is not further treated in this section. [125] Heat reflexes that are invoked both by a global body temperature change and by local temperature changes exist. The principle is simple, during hyperthermia, the blood vessels in the skin dilate to increase the blood flow and heat loss, whereas during hypothermia the vessels constrict to stop the skin blood flow in order to minimize the heat loss. [133] The same principles apply for local warming and cooling. [133,134]

During local heating, two different responses cause the vessels to dilate. A first reflex is caused by sensory C-fibers that release various vasodilator substances. [133] This response takes place within a couple of minutes, but reduces again after an additional couple of minutes. [133,135] The second response is caused by synthesis of nitric oxide (NO). [133,135] The second response is slower, but on the other hand it does not decline with time but reaches a plateau after 25 to 30 minutes of warming, where the final level is proportional to the temperature used and reaches a maximum for temperatures above 42°C. [136]

The Raynoud phenomenon and its "counterpart" erythromelalgia [132] are examples of disorders that are directly connected to the thermoregulation in skin. [133] As seen in the next subsection, also diabetes mellitus (DM) affects the thermoregulation.

The heat regulation is a process foremost involving relatively large vessels in the microcirculation bypassing much of the nutritive flow. [131]

6.2.2 Diabetes and microcirculation

Functional defects in the microcirculation, which may eventually lead to microangiopathy, often occur very early in DM. The thickening of the capillary basement membrane caused by the increased blood glucose level is for example common. The exact effects of this are still uncertain, but it seems as if it leads to reduced capillary exchange properties and reduced arteriolar vasoreaction (vasoconstriction and vasodilatation) followed by reduced capillary recruitment. As a consequence, the blood supply to the sympathetic nerves controlling the vasoconstriction of small arteries, arterioles, and AV shunts, may become insufficient. [137,138] The latter leads to an increased venous pressure and consequently a reduced arteriovenous pressure over the capillaries, which leads to a further reduction in capillary flow. [139] An impaired vasoconstriction may also lead to capillary hyperperfusion which further reduces the capillary exchange. [137] In principle, a capillary hyperperfusion in combination with a thickened basement membrane transforms these capillaries to AV shunts.

Strong evidence has been presented that the distribution of blood flow in skin is disturbed in diabetic patients, especially in the feet. [140,141] This has also been observed using LDF, where it has been shown that the total skin blood flow is increased in diabetes patients although the capillary flow is decreased. [142,VI] This can be seen already at rest, but is more pronounced during for example postocclusive reactive hyperemia and it is suggested that the effect is most likely due to AV shunting. [142]

In nonglabrous, i.e. hairy, skin a reduced vasodilator response to heat stimuli has frequently been shown, both in the foot and forearm. [143-145,VI] This is due to C-fiber impairment in both type 1 and type 2 diabetes, whereas in type 2 diabetes it is also due to endothelium dependent NO synthesis impairment. [146] In the glabrous skin on the finger pulp on the other hand, no reduced vasodilative response is usually observed. [138,143] Other types of provocation protocols are also used to study the differences in blood flow between diabetics and controls, using LDF. These protocols involve ischemia, cold, and gravity (change of position). [138]

7   Model-based data processing

In Chapter 5 it was described how a moving RBC gives rise to a single Doppler shift, how the optical Doppler spectrum is built up from single Doppler shifts, and finally how the optical Doppler spectrum mixes on the detector giving the measured Doppler power spectrum. When processing the Doppler power spectrum, the aim is to produce something that is easy to present and that reflects the blood flow in the measured sample. In conventional LDF, such a measure is achieved by calculating the first moment of the Doppler power spectrum, as described in Section 5.3. However, this measure is given in arbitrary units that can not be related to physiological relevant units in any reliable manner. Furthermore, as also described in Section 5.3, it is non-linear, and the measurement volume is unknown and varies with for example the distribution of blood within the sampled tissue.

An alternative way to produce an LDF-measure is to first solve the inverse problem of fitting a model to the measured Doppler power spectrum, and then to present relevant data directly from the resulting model. Most effort during this thesis work has aimed at being able to do this. For a successful result, first of all a proper model has to be constructed, which has to be both physiologically (Chapter 6, [II]) and optically (Chapter 3, [II]) relevant. The model also has to be flexible and stable. From a given model with given model parameters, the Doppler power spectrum has to be calculated. In the method presented in this thesis, this has been solved by first simulating the light propagation in the model using Monte Carlo simulations (Chapter 4, [III]) and then calculating the Doppler power spectrum based on the detected light intensity and path length (Chapter 5, [I, V]). By comparing the measured and calculated Doppler power spectra, the model parameters are iteratively updated until an optimal fit between the spectra is achieved [V].

This chapter gives a description of the model-based quantitative LDF method that has been developed during the thesis work and that fulfills the aim of the thesis. A more compact and mathematical description of the method can be found in Paper V. The accuracy and limitations of the method are discussed in Chapter 9.

7.1   Measurement system

The measurement systems used in Papers I, II, V, and VI is a modified Periflux 5000 system (Perimed AB, Järfälla, Sweden) where the detector signal is divided into two parts; a fast time-varying ac signal that is achieved by band pass filtering the detector signal between 8 Hz and 15 kHz, and a slower dc signal via a low pass filter with cut off frequency of 32 Hz. Both the ac and the dc signals were sampled at 50 kHz. The Doppler power spectrum was given as the power spectral density of the ac signal, subtracted with the noise spectrum, dc^2 normalized, and normalized with the total power of a calibration measurement made in a microsphere solution (see Section 5.4.5 and Equation 5.42). The spectra were also compensated for the filter effects.

In Paper I, a single light collecting fiber placed 0.25 mm (center-to-center) away from the light emitting fiber was used, whereas additional fibers placed 1.2 mm away from the light emitting fiber were used in Papers II, V, and VI. In the latter case, two different sets of ac/dc signals were collected, one originating from the 0.25 mm fiber separation and one from the 1.2 mm separation. All fibers had a core diameter of 0.125 mm and a numerical aperture of 0.37. The laser source used was a 1 mW 780 nm diode laser.

7.2   Forward problem

Doppler power spectra at the same fiber separations that are used in the measurement system are calculated for a given set of model parameters in the forward problem. The model consists of three layers; the bloodless epidermis layer with variable thickness and two dermis layers where the first layer is 0.5 mm thick and the second has an infinite thickness. The two dermis layers contain various amounts of blood with various velocity distributions. The optical properties of the model layers and blood are given in Table 7.1.

Table 7.1 Optical properties of the tissue model at 780 nm.

Tissue type	n [-]	μ_a [mm^{-1}]	μ_s' [mm^{-1}]	μ_s [mm^{-1}]	g [-]
Epidermis [a]	1.40	0.4	3.5	23	0.85
Dermis	1.40	0.1	2.0	13	0.85
Blood [b]	1.40	0.43	2.0	222	0.991[c]

[a] 2% eumelanin

[b] 80% oxygenation level, 43% hematocrit, 145 g Hb/liter blood, 345 g Hb/liter RBC

[c] Gegenbauer kernel phase function with a_{Gk} = 1.0 and g_{Gk} = 0.948

The variable model parameters are expressed with six free parameters. The first parameter controls the epidermal thickness. The second and third parameters control the blood tissue fraction in the dermal layers (mean fraction and difference between the layers). The fourth and fifth parameters control the slope of the velocity distribution of the first dermal layer for low and high velocities, respectively. Finally, the sixth parameter controls the difference of the slopes of the velocity distribution between the dermis layers.

The tissue model is simulated for a number of epidermal thicknesses. For each of the simulations, path-length distributions and the detected intensities are stored (Figure 7.1). The path length distributions in the epidermal layer is divided into three parts, based on photons that have been propagating in the epidermis layer only, photons that have been propagating in the epidermis layer and the first dermis layer, and photons that have been propagating in all three layers, respectively. Likewise, the path length distribution in the first dermal layer is divided based on photons that have been propagating in all three layers or not. Thus, in total six path length distributions are stored. Similarly, the detected intensities are divided for photons that have been propagating only in the epidermis layer, only in the epidermis layer and the first dermis layer, or photons that have been propagating in all three layers, i.e. three intensities. Furthermore, these six path length distributions and three intensities are stored separately for the two source-fiber separations 0.25 and 1.2 mm.
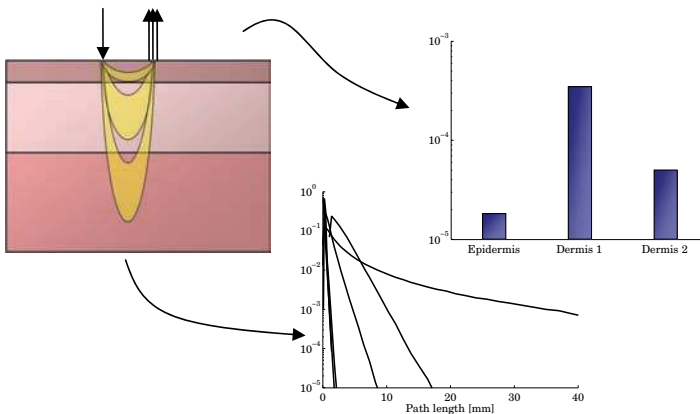

Figure 7.1 Path length distributions (lower) and intensities (right) are stored from base simulations (left), for each source-detector separation. Only data for the 0.25 mm separation are shown and three of the path length distributions are very similar.

When changing the blood tissue fraction in the dermal layers from the fractions used in the original simulations the path length distributions and intensities of the detected light are modified due to the difference in absorption between dermal tissue and blood (Figure 7.2). This modification is given by Beer-Lambert's law based on the path length distributions.
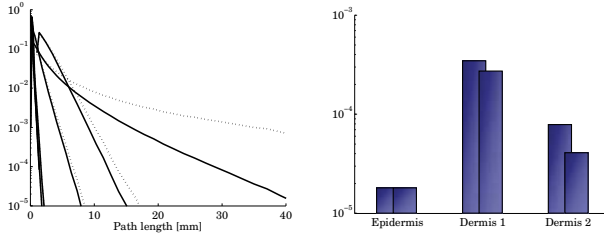

Figure 7.2 Modification of path length distributions and intensities.

The six modified path length distributions are translated into shift distributions, i.e. the number of Doppler shifts the photons have undergone during their propagation in each layer (Figure 7.3). Based on Beer-Lambert's law, it can be realized that the probability distribution of the number of shifts for a given path length, μ_s of blood, and blood tissue fraction follows a Poisson process (see also Equation 5.30). The total shift distribution in each layer therefore equals the sum of the Poisson processes over the path length distribution. For numerical reasons, it is convenient to calculate the Poisson distribution $Po(m)$ according to

$$Po(m) = \frac{(\mu e^{-\mu/m})^m}{m!} \tag{7.1}$$

instead of the normal form

$$Po(m) = \frac{\mu^m e^{-\mu}}{m!} \tag{7.2}$$

since μ^m may become very large. For large m, for example for $m > 50$, the factorial of m becomes very large, and then the Poisson distribution is better calculated using Stirling's formula [147] to approximate the factorial, which results in

$$Po(m) = \frac{(\mu e^{-\mu/m+1}/m)^m}{\sqrt{2\pi m}}. \tag{7.3}$$

In the Equations above, μ is the product of a given path length, the scattering coefficient of blood, and the blood tissue fraction, and m is the number of shifts.
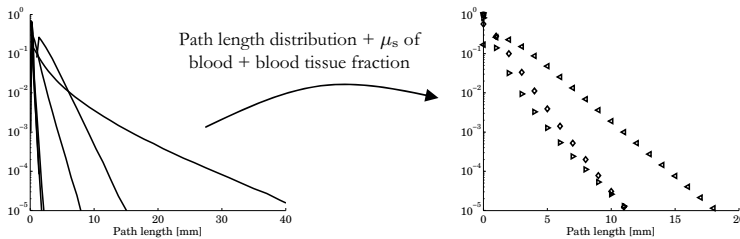

Figure 7.3 Translation from path length distribution to shift distribution. Note that three of the shift distributions are all zero shifts.

When the shift distribution in each layer is known the optical Doppler spectra in each layer can be calculated, still separated in six different optical spectra. This is done by successive cross correlations of the single shifted optical Doppler spectra in the layers

(Figure 7.4). The single shifted spectra are given from the velocity distribution in the layers and the phase function of blood assuming an isotropic angle distribution between the diffuse light and propagation of the RBC:s.
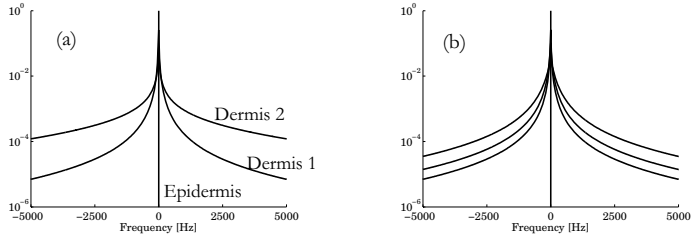

Figure 7.4a Single shifted optical spectra of epidermis and the two dermis layers.
b Optical Doppler spectra for 0, 1, 2, and 5 shifts, where 5 shifts corresponds to the widest spectrum (only spectra from dermis 1 are shown).

The total optical Doppler spectrum for each layer is then calculated by summation over each of the six shift distributions (Figure 7.5).
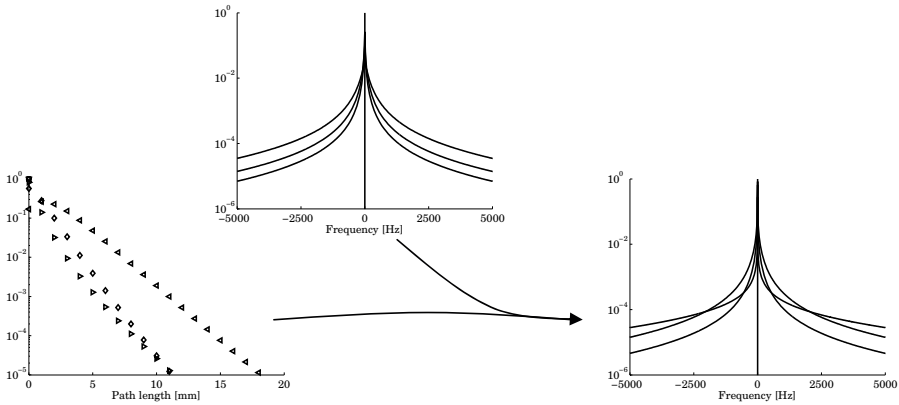

Figure 7.5 For each layer, the shift distribution is used to summarize optical spectra. This results in six spectra, three of them with 0 frequency only.

Now, the resulting six spectra are cross correlated with one another so that one spectrum (the zero frequency spectrum) corresponds to photons that only have been propagating in the epidermis layer, one spectrum corresponds to photons that have been propagating in epidermis and the first dermis layer, and one spectrum corresponds to photons that have been propagating in all three layers (Figure 7.6).
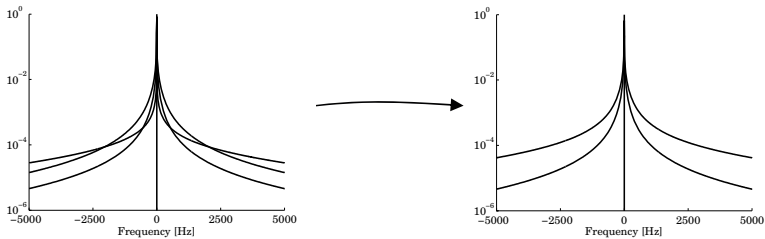

Figure 7.6 The six spectra are cross correlated into three spectra.

The resulting optical spectra is the summation of the three optical spectra from photons that have reached the three layers, respectively, using the three modified intensities normalized to unity (Figure 7.7).
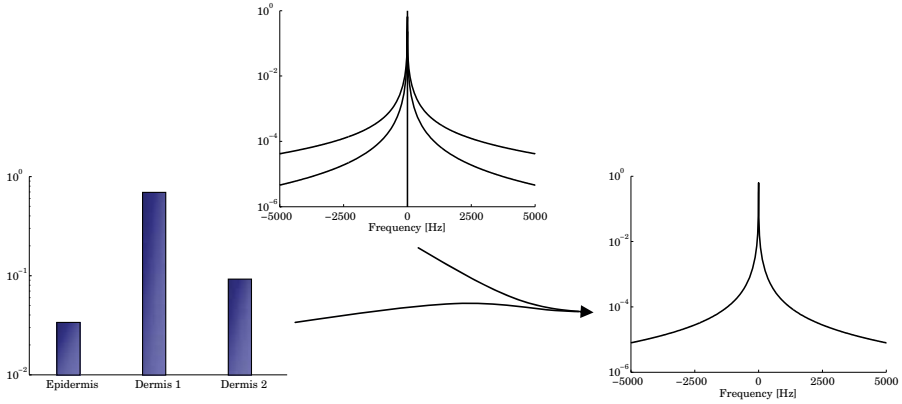
Figure 7.7 The intensities for photons that have been propagating down to each layer are used to summarize the optical spectra corresponding to these photons.

Finally, what the detector registers is the beating of the light that impinges the detector, which is the difference between frequencies in the optical spectrum. The Doppler power spectrum is thus calculated as the auto-correlation of the optical Doppler spectrum (Equation 5.27, Figure 7.8). A comparison between Monte Carlo simulated spectra, where the optical spectra are built from the cumulative Doppler shift of each photon, and calculated (forward problem) spectra is found in Figure 7.9.

Figure 7.8 The final optical Doppler spectrum is auto correlated to give the Doppler power spectrum

Figure 7.9 Comparison between simulated (thick, rough) and calculated (thin, smooth) Doppler power spectra at the two different source-detector separations 0.25 mm (below) and 1.2 mm (above). [V]
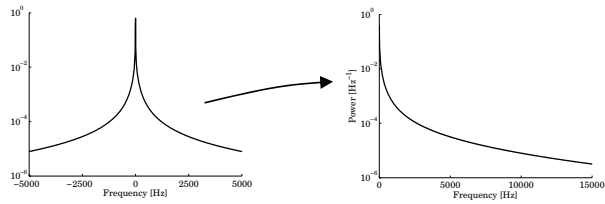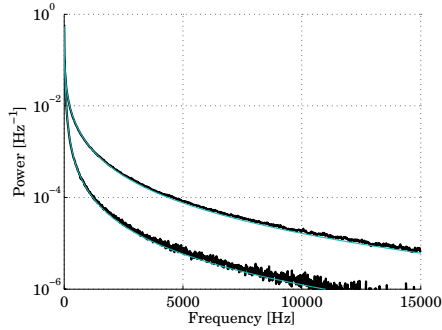
7.3   Nonlinear optimization

As mentioned in the last section, the six free model parameters are iteratively updated until the measured and calculated Doppler power spectra agree. The difference between the spectra, i.e. the χ^2 error function, is calculated by subtracting the logarithm of the spectra at 32 averaged frequency bins. The averaged frequency bins are calculated as the average power for frequencies that surround the bins. They are close one another at low frequencies and sparser at higher frequencies. In this manner, changes in any of the six parameters have approximately the same influence on the difference, and the difference is not influenced by noise. For details, see Paper V.

The widely used Levenberg-Marquardt method is used to update the free model parameters in each iteration. Very briefly, the Levenberg-Marquardt method searches in the steepest descent direction of χ^2 far from the minimum, and as the minimum is approached, it searches more and more in the direction to the minimum of a local quadratic model of the χ^2 function. [148]

The Levenberg-Marquardt method does not ensure global convergence but can be trapped in a local minimum. Therefore, another strategy must be used to increase the probability that the minimum found is in fact the global minimum. Many strategies may be used for this [149], and here a combination of two intuitive methods, pure random point and multiple start, is used. The method randomly chooses a starting point within certain boundaries, and when the χ^2 error is low enough in this point, it is used as a starting point for the Levenberg-Marquardt method. It is ensured that the starting points are widely separated from each other, and when the same minimum point is found from three different starting points, it is assumed that the global minimum is found.

7.4   Model output

When the best fit model is found it is an easy task to present any desired data from it. It is proposed in Paper V that the presented data is the perfusion measured in g RBC / 100 g tissue × mm/s, divided into three velocity regions; below 1 mm/s, 1-10 mm/s, and above 10 mm/s, in a volume of a 3 mm^3 half sphere, i.e. within a radius of 1.13 mm from the light emitting fiber. The robustness of this velocity resolved perfusion measure was evaluated in Paper V. It was concluded that the robustness was at least as good as for the conventional perfusion measure at the 1.2 mm fiber separation, and better than for the perfusion measure at 0.25 mm – the standard fiber separation used by leading LDF

manufacturers. Furthermore it lacks the non-linear behavior that is found in conventional LDF, especially at high RBC tissue fractions and large fiber separations.

In theory, any other parameters such as the epidermis thickness or the depth resolved perfusion can also be presented from the model. However, the robustness of such measures has not been evaluated and should be interpreted with the greatest caution, as the input data to the model is not designed to handle this. To be able to give such measures with good precision, more data are needed as input for the model optimization process and the model has to be more flexible. The same is true for a higher velocity resolution.

The separation of the perfusion measure into three velocity regions may facilitate the physiological interpretation of the perfusion. For example the high velocity region may be related to flow in large vessels whereas the low velocity region may be related to capillary flow, although also the blood flow velocity in veins is low in some situations. This offers a great advantage compared to conventional LDF in clinical use, as does the use of a physiologically relevant unit and a constant and predetermined output volume.

An example of the new absolute velocity resolved perfusion measure in the 3 mm^3 volume is shown in Figure 7.10. The figure shows the perfusion in the skin of the dorsal side of the foot during a heat provocation to 44 ºC, and is an example from the study in Paper VI.
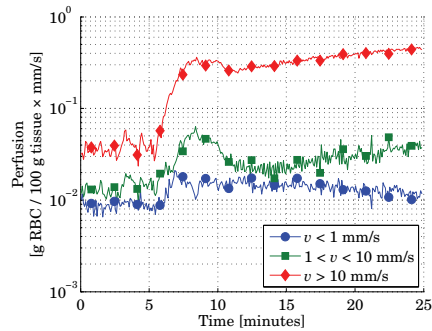

Figure 7.10 Example of the velocity resolved quantitative perfusion estimate during a heat provocation to 44ºC (from 5 minutes). [VI]

8 Review of the papers

The papers presented in this thesis show the methodological progress from *in vitro* models to clinical measurements. In short, Paper I demonstrates the principle of how multiple Doppler shifted spectra can be decomposed into relative amounts of flow in three different flow velocity regions. This was done in an *in vitro* flow model. A six-layered microcirculatory skin model is presented in Paper II. That model is the foundation for being able to extract the absolute units in the method that is presented in Paper V. Paper III presents a Monte Carlo variance reduction technique that can be used to simulate LDPI setups. That method was used in Paper IV, where the measurement depth and volume for various LDF setups and human tissues were investigated. The measurement depth and volume for various variants of the skin model from Paper II were, for example, evaluated there. The final method, which is presented in Chapter 7, was presented in Paper V. Many ideas and results from Papers I, II and IV were used in this paper. Finally, the method presented in Paper V was used in a clinical study on type 2 diabetics which is presented in Paper VI.

Short reviews of each of these six papers are given in the sections below.

8.1 Paper I

In the first study in this thesis, entitled "Absolute flow velocity components in laser Doppler flowmetry", the aim was to show that it is possible to decompose laser Doppler spectra, also with a high degree of multiple shifted photons, so that the flow is divided into three different velocity regions. It is a study performed on an *in vitro* model, consisting of plastic tubes (0.5 mm inner diameter) wrapped around a piece of white plastic in two layers and perfused with various concentrations of both polystyrene microspheres and human blood. The flow velocity in the tubes was controlled with a precision syringe pump.

Equations were presented to calculate a Doppler power spectrum based on three different velocity components, i.e. blood concentrations in the three different velocity regions. In the calculations, single shifted spectra for each of these velocity components were given by a simple Monte Carlo simulation based on the velocity distribution of the velocity component, the scattering phase function of the moving particles, and the assumption of a random angle between the direction of the photons and the moving particles. The single shifted spectra were combined and a multiple shifted spectrum was calculated by successive cross-correlations weighted with the shift distribution over the number of Doppler shifts the photons had undergone. This shift distribution was given by a Monte Carlo simulation of the flow model for the given concentration of the moving scatterer. The Doppler power spectrum was finally calculated by the cross correlation of the multiple shifted spectrum. It was also presented how these calculations could be made more efficient using the Fourier transform, avoiding the time-consuming cross correlations. The concentrations of each of the three velocity components were found using the non-linear Levenberg-Marquardt method to minimize the difference between the measured and simulated spectra in a least square manner.

The method worked well for low concentrations of moving particles, although a small underestimation of the mean velocity was generally observed. For higher concentrations of the moving particles, the underestimation was larger, especially for undiluted human blood. For the polystyrene spheres, the underestimated mean velocity was foremost due to subsequent Doppler shifts that tend to have opposite signs in the measurements, while it was assumed in the calculations that the signs were random. This effect resulted from the low anisotropy factor of the spheres combined with the relatively large diameter of the

tube. For the blood, on the other hand, the effect was probably foremost due to that most of the shifts took place in the periphery of the tubes where, because of the assumed parabolic flow profile, the velocity was lower. Another explanation as to why the mean velocity was underestimated for undiluted blood, not discussed in the paper, is that the anisotropy of undiluted blood was underestimated. The reason for this is that the scattering phase function of blood in that paper was estimated from a measurement on 0.1% blood diluted in physiological saline, that have a significantly lower refractive index than blood plasma which leads to a lower anisotropy factor. The anisotropy factor estimated in this paper was much lower ($1 - g$ differed 33%) than the anisotropy factor estimated in [II], where the blood was diluted using blood plasma (anisotropy factor of 0.988 compared with 0.991).

It was concluded that it is possible to accurately decompose three different flow velocity components from a Doppler power spectrum composed of a high degree of Doppler shifts. Some of the obstacles with the method originated from the high heterogeneity and large tube diameter in the flow model, which is less of a problem in living tissue. Thus, although using the method *in vivo* offers up many other obstacles, the study was a promising step towards a method for quantitative laser Doppler flowmetry.

8.2   Paper II

One of the steps in the method presented in [I] was to simulate the flow model for each concentration of moving scatterers to get the shift distribution. A similar method for *in vivo* skin measurements must in analogy be based on a valid skin model. Therefore, the aim of the second study was to present a flexible skin model with geometrical and optical (at 780 nm) properties based on the literature.

The resulting skin model consists of six layers (see Figure 6.1). The top layer is the bloodless epidermis layer that contains light absorbing melanin. The dermis is divided into four layers. First the papillary dermis at the border between the epidermis and the dermis that contains capillaries but no other vessels. Then follows the superior blood net dermis which is a thin layer with a high vessel density, containing foremost arteries, capillaries, and venules. The main part of the dermis is called the reticular dermis and contains sparsely distributed vessels. The deepest part of the dermis at the border to the subcutis, the inferior blood net, contains many blood vessels that support the skin layers above. A few larger blood vessels are situated in the deepest layer, the subcutis. The optical properties of the skin model layers and blood are presented in Table 8.1.

Table 8.1 Optical properties of bloodless skin layers and blood at 780 nm. Dermis reaches from the papillary dermis to the deep blood net. Note that the refractive index n is set to 1.40 to avoid Fresnel reflections at the distinct borders between the layers.

Tissue type	n [-]	μ_a [mm^{-1}]	μ_s' [mm^{-1}]	μ_s [mm^{-1}]	g [-]
Epidermis	1.40	0.4	3.5	23	0.85
Dermis	1.40	0.1	2.0	13	0.85
Subcutis	1.40	0.1	2.0	13	0.85
Blood	1.40	0.5	2.0	222	0.991[a]

[a] A Gegenbauer kernel phase function with $\alpha_{Gk} = 1.0$ and $g_{Gk} = 0.948$.

The thickness (same scaling factor for all layers) and blood tissue fractions (concentrations) at three different flow velocities could be altered from the standard model. The values for the standard model are given in Table 8.2, where it can be seen that the relative tissue fraction of high velocity components generally increases with depth. All velocity components were evenly distributed between 0 and twice the mean velocity (0.3, 3.0, and 30 mm/s, respectively).

Table 8.2 Thickness t and blood tissue fraction of the three different blood flow velocities for the six layers in the standard skin model.

Tissue type	t [mm]	Blood tissue fraction [%]		
		0.3 mm/s	3.0 mm/s	30 mm/s
Epidermis	0.075	0	0	0
Papillary dermis	0.15	0.2	0	0
Superior blood net dermis	0.15	0.6	0.05	0.001
Reticular dermis	0.80	0.1	0.01	0.0006
Inferior blood net dermis	0.40	0.25	0.035	0.006
Subcutis	10	0.1	0.01	0.001

Simulations were run for a large number of variations of the standard skin model, where the thickness t was varied with factors of 2^{-2}, 2^{-1}, …, 2^{2}, the blood concentrations of velocity components 0.3 and 3.0 mm/s with factors of 2^{-3}, 2^{-2}, …, 2^{6}, and the velocity component 30 mm/s with the factors 2^{-3}, 2^{-2}, …, 2^{10}. All layers were changed with the same factor.

To test the validity of the skin model, the Doppler power spectra from the simulations were fitted to measured spectra for measurements on finger and forearm. Spectra at two different source-detector separations (0.25 and 1.2 mm) were fitted simultaneously, increasing the robustness of the procedure. During the forearm measurements, the skin was also heated to 44 °C. Examples of the spectral fit during the forearm measurements are shown in Figure 8.1.
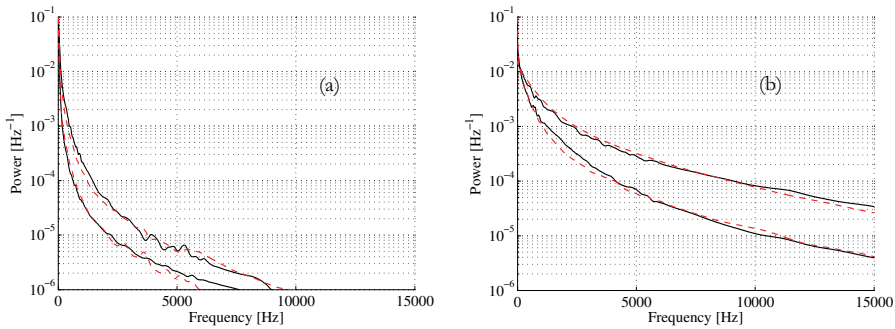

Figure 8.1 Examples of spectral fit between measured spectra (solid lines) and fitted simulated spectra (dashed lines). The higher spectra originate from the larger fiber separation (1.2 mm), whereas the lower spectra originate from the 0.25 mm fiber separation. In (a), spectra from a baseline measurement on the forearm are shown, whereas spectra at the end of the heat provocation are shown in (b).

The blood concentrations of the fitted models were consistent with *a priori* expectations; the concentration was higher on finger pulp that on forearm, the concentration increased drastically during heating, and the heating affected the high velocity component more than the low one. The results indicate that the model is valid.

8.3 Paper III

In many bio-optical setups, an extremely small part of the total light is detected. This is for example true when the detector size or acceptance angle is small, as in many imaging systems, including laser Doppler perfusion imaging. Simulating such setups is normally exceptionally time-consuming. A variance reducing method that works well for such setups is forced detection and that method is presented in paper III. The method, which has previously been extensively used in Monte Carlo simulations within the fields of atmospheric optics, nuclear and particle physics, and radiology, is demonstrated in detail for imaging simulations of blood vessels in that paper.

The principle is to force a fraction of the photon to the detector at each and every scattering event. The fraction forced to the detector equals the probability that it will reach the detector without any further interaction with the medium. That probability depends on the detector geometry, the scattering phase function, the scattering and absorption coefficients, and the refractive index. The rest of the photon continues its random walk but is not allowed to reach the detector by random walk. The principle is graphically shown in Figure 8.2.
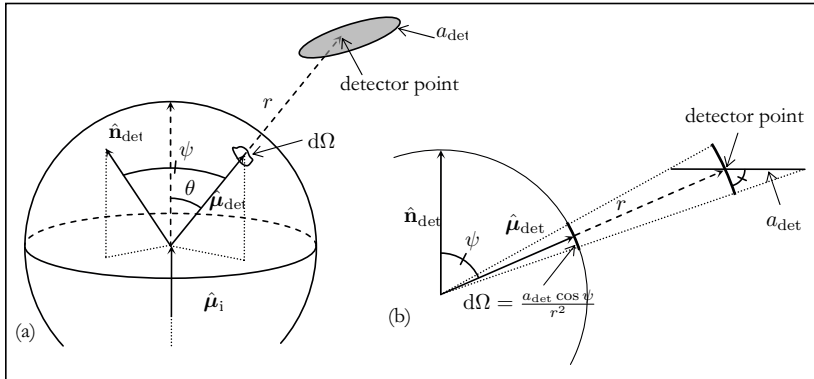

Figure 8.2 a) Incident photon with a direction $\hat{\boldsymbol{\mu}}_i$ is scattered in the center of the unit sphere. The forced part of the photon is directed $\hat{\boldsymbol{\mu}}_{det}$ towards the detector a_{det} located at a distance r.
b) Cross section where the plane spanned by $\hat{\mathbf{n}}_{det}$ and $\hat{\boldsymbol{\mu}}_{det}$ intersects the unit sphere in a).
Reprinted from [III], with permission.

Two slightly different methods were presented, one that is efficient when the detector is small and one that is efficient when the detector has a small acceptance angle. Unfortunately, the methods are limited to refractive index matched models, but it was discussed how refractive index mismatches can be corrected for in some situations. It was evaluated and discussed during what circumstances the methods are valid, and it was discussed in what situations the methods are expected to be efficient.

Two examples were presented in the article. In those examples, two blood vessels of different size and position were placed in a dermis tissue and the optical properties of dermis and blood were valid at 543 nm. This setup was simulated both simulating a normal camera system and simulating a telecentric lens system. The first method was used with the first setup and the second method with the second setup. When using the forced detection technique with these two setups, the simulation was accelerated two orders of magnitude using forced detection, compared to normal brute force simulations. The results can be seen in Figure 8.3, where it can be seen that less light is detected over the blood vessels due to the higher absorption in blood relative to the surrounding medium.
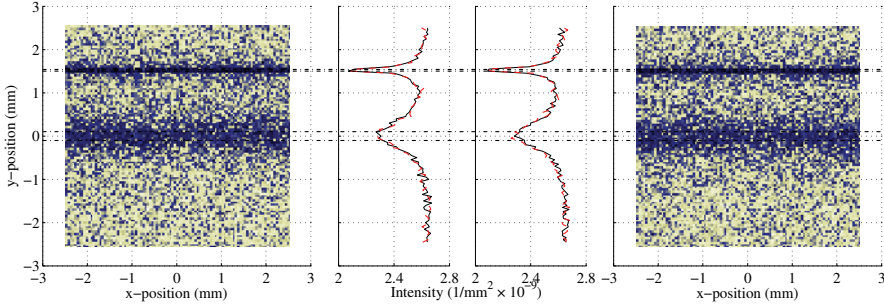
Figure 8.3 The generated images from the FD algorithm of setup I (left) and of setup II (right), and the average intensity over the x axis for both setups and for both forced detection and brute force simulations (middle). The true borders of the blood vessels are marked with the dash-dotted lines. Reprinted from [III], with permission.

8.4   Paper IV

To be able to draw correct physiological conclusions from LDF measurements, it is important to know the measurement depth or volume of the system. It is also important to know how various system parameters and physiological parameters affect the measurement depth or volume. This was studied in [IV], where the measurement depth and volume was calculated using Monte Carlo simulations of various system setups and tissue models. This has previously been done in Reference [150], but this paper differs from that study in that the models are more relevant, multiple Doppler shifts are handled correctly, and non-linear speckle effects are accounted for in the LDPI setups (see Section 5.5.1).

When calculating the measurement depth and volume, the position and signal contribution of each Doppler shift was evaluated. The signal contribution $s_{m,n}$ takes into account the weight w_m of photon m and the size $d_{m,n}$ of Doppler shift n in relation to all other Doppler shifts of the photon, as

$$s_{m,n} = w_m \frac{|d_{m,n}|}{\sum\limits_{k=1}^{K_m} |d_{m,k}|} \left| \sum_{k=1}^{K_m} d_{m,k} \right|, \tag{8.1}$$

where K_m is the total number of Doppler shifts for the photon. In this manner, multiple shifted photons were accounted for.

The measurement depth was set at the depth above which $1 - e^{-1} \approx 63\%$ of the signal contributions originated. In analogy, the output volume was set to the volume of a half sphere within which 63% of the signal contribution originated. This definition has more in common with the "look-ahead distance" introduced by Qian *et al.* [151] than the measurement depth as defined by Jakobsson and Nilsson [150], as it is related to the positions of signal contributions rather than where the light has been propagating. An example of the signal contributions and the resulting measurement depth is shown in Figure 8.4.
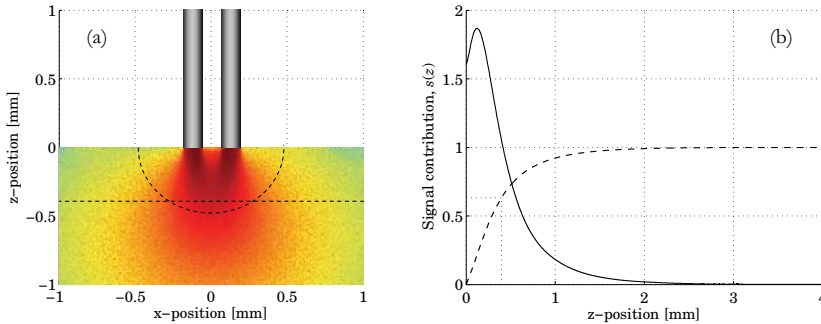
Figure 8.4 Example of the signal contribution s as a function of position (a) and depth (right, solid line) and the cumulative sum of the signal contribution (b, dashed line). The measurement depth at 63% of the total signal contribution is marked in both figures, and the measurement volume is marked in the left. The intensity scale in the left figure is logarithmic. Reprinted from [IV], with permission.

The general conclusions were, with some exceptions presented in the paper:

- The measurement depth/volume increases with source-detector separation in LDPM setups.
- The measurement depth/volume increases with beam diameter in LDPI setups.
- The measurement depth/volume is larger for 633 nm than for 543 nm, and larger for 780 nm than for 633 nm.
- An increased RBC tissue fraction reduces the measurement depth/volume, also at low fractions.
- The blood oxygen saturation affects the measurement depth/volume to a minor extent, particularly little at 543 and 780 nm.
- An increase of the tissue absorption and/or scattering reduces the measurement depth/volume.
- An increase of high velocity blood flow in deep skin layers increases the measurement depth/volume.
- Melanin tissue fraction in the epidermis has a negligible effect on the measurement depth/volume.

The following examples of measurement depths are given for an LDPM system with 0.25 mm source-detector separation and an LDPI system with a 0.5 mm beam diameter, respectively, both operating at 780 nm: muscle – 0.55/0.79 mm; liver – 0.40/0.53 mm; gray matter – 0.48/0.68 mm; white matter – 0.20/0.20 mm; index finger pulp – 0.41/0.53 mm; forearm skin – 0.53/0.56 mm; heat provoked forearm skin – 0.66/0.67 mm. All evaluated measurement depths were below 1.0 mm.

8.5   Paper V

The method for quantitative laser Doppler flowmetry, which is based on a model adaption to measured Doppler power spectra, is described in Paper V. This work describes in-detail the forward problem, the reverse problem, and how to attain output data from the model.

Briefly, the forward problem describes how to calculate the Doppler power spectra for a given set of model parameters. This is done via Monte Carlo simulated path length distributions from a small number of three-layer skin models with different layer thicknesses. Based on this data, shift distributions that displays how many times the photons are Doppler shifted before detection, are calculated. These shift distributions are used to combine single shifted optical Doppler spectra into multiple shifted optical Doppler spectra for the different layers in the model. The single shifted optical Doppler spectra are given by the scattering phase function of blood and the velocity distribution

that is controlled by some of the model parameters. The multiple shifted optical Doppler spectra from the different layers are then combined into a single Doppler power spectrum that can be compared to the measured spectra for each fiber separation.

Using the Levenberg-Marquardt method, the model parameters are iteratively updated until an optimal fit is found between the calculated and measured spectra at both fiber separations. The method description given in this paper is a more mathematically thorough description than the one given in Chapter 7 in the thesis. It also describes how the forward problem can be calculated faster using the Fourier transform.

Apart from the method description, a comprehensive robustness analysis of the method was performed for simulated models that could generally not be exactly described by the three-layered model used in the method. It was concluded that the method had a robustness superior to conventional LDF, and that the method output was only affected to a low extent by the optical properties of the static media and the absorption coefficient of blood. As expected, it was affected to a larger extent by variations in the scattering properties of blood. Moreover, it was shown that the introduction of heterogeneities in form of discrete capillaries, hair follicles, and sweat glands had a negligible impact on the results. Larger vessels on the other hand can introduce heterogeneities that the model cannot handle, which is manifested by a large error in the spectral fit. That error can thus be used to exclude uncertain perfusion estimates, which is an advantage to conventional LDF.

The method was also tested on a measurement during a local heat provocation of forearm skin. The results showed that the increased blood flow, caused by the provocation, occurred foremost in the high velocity regions above 1 mm/s.

8.6   Paper VI

In the last paper, microcirculatory changes in diabetes type 2 were studied using the quantitative LDF method. The velocity resolved perfusion estimate was compared for patients with diabetes type 2 with age-matched non-diabetic controls, during baseline and heat provocation of the dorsal side of the foot.

As in the example measurement in Paper V, it was shown that the increased blood flow that results from local warming is an effect that involves blood flow velocities above 1 mm/s, which indicates that it does not affect the nutritive capillary flow but foremost larger vessels and arteriovenous (AV) shunt flow. Although this was expected, it has not been shown using conventional LDF, which lacks the ability of differentiating between blood flow velocities.

The heat response in the diabetes subjects was significantly lower than in the non-diabetic controls, both in the initial response a few minutes after the heat onset and in the late plateau 15-20 minutes after the onset. That indicates that both the fast C-fiber axon reflex and the slower NO-dependent response (see Section 6.2.1) is impaired in diabetes type 2, which has previously been shown using conventional LDF. The results in this study showed that the differences could be seen for high velocities and not for velocities below 1 mm/s.

In Figure 8.5, the perfusion in the low and intermediate velocity regions is plotted versus the diabetes duration. In both cases, a significant ($p < 0.05$) correlation was found, but interestingly, the relation was opposite for the two regions. Normalizing the perfusion in the low velocity region with the intermediate region further increased the significance ($p < 0.01$). Others have previously shown that the AV shunt flow may be increased in diabetes during baseline conditions, at the expense of the nutritive capillary flow. [142] This is found especially in patients with severe neuropathy, but also in patients without further complications. Using conventional LDF, it has previously been shown that the baseline perfusion may be increased in diabetics indicating an increased AV shunt flow. Due to the ability of the quantitative LDF to differentiate the perfusion into various velocity regions,

this is the first time the use of LDF has indicated a reduced nutritive capillary flow in diabetes, a conclusion that is made possible by relating the low velocity region to capillary flow.
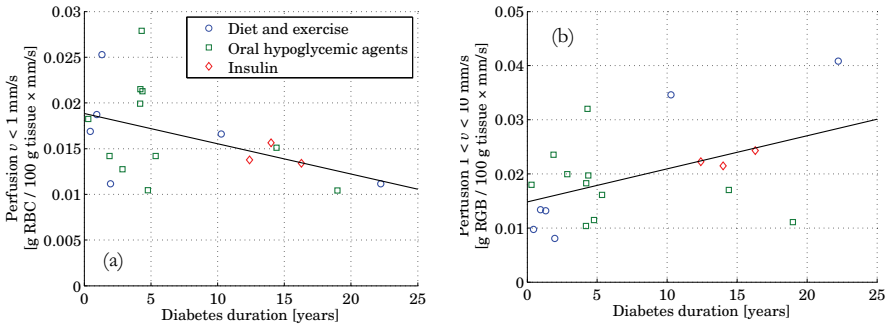

Figure 8.5 Relation between the perfusion in the low velocity region (below 1 mm/s, a), and the intermediate velocity region (between 1 and 10 mm/s, b), respectively, and diabetes duration.

9   Discussion

The quantitative LDF method is discussed in the following subsections, especially in contrast to the conventional LDF method. Since LDF is an established method, its uniqueness and the elegancy of the analysis model presented by Bonner and Nossal [8] are not discussed here. Rather, the limitations of the conventional method and how these are treated by the quantitative method are discussed, as well as the potential limitations and possibilities of using the quantitative method.

9.1   Conventional LDF limitations

The conventional LDF method has been accompanied with a number of limitations and/or question marks. These include: the influence of the tissue optical properties; unknown and non-constant measurement volume; arbitrary units and relative measurements only; no flow velocity determination and differentiation; non-linearities due to multiple Doppler shifts; motion artifacts; and the effect of other moving particles in the tissue. [20] These limitations and their relation to quantitative LDF are discussed in this section.

The effect of changing the optical properties of both the static media and blood on both the conventional perfusion estimates (see also reference [108]), the measurement volume of the conventional perfusion estimates, and on the quantitative perfusion estimates, has been evaluated in Papers II, IV, and V, respectively. In Paper V, it was concluded that the effect was in principle negligible for values relevant for skin for the quantitative LDF method. The quantitative LDF method can easily be adapted to other types of tissue, where the optical properties of the static tissue are substantially different from skin. Thus, by modifying the properties of the model, the quantitative LDF method is general for all types of tissue. However, the method may benefit from a layer structure that is adapted to the tissue under consideration. For example in a homogeneous tissue without layers, the model adaption may be better if the model is a single-layer model, although the three-layer model in V, can in principle handle homogeneous tissue.

In conventional LDF, the measurement volume is unknown and changes both with system setup, optical properties, and with the blood flow itself. [IV] In the quantitative LDF method, the output volume is not only constant, but also geometrically defined as a half sphere with the volume of 3 mm^3, i.e. a 1.13 mm radius from the light emitting fiber. Although the output volume is arbitrarily defined and the quantitative perfusion estimate is affected by the flow outside this volume to some extent, which has been evaluated in Paper V, the constant volume offers a great advantage compared to conventional LDF for both the physiological interpretation of the results and when comparing different measurements. Furthermore, the perfusion will change due to the change in measurement volume alone in conventional LDF when the blood flow distribution is changed, which is probably the main reason that the robustness of the conventional LDF is considerably lower than for the quantitative LDF method, as evaluated in Paper V.

One of the main aims in this thesis was that the developed method should present the perfusion estimate in a physiologically relevant unit, in contrast to the arbitrary units used in conventional LDF. With the new method, RBC tissue fractions are presented in g RBC/100 g tissue, velocities in mm/s, and perfusions in g RBC/100 g tissue × mm/s. It is likely that this facilitates the physiological interpretation of the results. This, however, remains to be shown in further clinical studies.

In the theoretical model of LDF presented by Bonner and Nossal [8] an assumption is made that single Doppler shifts are dominant. This assumption is unfortunately not valid

even for small source-detector separations at moderate blood tissue fractions, and becomes even worse for increased source-detector separations or higher blood tissue fractions. In Figure 9.1, the fraction of multiple shifted photons, relative to all shifted photons, for photons detected at 0.25 and 1.2 mm source-detector separations, is plotted versus the blood tissue fraction. The data is based on a model with a 0.075 mm epidermis layer and an infinite dermis layer, with the given blood tissue fractions and hematocrit of 43% giving $\mu_s = 222$ mm^{-1}. The effect of the multiple Doppler shifts is a non-linearity in the conventional perfusion estimate (Figure 5.4b). In an early attempt to compensate for this, Nilsson developed a method that based on the CMBC estimate adjusted the perfusion signal. [9] However, in LDF systems the CMBC estimate is not very reliable and quickly becomes saturated when the blood tissue fraction increases. Furthermore, the method was evaluated on plastic flow phantoms, and even though the response in *in vivo* measurements followed the expected pattern, it has not been proven that the adjustment is correct. Other studies have also identified a number of weaknesses with the simple approach. [152,153] In the quantitative LDF method, the multiple Doppler shifts are a part of the forward problem, and the non-linearity introduced by multiple shifted photons is therefore not present in this method. This was shown in Paper V.
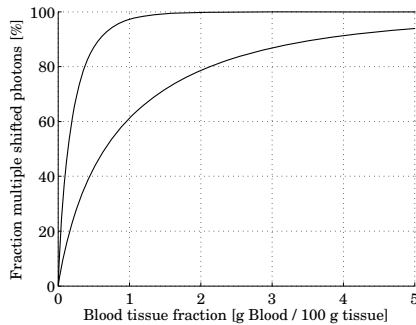

Figure 9.1 Fraction of all detected Doppler shifted photons that are multiple Doppler shifted as a function of blood tissue fraction in dermis which is located below a 0.075 mm thick epidermis layer. The fraction is shown for two source-detector separations, 0.25 (lower) and 1.2 mm (upper).

By normalizing the conventional perfusion measure with the CMBC-signal, i.e. the zero order moment of the Doppler power spectrum, a measure related to the RMS velocity is achieved. [8] However, due to the highly non-linear behavior of the CMBC (Figure 5.4a) and its saturation at moderate to high blood tissue fractions, the velocity estimate also becomes uncertain. Furthermore, this is only an estimate of the RMS velocity (in an arbitrary unit) and not the distribution of velocities. Studies with higher order moments have been presented, where foremost high velocity flows could be separated. [154,155] Still, this gives no information about the absolute velocities and it is therefore difficult to draw any conclusions based on this velocity estimate. The proposed quantitative LDF method not only separates the perfusion into three velocity regions, but also gives the absolute borders between the regions in mm/s.

Movement artifacts are sometimes a problem in LDF, both that tissue movements affect the Doppler power spectrum, and in LDPI where the acquisition times are long, that tissue movements introduce image distortions. In LDPM, movements of the optical fibers may also affect the Doppler power spectrum. For LDPI, the problem of image distortion is reduced with the fast CMOS-based imaging systems. Furthermore, cross polarized filters can reduce the movement artifacts on the Doppler power spectrum in LDPI [156], and the use of an integrated probe may reduce the movement artifacts in LDPM [110]. The thesis by Karlsson treats the problem of movement artifacts thoroughly. [114] Movement

artifacts are not specially treated in the quantitative LDF method, apart from that severe artifacts may lead to a poor model adaption and exclusion of the measurement.

It is generally assumed that only RBC:s influence the LDF signal. The blood consists of other scattering particles as well though – proteins in the plasma, platelets, and white blood cells (leukocytes). According to [157], the proteins in the plasma scatters in the Rayleigh regime, which generally results in large scattering angles and thus large Doppler shifts (Equation 4.13). However, the probability of scattering by a protein compared to the probability of scattering by an RBC is only about 1/50,000 [157]. The platelets are almost as forward scattering as RBC:s, but the scattering coefficient of platelets in blood is only about 1/1,000 of the scattering coefficient of RBC:s [157]. Finally, white blood cells are extremely weak scatterers [157]. In conclusion, the influence of other blood constitutes than RBC:s can be neglected. The effect of other moving structures in the tissue, such as the movement of vessel walls, may have a small influence, however.

9.2   Model assumptions

As described in Section 5.5, it has frequently been shown that MC simulations may be used to produce accurate Doppler power spectra. The simulations in this thesis do not deal with the polarization direction of the light, which could theoretically affect the results since light with different polarization directions does not interfere. However, the light emitted from the fiber in an LDPM system is unpolarized and it can therefore be assumed that both polarization directions carry the same information. Furthermore, even if the optical fiber would conserve the polarization from the laser source, light quickly loses its polarization through dermis (almost entirely after 10 mean free path lengths [158]), so the detected Doppler shifted light even in the close source-detector separation of 0.25 mm would in principle be unpolarized. In LDPI on the other hand, crossed polarization filters can be used to remove specular reflections which strongly affect the dc-signal. [156]

A number of assumptions and simplifications are always made when modeling the reality and this is of course also true for the Monte Carlo models used in this thesis. One very common assumption in Monte Carlo simulations of tissue is that the tissue is homogeneous, for example that the blood is homogeneously distributed. The effect of this has been studied by Talsma *et al.* [159] who suggested the use of "apparent" optical properties. The effect may be completely different in different measurement situations, and was partly evaluated for quantitative LDF in Paper V. However, this may require more attention in future studies.

In the layered models used in this thesis, for example in Papers II and V, the borders between the layers are perfectly flat and distinct, which is a simplification. Meglinsky and Matcher proposed a method to model the wavy borders between the various skin layers for more correct simulation results. [52] It seems, however, as if neglecting the differences in refractive index between the layers has a similar effect as the wavy model, and since refractive index matched flat borders substantially reduces the complexity of the model, that strategy has been used throughout most of the simulations in this thesis. Furthermore, as the forced detection method presented in Paper III can not handle refractive index mismatches within the medium, this is an attractive solution.

Most often in Monte Carlo simulations, the medium is assumed to be isotropic, i.e. the optical properties are not dependent on the direction of the light propagation but only on the position. This is not true for all types of tissue though, for example not for dentin and muscle tissue. The effect can be severe but can also be accounted for in the Monte Carlo software. [89,160] No such considerations have been taken in the simulations in this thesis, but in skin especially the epidermis is slightly anisotropic, which however probably has a minor impact on the results.

Light scattering in RBC:s was modeled using a Gegenbauer kernel phase function with $\alpha_{Gk} = 1.0$ and $g_{Gk} = 0.948$ resulting in an anisotropy factor $g = 0.991$ in Papers II and

IV-VI at 780 nm. This differs slightly from the phase function used in Paper I, which had the same α_{Gk} but with $g_{Gk} = 0.937$ results in $g = 0.988$. The reason for this deviation is that when estimating the scattering phase function in Paper I, a saline solution was used instead of blood plasma to dilute the RBC:s. Since the saline solution has a somewhat lower refractive index than blood plasma, the result was a more isotropic scattering phase function, i.e. a slightly lower anisotropy factor which can also be foreseen with Mie theory.

In both Papers I and II, the phase function of blood was determined using a low concentration of RBC:s and at a low velocity. RBC:s tend to migrate toward the center of the tube at higher shear rates [161-163], and the tube would have been unevenly probed at higher concentrations due to absorption. Therefore, for correct results, the measurements were performed at low concentrations and velocities.

The Gegenbauer kernel phase function was developed to describe the scattering phase function for highly anisotropic particles, where RBC:s and other blood components were taken as examples in the original article. [58] It can also be seen in Figure 3.2 that the Gegenbauer kernel phase function in Paper II resembles the shape of the Mie phase function of an RBC equivalent Mie sphere much better than the Henyey-Greenstein phase function with the same anisotropy factor. The anisotropy factor of the phase function presented in Paper II is in good agreement with values presented by others. [163,164]

A constant scattering phase function of blood in the tissue is assumed in the skin models in the thesis. It is however known that the RBC shape and formation may affect the phase function, and it is not unlikely that it can also be affected by the vessel wall when squeezed through a capillary. Enejder (formerly Nilsson) *et al.* have performed calculations on the effect of this. [164,165] According to their calculations, the effect is about ±30% in the extreme cases for $1 - g$. In Paper V, the effect on the quantitative perfusion estimate of changing the anisotropy factor corresponding to a change in $1 - g$ of ±40% was evaluated. The effect of this was less than 40%, and since it is unlikely that the phase functions of all RBC:s in the probed tissue are changed to the same extreme, the effect of RBC shape and formation on the quantitative perfusion estimate is probably minor.

A potentially greater effect on the quantitative LDF method related to the scattering phase function is the fact that the apparent phase function of blood from the detected photons is sometimes lower than 0.991. The apparent phase function is the actual distribution of scattering angles for the detected photons. In Figure 9.2, the distributions of scattering angles from photons detected in the close detection fiber (0.25 mm) are plotted, as well as the Gegenbauer kernel phase function with $\alpha_{Gk} = 1.0$, $g_{Gk} = 0.948$, $g = 0.991$. The results come from a simulation of the three-layered model used in Paper V with 0.3 g RBC / 100 g tissue in the superior dermis layer, and 0.8 g RBC / 100 g tissue in the inferior dermis layer. The plotted apparent phase functions are divided for Doppler shifts occurring in the superior and inferior dermis layers, respectively, and for those occurring in the superior layer, divided for photons that have only been shifted in that layer and photons that have been shifted in both layers. The probability for a low $\cos\theta$, i.e. a large scattering angle θ and thus a large Doppler shift, is slightly higher for photons that have only been shifted in the superior dermis layer. Since this effect is not accounted for in the forward problem, the results will not be fully accurate. Although this could be accounted for, the effect on the presented quantities is rather small as seen in Paper V, and is therefore neglected.
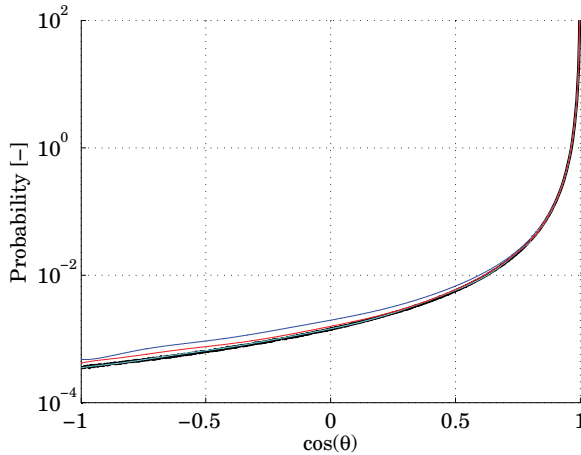
Figure 9.2 Apparent scattering phase functions for photons detected at the 0.25 mm source-detector separation. The thick black curve is the true phase function of blood used in the simulation, the upper curve is the apparent phase function for photons only scattered in the superior dermis layer, the middle curve for Doppler shifts in the inferior dermis layer, and the lower curve (identical to the true phase function) for Doppler shifts in the superior dermis layer that have also been propagating in the inferior dermis layer.

The three-layered model in Paper V differs from the six-layered skin model in Paper II. The model in Paper II was developed to replicate the general structure of skin. However, since there was a fixed relationship between the blood flow of the individual layers in that model, it was not flexible enough for maximal performance in the quantitative LDF method. This was found when evaluating data in paper VI. Therefore, a generalization of the six-layered model was developed in Paper V. Furthermore, the velocity distribution was a stepwise function in the six-layered model in Paper II, whereas it was continuous in the model in Paper V. It should also be noted that the three-layered model in Paper V can adapt to a homogeneous model.

9.3   Presented quantities

The most obvious difference between conventional LDF and the proposed quantitative LDF is that the presented perfusion estimate in conventional LDF is directly calculated from the Doppler power spectra, whereas the perfusion estimate from the quantitative LDF is given from the adapted tissue model. Under the assumption that the model is in agreement with the studied tissue, the amount of information that can be gathered from the model is large as compared to the conventional measure. However, the model contains a number of assumptions and simplifications that were discussed in the previous section. Quite naturally, that model can therefore not perfectly describe the examined tissue, and therefore it is important to realize when the model is valid, in order to avoid presenting erroneous data from the model.

First of all, the data presented are most reliable over the average of the volume that is mainly probed by the two source-detector separations. It is proposed that this volume can be represented with a 3 mm^3 half sphere, which is in between the normal measurement volume for the 0.25 and 1.2 mm source-detector separations. [IV] Looking only at a part of this volume will not be in as good agreement to the real tissue as for the whole volume. For maximal robustness of the method, the data could be presented exactly for the diffuse volume that is probed by the two source-detector separations in the adapted model, with

the highest weight close to the emitting fiber and less weight further away, as in Figure 8.4a. That approach would however severely obstruct the physiological interpretation of the results and comparisons between different measurements would be almost as troublesome as with conventional LDF measures.

It is proposed in Paper V that the concentration and perfusion measures can be divided into three velocity regions; below 1 mm/s, 1-10 mm/s, and above 10 mm/s. In the model, the velocity distribution is continuous and it would therefore be possible to increase the velocity resolution. However, the method robustness for an increased resolution has not been evaluated and it is questionable if a higher velocity resolution would significantly improve the clinical information. For higher velocity resolution, the model has to be more detailed with an increasing number of free parameters. For such a model to be robust, the Doppler power spectra from the two source-detector separations are not enough, and that would require more input data into the inverse problem.

9.4   Methodological considerations

The quantitative LDF method has a full model-based reverse engineering approach. This makes it unique among all LDF methods presented until today and as previously described it also solves many of the conventional LDF limitations and enables data presented in absolute units and constant output volume with an accuracy that is analyzed and discussed in Paper V.

In principle, the solving of the reverse problem translates the total power of the Doppler power spectrum and its frequency distribution into the absolute units of mm/s and g RBC/100 g tissue. The translation is made possible due to the calibration of the total power to a measurement where all detected light is Doppler shifted, and the fact that the frequency shifts can be exactly calculated (Equation 5.1). This model-based approach should not be confused with early attempts of absolute calibrating the perfusion estimate to flow phantoms, a strategy that was quickly abandoned due to extremely poor reliability.

In contrast to conventional LDF, the quantitative LDF method has a means of excluding measurements which the model can not adapt to. This is for example useful to exclude measurements very close to large vessels, where both the quantitative LDF model and the model that is the foundation of conventional LDF [8] are inadequate. This could prevent erroneous conclusions in clinical studies.

The use of two source-detector separations where Doppler power spectra are fitted for both separations simultaneously is of the uttermost importance to reduce the risk of multiple solutions to the reverse problem. This follows from the fact the Doppler power spectra are generally affected differently by a redistribution of blood, changed blood tissue fraction, and changed velocity distribution in part of the tissue. Moreover, the use of an operating wavelength around 780 nm is optimal for LDF, both the conventional and quantitative methods, for a number of reasons. First, the absorption coefficient of melanin in the epidermis is low at this wavelength, which makes the method insensitive to skin pigmentation. The difference in absorption between oxygenized and deoxygenized blood is minimal (0 at about 800 nm), which can be compared to the situation at 633 nm where μ_a of deoxygenized blood is almost a factor 10 higher than for oxygenized blood. The overall absorption of blood is also low, compared to wavelengths under 600 nm, which leads to smaller variations in the output volume when the blood tissue fraction is varied, for conventional LDF.

The results presented in Papers V and VI are retrieved using an implementation of the method in Matlab 7.6 (Mathworks Inc., US). A couple of seconds are normally required to find the best fit model using a single 2.4 GHz processor. It is likely that code optimization and the use of a better suited environment would reduce this time at least an order of magnitude, but it may still limit the use of the method in a real-time setup where high temporal resolution is required.

Another limiting factor compared to conventional LDF, except the increased method complexity, is that the quality of the spectra used in the fitting procedure must be high. This has been solved by ensemble averaging over five second intervals in Papers V and VI, an approach that makes pulse detection impossible. Furthermore, it is not mathematically correct to calculate the ensemble average for an ensemble where the expectation value is not constant (since pulsations are expected in parts of the microcirculation). This is not seen as a large problem as the resulting spectra will just include frequencies both from diastole and systole, though. However, the conventional perfusion estimate, calculated at a higher temporal resolution, could be used to exclude for example the peaks in the pulsations to achieve an ensemble average for diastole. Another straight forward alternative is to increase the laser output or the detector sensitivity of the LDF system to increase the spectral quality and temporal resolution.

9.5   Clinical possibilities

Merely the presentation of the perfusion value in a physiologically relevant unit will probably ease the interpretation of the results from LDF measurements. But more importantly, this unit, together with the constant and geometrically defined output volume, will make inter- and intra-individual comparisons less troublesome. This is further emphasized by the fact that optical properties of the static tissue do not seem to significantly affect the results of the quantitative LDF method, within values relevant for skin. [V]

Another aspect of the clinical benefits with the quantitative LDF method is the separation in three different flow velocity regions. This separation may under some circumstances enable means of differentiating the flow into different flow compartments, by relating high velocity flow to relatively large vessels, and low velocity flow to the nutritive capillary flow. However, it must be realized that for example the low velocity flow may also be present in other types of vessels, foremost veins.

The quantitative LDF method was used in Paper VI where a clinical study on diabetes type 2 was performed. The new method confirmed that changes during a heat provocation is a process foremost involving relatively large, high velocity vessels and that differences between diabetic patients and controls during heat are found in these vessels. More interesting however was the correlation between baseline flow and diabetes duration, where the low velocity perfusion decreased whereas the intermediate velocity perfusion increased and the high velocity perfusion was unaffected. These findings are well in line with the theory that diabetic patients have an increased arteriovenous shunt flow which has a negative effect on the nutritive capillary flow, [139] and can not be assessed using conventional LDF.

9.6   Future prospects

Conventional LDF is a well established method that has been used for three decades within clinical research. Therefore, the quantitative LDF method will need more clinical studies to prove its advantages over conventional LDF and to be clinically accepted. Furthermore, its reliability, especially regarding discrete vessels, must be further investigated, although there are no indications that the reliability would be less than for conventional LDF in such situations.

Since the proposed method is based on a microcirculatory and optical model, its principles are not only applicable to LDF. Integrating measurements from other modalities into the model would probably increase its robustness considerably. Initial trials have already begun merging LDF and diffuse reflectance spectroscopy (DRS) [70,166,167] into the same model. This would strengthen both techniques much more than just taking two

conventional LDF and DRS systems and combining them into the same measurement probe, but still perform the data processing separately. A device combining the two techniques into the same model would give an instrument that is able to give a comprehensive picture of the microcirculation, including velocity resolved perfusion and blood tissue fraction as well as blood oxygen status. Due to the capability of DRS to estimate the blood tissue fraction in a different manner than LDF, as well as estimating the optical properties of the tissue, it is likely that the robustness of such an instrument would be greater than for the proposed quantitative LDF method, as well as being more general.

The principles of the quantitative LDF method are by no means limited to fiber-based systems but may also be applied in an imaging system, although the computational burden would be high. In fact, implementing the method in a CMOS imaging system combined with some inhomogeneous laser illumination pattern could increase the informational input to the model leading to more robust model adaption.

10 Conclusions

In this thesis, it has been shown that it is possible to use a model-based reverse engineering approach to analyze LDF signals. The analysis method presented, called quantitative laser Doppler flowmetry, gives a velocity resolved perfusion estimate in the physiologically relevant unit g RBC / 100 g tissue × mm/s, in a constant and defined output volume of 3 mm^3. The robustness has been evaluated and found to be superior to that of the conventional LDF method. The quantitative LDF method also gives a means of excluding uncertain measurements where the model adapts poorly, which has not been possible using conventional LDF.

The physiologically relevant unit of the perfusion estimate and the constant output volume will facilitate the physiological interpretation of the results and comparisons of inter- and intra-individual measurements. It also opens up new possibilities for comparisons with other methods, not only in a relative manner during tissue provocations.

The quantitative LDF has been used in an initial clinical study on diabetes type 2 patients. The method enabled conclusions that could not be drawn using the conventional LDF method, including reduced nutritive and increased shunt flow during baseline for patients with a long diabetes duration.

Acknowledgements

My first personal "thank you" goes to my supervisors Tomas and Marcus. Tomas' excellent guidance throughout my PhD studies and never ending eagerness to dig into the details in the research have been combined with Marcus' deep theoretical bio-optical skills in a way that makes other PhD students green with envy. Thank you also for being great colleagues and friends which makes working so much more easy and fun.

I would also like to express my gratitude to Göran for opening doors for me during my first time at IMT and for your dedication to undergraduate students that inspired me to continue within the field of biomedical engineering. Furthermore (a word now used 25 times in this thesis, I have counted them), thank you Erik and Michail for letting me feel welcome at IMT, Tobias for being the perfect companion during my PhD studies, Gert, Karin and Johannes for valuable comments on my thesis, and Linda, Martin, Joakim, Håkan and all who I do not mention for being great colleagues, fika-comrades, and table-hockey opponents.

I will not pass the opportunity to express my appreciation to Perimed AB and especially to Hans-Eric, Björn, Fredrik and Anders for a valuable cooperation. Our discussions regarding the whole field of LDF, from theory to application, have been both challenging and fruitful, hopefully not only to me, and it has always been nice to see you all. I hope this thesis is just a milestone in our cooperation.

Nu till de som givit mig grunden och möjligheterna till den här boken – Mamma och Pappa. Tack för ert stöd och uppmuntran ända från småskolan och igenom alla de val jag har gjort sedan dess! Ni ska veta att jag är evigt tacksam för att ni givit mig så många möjligheter i livet och för allt ni gör för mig och min familj.

Till sist, tack Carina och Elias för att ni gör mitt liv underbart, Ich hab' euch lieb!

References

1. A.T. Forrester, R.A. Gudmundsen, and P.O. Johnson, *Photoelectric Mixing of Incoherent Light,* Physical Review, 99(6), 1691 LP - 1700, 1955

2. A.T. Forrester, *Photoelectric Mixing As a Spectroscopic Tool,* Journal of the Optical Society of America, 51(3), 253-259, 1961

3. H.Z. Cummins and H.L. Swinney, *Light Beating Spectroscopy*, in *Progress in optics*, E. Wolf, 135-200, North-Holland, 1970

4. M.D. Stern, *In vivo evaluation of microcirculation by coherent light scattering,* Nature, 254, 56-8, 1975

5. G.A. Holloway Jr. and D.W. Watkins, *Laser Doppler measurement of cutaneous blood flow,* The Journal of Investigative Dermatology, 69(3), 306-9, 1977

6. G.E. Nilsson, T. Tenland, and P.Å. Öberg, *A new instrument for continuous measurement of tissue blood flow by light beating spectroscopy,* IEEE Transactions on Biomedical Engineering, 27(1), 12-9, 1980

7. G.E. Nilsson, T. Tenland, and P.Å. Öberg, *Evaluation of a laser Doppler flowmeter for measurement of tissue blood flow,* IEEE Transactions on Biomedical Engineering, 27(10), 597-604, 1980

8. R. Bonner and R. Nossal, *Model for laser Doppler measurements of blood flow in tissue,* Applied Optics, 20(12), 2097-2107, 1981

9. G.E. Nilsson, *Signal processor for laser Doppler tissue flowmeters,* Medical and Biological Engineering and Computing, 22(4), 343-8, 1984

10. G.E. Nilsson, A. Jakobsson, and K. Wårdell. *Imaging of tissue blood flow by coherent light scattering.* in Engineering in Medicine and Biology Society, 1989. Images of the Twenty-First Century., Proceedings of the Annual International Conference of the IEEE Engineering in. 1989.

11. T.J.H. Essex and P.O. Byrne, *A Laser Doppler Scanner for Imaging Blood-Flow in Skin,* Journal of Biomedical Engineering, 13(3), 189-194, 1991

12. K. Wårdell, A. Jakobsson, and G.E. Nilsson, *Laser-Doppler Perfusion Imaging by Dynamic Light-Scattering,* IEEE Transactions on Biomedical Engineering, 40(4), 309-319, 1993

13. M.L. Iabichella, E. Melillo, and G. Mosti, *A review of microvascular measurements in wound healing,* The International Journal of Lower Extremity Wounds, 5(3), 181-99, 2006

14. L. Devgan, S. Bhat, S. Aylward, and R.J. Spence, *Modalities for the assessment of burn wound depth,* Journal of Burns and Wounds, 5, e2, 2006

15. M. Stücker, M. Esser, M. Hoffmann, U. Memmel, A. Hirschmuller, C. Von Bormann, K. Hoffmann, and P. Altmeyer, *High-resolution laser Doppler perfusion imaging aids in differentiating between benign and malignant melanocytic skin tumours,* Acta Dermato-Venereologica, 82(1), 25-29, 2002

16. L. Lantsberg and M. Goldman, *Laser Doppler flowmetry, transcutaneous oxygen tension measurements and Doppler pressure compared in patients undergoing amputation,* European Journal of Vascular Surgery, 5(2), 195-7, 1991

17. S.A. Ray, T.M. Buckenham, A.M. Belli, R.S. Taylor, and J.A. Dormandy, *The predictive value of laser Doppler fluxmetry and transcutaneous oximetry for clinical outcome in patients undergoing revascularisation for severe leg ischaemia,* European Journal of Vascular and Endovascular Surgery, 13(1), 54-9, 1997

18. K. Wårdell, P. Blomstedt, J. Richter, J. Antonsson, O. Eriksson, P. Zsigmond, A.T. Bergenheim, and M.I. Hariz, *Intracerebral microvascular measurements during deep brain stimulation implantation using laser Doppler perfusion monitoring,* Stereotactic and Functional Neurosurgery, 85(6), 279-86, 2007

19. D.I. Booi, I.B. Debats, W.D. Boeckx, and R.R. Van Der Hulst, *A study of perfusion of the distal free-TRAM flap using laser Doppler flowmetry,* Journal of Plastic, Reconstructive & Aesthetic Surgery, 61(3), 282-8, 2008

20. V. Rajan, B. Varghese, T.G. Van Leeuwen, and W. Steenbergen, *Review of methodological developments in laser Doppler flowmetry,* Lasers in Medical Science, 24(2), 269-83, 2009

21. U. Hoffmann, U.K. Franzeck, M. Geiger, A. Yanar, and A. Bollinger, *Variability of Different Patterns of Skin Oscillatory Flux in Healthy Controls and Patients with Peripheral Arterial Occlusive Disease,* International Journal of Microcirculation-Clinical and Experimental, 12(3), 255-273, 1993

22. H.D. Kvernmo, A. Stefanovska, M. Bracic, K.A. Kirkebøen, and K. Kvernebo, *Spectral analysis of the laser Doppler perfusion signal in human skin before and after exercise,* Microvascular Research, 56(3), 173-182, 1998

23. M. Bracic and A. Stefanovska, *Wavelet-based analysis of human blood-flow dynamics,* Bulletin of Mathematical Biology, 60(5), 919-35, 1998

24. A. Humeau, L. Fizanne, A. Garry, J.L. Saumet, and J.P. L'huillier, *Signal processing methodology to study the cutaneous vasodilator response to a local external pressure application detected by laser Doppler flowmetry,* IEEE Transactions on Biomedical Engineering, 51(1), 190-2, 2004

25. R. Lohwasser and G. Soelkner, *Experimental and theoretical laser-Doppler frequency spectra of a tissuelike model of a human head with capillaries,* Applied Optics, 38(10), 2128-2137, 1999

26. A. Kienle, *Non-invasive determination of muscle blood flow in the extremities from laser Doppler spectra,* Physics in Medicine and Biology, 46(4), 1231-44, 2001

27. T. Binzoni, T.S. Leung, D. Boggett, and D. Delpy, *Non-invasive laser Doppler perfusion measurements of large tissue volumes and human skeletal muscle blood RMS velocity,* Physics in Medicine and Biology, 48(15), 2527-2549, 2003

28. A.L. Petoukhova, W. Steenbergen, and F.F. De Mul, *Path-length distribution and path-length-resolved Doppler measurements of multiply scattered photons by use of low-coherence interferometry,* Optics Letters, 26(19), 1492-4, 2001

29. B. Varghese, V. Rajan, T.G. Van Leeuwen, and W. Steenbergen, *Path-length-resolved measurements of multiple scattered photons in static and dynamic turbid media using phase-modulated low-coherence interferometry,* Journal of Biomedical Engineering, 12(2), 024020, 2007

30. K. Dörschel and G. Müller, *Velocity resolved laser Doppler blood flow measurements in skin,* Flow Measurement and Instrumentation, 7(3-4), 257-264, 1996

31. A. Liebert, N. Zolek, and R. Maniewski, *Decomposition of a laser-Doppler spectrum for estimation of speed distribution of particles moving in an optically turbid medium: Monte Carlo validation study,* Physics in Medicine and Biology, 51(22), 5737-5751, 2006

32. A. Liebert, N. Zolek, S. Wojtkiewicz, and R. Maniewski. *Estimation of Speed Distribution of Particles Moving in an Optically Turbid Medium Using Decomposition of a Laser-Doppler Spectrum.* in Engineering in Medicine and Biology Society, 2007. EMBS 2007. 29th Annual International Conference of the IEEE. 2007.

33. M. Larsson and T. Strömberg, *Toward a velocity-resolved microvascular blood flow measure by decomposition of the laser Doppler spectrum,* Journal of Biomedical Engineering, 11(1), 014024, 2006

34. M. Larsson, W. Steenbergen, and T. Strömberg, *Influence of optical properties and fiber separation on laser Doppler flowmetry,* Journal of Biomedical Optics, 7(2), 236-243, 2002

35. M.H. Koelink, F.F.M. De Mul, J. Greve, R. Graaff, A.C.M. Dassel, and J.G. Aarnoudse, *Laser-Doppler Blood Flowmetry Using two Wavelengths - Monte-Carlo Simulations and Measurements,* Applied Optics, 33(16), 3549-3558, 1994

36. I.I. Tulevski, D.T. Ubbink, and M.J.H.M. Jacobs, *Red and green laser Doppler compared with capillary microscopy to assess skin microcirculation in the feet of healthy subjects,* Microvascular Research, 58(2), 83-88, 1999

37. O. Andrée Larsen, N.A. Lassen, and F. Quaade, *Blood Flow through Human Adipose Tissue Determined with Radioactive Xenon,* Acta Physiologica Scandinavica, 66(3), 337-345, 1966

38. A.M. Rudolph and M.A. Heymann, *The Circulation of the Fetus in Utero: Methods For Studying Distribution of Blood Flow, Cardiac Output And Organ Blood Flow,* Circulation Research, 21(2), 163-184, 1967

39. M.A. Heymann, B.D. Payne, J.I. Hoffman, and A.M. Rudolph, *Blood flow measurements with radionuclide-labeled particles,* Progress in Cardiovascular Diseases, 20(1), 55-79, 1977

40. C.M. Black, R.P. Clark, K. Darton, M.R. Goff, T.D. Norman, and H.A. Spikes, *A pyroelectric thermal imaging system for use in medical diagnosis,* Journal of Biomedical Engineering, 12(4), 281-6, 1990

41. S. Bornmyr, H. Svensson, B. Lilja, and G. Sundkvist, *Skin temperature changes and changes in skin blood flow monitored with laser Doppler flowmetry and imaging: a methodological study in normal humans,* Clinical Physiology, 17(1), 71-81, 1997

42. A. Merla and G.L. Romani. *Functional Infrared Imaging in Medicine: A Quantitative Diagnostic Approach.* in Engineering in Medicine and Biology Society, 2006. EMBS '06. 28th Annual International Conference of the IEEE. 2006.

43. A. Bollinger, P. Butti, J.P. Barras, H. Trachsler, and W. Siegenthaler, *Red blood cell velocity in nailfold capillaries of man measured by a television microscopy technique,* Microvascular Research, 7(1), 61-72, 1974

44. J. Zhong, C.L. Asker, and E.G. Salerud, *Imaging, image processing and pattern analysis of skin capillary ensembles,* Skin Research and Technology, 6(2), 45-57, 2000

45. Y.H. Zhao, Z.P. Chen, C. Saxer, S.H. Xiang, J.F. De Boer, and J.S. Nelson, *Phase-resolved optical coherence tomography and optical Doppler tomography for imaging blood flow in human skin with fast scanning speed and high velocity sensitivity,* Optics Letters, 25(2), 114-116, 2000

46. G. Maret and P.E. Wolf, *Multiple Light-Scattering from Disordered Media - the Effect of Brownian-Motion of Scatterers,* Zeitschrift Für Physik B-Condensed Matter, 65(4), 409-413, 1987

47. M.J. Stephen, *Temporal Fluctuations in Wave-Propagation in Random-Media,* Physical Review B, 37(1), 1-5, 1988

48. D.J. Pine, D.A. Weitz, P.M. Chaikin, and E. Herbolzheimer, *Diffusing-Wave Spectroscopy,* Physical Review Letters, 60(12), 1134-1137, 1988

49. J.D. Briers, *Laser Doppler, speckle and related techniques for blood perfusion mapping and imaging,* Physiological Measurement, 22(4), R35-66, 2001

50. J. Mobley and T. Vo-Dinh, *Optical Properties of Tissue,* in *Biomedical photonics handbook,* T. Vo-Dinh, 2.1 - 2.75, CRC Press, 2003

51. C.F. Bohren and D.R. Huffman, *Absorption and scattering of light by small particles,* Wiley, New York, 1998

52. I.V. Meglinsky and S.J. Matcher, *Modelling the sampling volume for skin blood oxygenation measurements,* Medical & Biological Engineering & Computing, 39(1), 44-50, 2001

53. S.L. Jacques, *Skin Optics,* Oregon Medical Laser Center News, http://omlc.ogi.edu/news/jan98/skinoptics.html, 1998

54. G.M. Hale and M.R. Querry, *Optical Constants of Water in the 200-nm to 200-µm Wavelength Region,* Applied Optics, 12(3), 555-563, 1973

55. W.G. Zijlstra, A. Buursma, and O.W. Van Assendelft, *Visible and near infrared absorption spectra of human and animal haemoglobin Determination and application*, VSP, Utrecht, Boston, Köln, Tokyo, 2000

56. E. Hecht, *Optics*, Addison Wesley, San Francisco, 2002

57. L.G. Henyey and J.L. Greenstein, *Diffuse radiation in the galaxy,* Astrophysical Journal, 93, 70-83, 1941

58. L.O. Reynolds and N.J. Mccormick, *Approximate two-parameter phase function for light scattering,* Journal of the Optical Society of America, 70(10), 1206-1212, 1980

59. B.C. Wilson, *Measurement of tissue optical properties: methods and theories*, in *Optical-Thermal Response of Laser-Irradiated Tissue*, A.J. Welch and M.J.C. van Gemert, Plenum Press, 1995

60. W.F. Cheong, S.A. Prahl, and A.J. Welch, *A Review of the Optical-Properties of Biological Tissues,* IEEE Journal of Quantum Electronics, 26(12), 2166-2185, 1990

61. L.H. Wang and S.L. Jacques, *Error Estimation of Measuring Total Interaction Coefficients of Turbid Media Using Collimated Light Transmission,* Physics in Medicine and Biology, 39(12), 2349-2354, 1994

62. R. Michels, A. Kienle, F.K. Forster, M.W. Mueller, and R. Hibst. *Goniometric measurement of the phase function of different fat emulsions.* in Photon Migration and Diffuse-Light Imaging II. 2005: SPIE.

63. J.W. Pickering, S.A. Prahl, N. Vanwieringen, J.F. Beek, H.J.C.M. Sterenborg, and M.J.C. Vangemert, *Double-Integrating-Sphere System for Measuring the Optical-Properties of Tissue,* Applied Optics, 32(4), 399-410, 1993

64. I.V. Yaroslavsky, A.N. Yaroslavsky, T. Goldbach, and H.J. Schwarzmaier, *Inverse hybrid technique for determining the optical properties of turbid media from integrating-sphere measurements,* Applied Optics, 35(34), 6797-6809, 1996

65. J.S. Dam, T. Dalgaard, P.E. Fabricius, and S. Andersson-Engels, *Multiple polynomial regression method for determination of biomedical optical properties from integrating sphere measurements,* Applied Optics, 39(7), 1202-1209, 2000

66. T.J. Farrell, M.S. Patterson, and B. Wilson, *A diffusion theory model of spatially resolved, steady-state diffuse reflectance for the noninvasive determination of tissue optical properties in vivo,* Medical Physics, 19(4), 879-88, 1992

67. A. Kienle, L. Lilge, M.S. Patterson, R. Hibst, R. Steiner, and B.C. Wilson, *Spatially resolved absolute diffuse reflectance measurements for noninvasive determination of the optical scattering and absorption coefficients of biological tissue,* Applied Optics, 35(13), 2304-2314, 1996

68. M. Larsson, H. Nilsson, and N.O.T. Strömberg, *In vivo determination of local skin optical properties and photon path length by use of spatially resolved diffuse reflectance with applications in laser Doppler flowmetry,* Applied Optics, 42(1), 124-134, 2003

69. F. Bevilacqua and C. Depeursinge, *Monte Carlo study of diffuse reflectance at source-detector separations close to one transport mean free path,* Journal of the Optical Society of America a-Optics Image Science and Vision, 16(12), 2935-2945, 1999

70. T. Lindbergh, I. Fredriksson, M. Larsson, and T. Strömberg, *Spectral determination of a two-parametric phase function forpolydispersive scattering liquids,* Optics Express, 17(3), 1610-1621, 2009

71. L.H. Wang and S.L. Jacques, *Use of a Laser-Beam with an Oblique Angle of Incidence to Measure the Reduced Scattering Coefficient of a Turbid Medium,* Applied Optics, 34(13), 2362-2366, 1995

72. T. Lindbergh, M. Larsson, I. Fredriksson, and T. Strömberg. *Reduced scattering coefficient determination by non-contact oblique angle illumination: methodological considerations.* in Optical Interactions with Tissue and Cells XVIII. 2007: SPIE.

73. M.S. Patterson, B. Chance, and B.C. Wilson, *Time Resolved Reflectance and Transmittance for the Noninvasive Measurement of Tissue Optical-Properties,* Applied Optics, 28(12), 2331-2336, 1989

74. S.L. Jacques, L.H. Wang, and A.H. Hielscher, *Time-resolved photon propagation in tissues*, in *Optical-Thermal Response of Laser-Irradiated Tissue*, A.J. Welch and M.J.C. van Gemert, Plenum Press, 1995

75. C. Abrahamsson, T. Svensson, S. Svanberg, S. Andersson-Engels, J. Johansson, and S. Folestad, *Time and wavelength resolved spectroscopy of turbid media using light continuum generated in a crystal fiber,* Optics Express, 12(17), 4103-4112, 2004

76. E. Alerstam, S. Andersson-Engels, and T. Svensson, *White Monte Carlo for time-resolved photon migration,* Journal of Biomedical Optics, 13(4), 041304, 2008

77. M.S. Patterson, J.D. Moulton, B.C. Wilson, K.W. Berndt, and J.R. Lakowicz, *Frequency-Domain Reflectance for the Determination of the Scattering and Absorption Properties of Tissue,* Applied Optics, 30(31), 4474-4476, 1991

78. M.S. Patterson, *Principles and applications of frequency-domain measurements of light propagation*, in *Optical-Thermal Response of Laser-Irradiated Tissue*, A.J. Welch and M.J.C. van Gemert, Plenum Press, 1995

79. I.V. Yaroslavsky, A.N. Yaroslavsky, H.-J. Schwarzmaier, G.G. Akchurin, and V.V. Tuchin. *New approach to Monte Carlo simulation of photon transport in the frequency domain.* in Photon Propagation in Tissues. 1995: SPIE.

80. G. Alexandrakis, T.J. Farrell, and M.S. Patterson, *Monte Carlo diffusion hybrid model for photon migration in a two-layer turbid medium in the frequency domain,* Applied Optics, 39(13), 2235-2244, 2000

81. A. Kienle, M.S. Patterson, L. Ott, and R. Steiner, *Determination of the scattering coefficient and the anisotropy factor from laser Doppler spectra of liquids including blood,* Applied Optics, 35(19), 3404-3412, 1996

82. S.A. Prahl, *Light transport in tissue.* 1988, The university of Texas at Austin: Austin.

83. W.M. Star, *Diffusion theory of light transport*, in *Optical-Thermal Response of Laser-Irradiated Tissue*, A.J. Welch and M.J.C. van Gemert, Plenum Press, 1995

84. E. Alerstam, T. Svensson, and S. Andersson-Engels, *Parallel computing with graphics processing units for high-speed Monte Carlo simulation of photon migration,* Journal of Biomedical Optics, 13(6), 060504-3, 2008

85. S.A. Prahl, M. Keijzer, S.L. Jacques, and A.J. Welch. *A Monte Carlo Model of Light Propagation in Tissue.* in SPIE Proceedings of Docimetry of Laser Radiation in Medicine and Biology. 1989.

86. L.H. Wang, S.L. Jacques, and L.Q. Zheng, *MCML - Monte-Carlo Modeling of Light Transport in Multilayered Tissues,* Computer Methods and Programs in Biomedicine, 47(2), 131-146, 1995

87. P. Thueler, I. Charvet, F. Bevilacqua, M.S. Ghislain, G. Ory, P. Marquet, P. Meda, B. Vermeulen, and C. Depeursinge, *In vivo endoscopic tissue diagnostics based on spectroscopic absorption, scattering, and phase function properties,* Journal of Biomedical Optics, 8(3), 495-503, 2003

88. J. Swartling, *Biomedical and atmospheric applications of optical spectroscopy in scattering media*, Lund University, Lund, 2002

89. A. Kienle and R. Hibst, *Light guiding in biological tissue due to scattering,* Physical Review Letters, 97(1), 2006

90. E. Veach, *Robust Monte Carlo Methods for Light Transport Simulation*, in *Department of Computer Science.* 1997, Stanford University: Stanford.

91. N.G. Chen and J. Bai, *Estimation of quasi-straightforward propagating light in tissues,* Physics in Medicine and Biology, 44(7), 1669-1676, 1999

92. G. Yao and L.H.V. Wang, *Monte Carlo simulation of an optical coherence tomography signal in homogeneous turbid media,* Physics in Medicine and Biology, 44(9), 2307-2320, 1999

93. R.R. Meier, J.-S. Lee, and D.E. Anderson Jr., *Atmospheric scattering of middle UV radiation from an internal source,* Applied Optics, 17(20), 3216, 1978

94. J.W. Beck, R.J. Jaszczak, R.E. Coleman, C.F. Starmer, and L.W. Nolte, *Analysis of SPECT including Scatter and Attenuation Using Sophisticated Monte Carlo Modeling Methods,* IEEE Transactions on Nuclear Science, 29(1), 506-511, 1982

95. E. Berrocal, D.Y. Churmakov, V.P. Romanov, M.C. Jermy, and I.V. Meglinski, *Crossed source-detector geometry for a novel spray diagnostic: Monte Carlo simulation and analytical results,* Applied Optics, 44(13), 2519-2529, 2005

96. D.Y. Churmakov, V.L. Kuzmin, and I.V. Meglinski, *Application of the vector Monte-Carlo method in polarisation optical coherence tomography,* Quantum Electronics, 36(11), 1009-1015, 2006

97. E. Tinet, S. Avrillier, and J.M. Tualle, *Fast semianalytical Monte Carlo simulation for time-resolved light propagation in turbid media,* Journal of the Optical Society of America a-Optics Image Science and Vision, 13(9), 1903-1915, 1996

98. L.H. Wang, S.L. Jacques, and L.Q. Zheng, *CONV - convolution for responses to a finite diameter photon beam incident on multi-layered tissues,* Computer Methods and Programs in Biomedicine, 54(3), 141-150, 1997

99. R. Graaff, M.H. Koelink, F.F.M. De Mul, W.G. Zijlstra, A.C.M. Dassel, and J.G. Aarnoudse, *Condensed Monte-Carlo Simulations for the Description of Light Transport,* Applied Optics, 32(4), 426-434, 1993

100. A. Kienle and M.S. Patterson, *Determination of the optical properties of turbid media from a single Monte Carlo simulation,* Physics in Medicine and Biology, 41(10), 2221-7, 1996

101. J. Swartling, A. Pifferi, A.M.K. Enejder, and S. Andersson-Engels, *Accelerated Monte Carlo models to simulate fluorescence spectra from layered tissues,* Journal of the Optical Society of America A, 20(4), 714-727, 2003

102. Q. Liu and N. Ramanujam, *Scaling method for fast Monte Carlo simulation of diffuse reflectance spectra from multilayered turbid media,* Journal of the Optical Society of America a-Optics Image Science and Vision, 24(4), 1011-1025, 2007

103. N.G. Chen, *Controlled Monte Carlo method for light propagation in tissue of semi-infinite geometry,* Applied Optics, 46(10), 1597-1603, 2007

104. R.G. Giovanelli, *Reflection by Semi-infinite Diffusers,* Journal of Modern Optics, 2, 153-162, 1955

105. H.C. Van De Hulst, *Multiple light scattering : tables, formulas, and applications, vol II,* 1980

106. J.C. Doppler, *Über das farbige Licht der Doppelsterne und einiger anderer Gestirne des Himmels [On the coloured light of the double stars and some other stars of the heavens]*, in *Der Königl. Böhm. Gesellschaft der Wissenschaften.* 1842.

107. I. Fredriksson, C. Fors, and J. Johansson, *Laser Doppler Flowmetry - a Theoretical Framework*, Department of Biomedical Engineering, Linköping University, www.imt.liu.se/bit/ldf/ldf, 2007

108. M. Larsson, *Influence of optical properties on Laser Doppler Flowmetry*, in *Department of Biological Engineering.* 2004, Linköping University: Linköping.

109. A.E. Siegman, *The antenna properties of optical heterodyne receivers,* Proceedings of the IEEE, 54(10), 1350-1356, 1966

110. A.N. Serov, J. Nieland, S. Oosterbaan, F.F.M. De Mul, H. Van Kranenburg, H.H. Bekman, and W. Steenbergen, *Integrated optoelectronic probe including a vertical cavity surface emitting laser for laser Doppler perfusion monitoring,* IEEE Transactions on Biomedical Engineering, 53(10), 2067-74, 2006

111. V. Rajan, B. Varghese, T.G. Van Leeuwen, and W. Steenbergen, *Speckles in laser Doppler perfusion imaging,* Optics Letters, 31(4), 468-470, 2006

112. A.N. Serov, W. Steenbergen, F.F.M. De Mul, and T. Lasser. *Quasi-parallel laser-Doppler perfusion imaging using a CMOS image sensor*. in Saratov Fall Meeting 2002: Laser Physics and Photonics, Spectroscopy, and Molecular Modeling III; Coherent Optics of Ordered and Random Media III. 2003: SPIE.

113. A. Serov and T. Lasser. *Full-field high-speed laser Doppler imaging system for blood-flow measurements*. in Advanced Biomedical and Clinical Diagnostic Systems IV. 2006. San Jose, CA, USA: SPIE.

114. M.G.D. Karlsson, *Movement artifact reduction in laser Doppler blood flowmetry : myocardial perfusion applications*, in *Department of Biomedical Engineering*. 2005, Linköping University: Linköping.

115. L. Caspary, A. Creutzig, and K. Alexander, *Biological Zero in Laser Doppler Fluxmetry,* International Journal of Microcirculation-Clinical and Experimental, 7(4), 367-371, 1988

116. N.C. Abbot and J.S. Beck, *Biological zero in laser Doppler measurements in normal, ischaemic and inflamed human skin,* International Journal of Microcirculation-Clinical and Experimental, 12(1), 89-98, 1993

117. A. Colantuoni, S. Bertuglia, and M. Intaglietta, *Biological zero of laser Doppler fluxmetry: microcirculatory correlates in the hamster cheek pouch during flow and no flow conditions,* International Journal of Microcirculation-Clinical and Experimental, 13(2), 125-36, 1993

118. E. Wahlberg, P. Olofsson, J. Swedenborg, and B. Fagrell, *Effects of local hyperemia and edema on the biological zero in laser Doppler fluxmetry (LD),* International Journal of Microcirculation-Clinical and Experimental, 11(2), 157-65, 1992

119. H.N. Mayrovitz and J.A. Leedham, *Laser-Doppler imaging of forearm skin: perfusion features and dependence of the biological zero on heat-induced hyperemia,* Microvascular Research, 62(1), 74-8, 2001

120. B. Fagrell and G.E. Nilsson, *Advantages and limitations of one-point laser Doppler perfusion monitoring in clinical practice,* Vascular medicine review, 6, 97-101, 1995

121. D.P. Kernick, J.E. Tooke, and A.C. Shore, *The biological zero signal in laser Doppler fluximetry - origins and practical implications,* Pflügers Archiv : European journal of physiology, 437(4), 624-31, 1999

122. J. Zhong, A.M. Seifalian, E.G. Salerud, and G.E. Nilsson, *A mathematical analysis on the biological zero problem in laser Doppler flowmetry,* IEEE Transactions on Biomedical Engineering, 45(3), 354-64, 1998

123. F.F.M. De Mul, M.H. Koelink, M.L. Kok, P.J. Harmsma, J. Greve, R. Graaff, and J.G. Aarnoudse, *Laser-Doppler Velocimetry and Monte-Carlo Simulations on Models for Blood Perfusion in Tissue,* Applied Optics, 34(28), 6595-6611, 1995

124. A. Serov, W. Steenbergen, and F.F.M. De Mul, *Prediction of the photodetector signal generated by Doppler-induced speckle fluctuations: theory and some validations,* Journal of the Optical Society of America, 18(3), 622-630, 2001

125. G.J. Tortora and S.R. Grabowski, *The Integumentary System*, in *Principles of Anatomy and Physiology*, 140-159, John Wiley & Sons, Inc., 2000

126. A.J. Thody, E.M. Higgins, K. Wakamatsu, S. Ito, S.A. Burchill, and J.M. Marks, *Pheomelanin as well as Eumelanin Is Present in Human Epidermis,* Journal of Investigative Dermatology, 97(2), 340-344, 1991

127. N. Otberg, H. Richter, H. Schaefer, U. Blume-Peytavi, W. Sterry, and J. Lademann, *Variations of Hair Follicle Size and Distribution in Different Body Sites,* Journal of Investigative Dermatology, 122(1), 14-19, 2004

128. A.C. Guyton, *Overview of the Circulation, and Medical Physics of Pressure, Flow, and Resistance*, in *Textbook of medical physiology*, 150-158, Saunders, 1991

129. G.J. Tortora and S.R. Grabowski, *The Cardiovascular System: Blood Vessels and Hemodynamics*, in *Principles of Anatomy and Physiology*, 610-635, John Wiley & Sons, Inc., 2000

130. P.J. Watkins and M.E. Edmonds, *Sympathetic nerve failure in diabetes,* Diabetologia, 25(2), 73-77, 1983

131. A.C. Guyton, *Body Temperature, Temperature Regulation, and Fever*, in *Textbook of medical physiology*, 797-808, Saunders, 1991

132. C. Mørk, C.L. Asker, E.G. Salerud, and K. Kvernebo, *Microvascular Arteriovenous Shunting is a Probable Pathogenetic Mechanism in Erythromelalgia,* Journal of Investigative Dermatology, 114(4), 643-646, 2000

133. N. Charkoudian, *Skin blood flow in adult human thermoregulation: How it works, when it does not, and why,* Mayo Clinic Proceedings, 78(5), 603-612, 2003

134. D.L. Kellogg, Jr., Y. Liu, I.F. Kosiba, and D. O'donnell, *Role of nitric oxide in the vascular effects of local warming of the skin in humans,* Journal of Applied Physiology, 86(4), 1185-90, 1999

135. C.T. Minson, L.T. Berry, and M.J. Joyner, *Nitric oxide and neurally mediated regulation of skin blood flow during local heating,* Journal of Applied Physiology, 91(4), 1619-26, 2001

136. P.E. Pergola, D.L. Kellogg, Jr., J.M. Johnson, W.A. Kosiba, and D.E. Solomon, *Role of sympathetic nerves in the vascular effects of local temperature in human forearm skin,* The American Journal of Physiology, 265(3 Pt 2), H785-92, 1993

137. N.F. Wiernsperger and E. Bouskela, *Microcirculation in insulin resistance and diabetes: more than just a complication,* Diabetes & Metabolism, 29(4 Pt 2), 6S77-87, 2003

138. A.I. Vinik, T. Erbas, T.S. Park, K.K. Pierce, and K.B. Stansberry, *Methods for evaluation of peripheral neurovascular dysfunction,* Diabetes Technology & Therapeutics, 3(1), 29-50, 2001

139. B. Fagrell, G. Jörneskog, and M. Intaglietta, *Disturbed microvascular reactivity and shunting - a major cause for diabetic complications,* Vascular Medicine, 4(3), 125-7, 1999

140. A.J.M. Boulton, J.H.B. Scarpello, and J.D. Ward, *Venous Oxygenation in the Diabetic Neuropathic Foot - Evidence of Arteriovenous Shunting,* Diabetologia, 22(1), 6-8, 1982

141. J.D. Ward, J.M. Simms, G. Knight, A.J.M. Boulton, and D.A. Sandler, *Venous Distension in the Diabetic Neuropathic Foot (Physical Sign of Arteriovenous Shunting),* Journal of the Royal Society of Medicine, 76(12), 1011-1014, 1983

142. G. Jörneskog, K. Brismar, and B. Fagrell, *Skin Capillary Circulation Severely Impaired in Toes of Patients with Iddm, with and without Late Diabetic Complications,* Diabetologia, 38(4), 474-480, 1995

143. M. Rendell and O. Bamisedun, *Diabetic Cutaneous Microangiopathy,* American Journal of Medicine, 93(6), 611-618, 1992

144. K.B. Stansberry, H.R. Peppard, L.M. Babyak, G. Popp, P.M. Mcnitt, and A.I. Vinik, *Primary nociceptive afferents mediate the blood flow dysfunction in non-glabrous (hairy) skin of type 2 diabetes - A new model for the pathogenesis of microvascular dysfunction,* Diabetes Care, 22(9), 1549-1554, 1999

145. S.R. Colberg, H.K. Parson, T. Nunnold, M.T. Herriott, and A.I. Vinik, *Effect of an 8-week resistance training program on cutaneous perfusion in type 2 diabetes,* Microvascular Research, 71(2), 121-127, 2006

146. S. Kilo, M. Berghof, M. Hilz, and R. Freeman, *Neural and endothelial control of the microcirculation in diabetic peripheral neuropathy,* Neurology, 54(6), 1246-1252, 2000

147. C. Nordling and J. Österman, *Physics handbook for science and engineering,* Studentlitteratur, Lund, 1999

148. W.H. Press, B.P. Flannery, S.A. Teukolsky, and W.T. Vetterling, *Numerical Recipes in C : The Art of Scientific Computing,* Cambridge University Press, 1992

149. M. Hazen, *Search strategies for global optimization,* in *Department of electrical engineering.* 2008, University of Washington.

150. A. Jakobsson and G.E. Nilsson, *Prediction of sampling depth and photon pathlength in laser Doppler flowmetry,* Medical and Biological Engineering and Computing, 31(3), 301-7, 1993

151. Z.Y. Qian, S.S. Victor, Y.Q. Gu, C.A. Giller, and H.L. Liu, *"Look-Ahead Distance" of a fiber probe used to assist neurosurgery: Phantom and Monte Carlo study,* Optics Express, 11(16), 1844-1855, 2003

152. N.J. Barnett, G. Dougherty, and S.J. Pettinger, *Comparative study of two laser Doppler blood flowmeters,* Journal of Medical Engineering & Technology, 14(6), 243-9, 1990

153. A.L. Petoukhova, W. Steenbergen, F. Morales, R. Graaff, E.D. De Jong, J.M. Elstrodt, F.F.M. De Mul, and G. Rakhorst, *Instrument-independent flux units for laser Doppler perfusion monitoring assessed in a multi-device study on the renal cortex,* Microvascular Research, 66(2), 83-90, 2003

154. V. Alexopoulos, S. Kollias, P. Leger, H. Boccalon, and Z. Csiki, *Higher-order spectral analysis in laser-Doppler flowmetry signal processing,* Technol and Health Care, 7(2-3), 85-101, 1999

155. M.L. Arildsson, K. Wårdell, and G.E. Nilsson, *Higher order moment processing of laser Doppler perfusion signals,* Journal of Biomedical Optics, 2(4), 358-363, 1997

156. M.G.D. Karlsson and K. Wårdell, *Polarized laser Doppler perfusion imaging--reduction of movement-induced artifacts,* Journal of Biomedical Engineering, 10(6), 064002, 2005

157. M. Meinke, G. Muller, J. Helfmann, and M. Friebel, *Optical properties of platelets and blood plasma and their influence on the optical behavior of whole blood in the visible to near infrared wavelength range,* Journal of Biomedical Optics, 12(1), 014024, 2007

158. S.L. Jacques, J.R. Roman, and K. Lee, *Imaging superficial tissues with polarized light,* Lasers in Surgery and Medicine, 26(2), 119-129, 2000

159. A. Talsma, B. Chance, and R. Graaff, *Corrections for inhomogeneities in biological tissue caused by blood vessels,* Journal of the Optical Society of America a-Optics Image Science and Vision, 18(4), 932-939, 2001

160. A. Kienle, C. Wetzel, A. Bassi, D. Comelli, P. Taroni, and A. Pifferi, *Determination of the optical properties of anisotropic biological media using an isotropic diffusion model,* Journal of Biomedical Optics, 12(1), 2007

161. T.V. Starkey, *The laminar flow of streams of suspended particles,* British Journal of Applied Physics, 7(2), 52-55, 1955

162. E.C. Eckstein, D.G. Bailey, and A.H. Shapiro, *Self-diffusion of particles in shear flow of a suspension,* Journal of Fluid Mechanics, 79(1), 191-208, 1977

163. A. Roggan, M. Friebel, K. Dorschel, A. Hahn, and G. Muller, *Optical properties of circulating human blood in the wavelength range 400-2500 nm,* Journal of Biomedical Engineering, 4(1), 36-46, 1999

164. A.M.K. Enejder, J. Swartling, P. Aruna, and S. Andersson-Engels, *Influence of cell shape and aggregate formation on the optical properties of flowing whole blood,* Applied Optics, 42(7), 1384-94, 2003

165. A.M.K. Nilsson, P. Alsholm, A. Karlsson, and S. Andersson-Engels, *T-matrix computations of light scattering by red blood cells,* Applied Optics, 37(13), 2735-2748, 1998

166. G.M. Palmer and N. Ramanujam, *Monte Carlo-based inverse model for calculating tissue optical properties. Part I: Theory and validation on synthetic phantoms,* Applied Optics, 45(5), 1062-1071, 2006

167. G.M. Palmer, C.F. Zhu, T.M. Breslin, F.S. Xu, K.W. Gilchrist, and N. Ramanujam, *Monte Carlo-based inverse model for calculating tissue optical properties. Part II: Application to breast cancer diagnosis,* Applied Optics, 45(5), 1072-1078, 2006